SCALABLE SYNTHESIS AND ENERGY APPLICATIONS OF DEFECT ENGINEERED NANO MATERIALS

A Dissertation
Presented to
the Graduate School of
Clemson University

In Partial Fulfillment
of the Requirements for the Degree
Doctor of Philosophy
Physics and Astrophysics

---

by
Mehmet Karakaya
December 2015

Accepted by:
Dr. Apparao M. Rao, Committee Chair
Dr. Malcolm J. Skove
Dr. Jian He
Dr. John M. Ballato

ABSTRACT

Nanomaterials and nanotechnologies have attracted a great deal of attention in a few decades due to their novel physical properties such as, high aspect ratio, surface morphology, impurities, *etc.* which lead to unique chemical, optical and electronic properties. The awareness of importance of nanomaterials has motivated researchers to develop nanomaterial growth techniques to further control nanostructures properties such as, size, surface morphology, *etc.* that may alter their fundamental behavior. Carbon nanotubes (CNTs) are one of the most promising materials with their rigidity, strength, elasticity and electric conductivity for future applications. Despite their excellent properties explored by the abundant research works, there is big challenge to introduce them into the macroscopic world for practical applications.

This thesis first gives a brief overview of the CNTs, it will then go on mechanical and oil absorption properties of macro-scale CNT assemblies, then following CNT energy storage applications and finally fundamental studies of defect introduced graphene systems.

Chapter Two focuses on helically coiled carbon nanotube (HCNT) foams in compression. Similarly to other foams, HCNT foams exhibit preconditioning effects in response to cyclic loading; however, their fundamental deformation mechanisms are unique. Bulk HCNT foams exhibit super-compressibility and recover more than 90% of large compressive strains (up to 80%). When subjected to striker impacts, HCNT foams

mitigate impact stresses more effectively compared to other CNT foams comprised of non-helical CNTs (~50% improvement). The unique mechanical properties we revealed demonstrate that the HCNT foams are ideally suited for applications in packaging, impact protection, and vibration mitigation.

The third chapter describes a simple method for the scalable synthesis of three-dimensional, elastic, and recyclable multi-walled carbon nanotube (MWCNT) based light weight bucky-aerogels (BAGs) that are capable of efficiently absorbing non-polar solvents and separating oil-in-water emulsions. Furthermore, BAGs exhibit resilience to impact by recovering more than 70% of the deformation. The energy dissipated by BAGs at 80% compressive strain is in the order of 500 kJm^{-3}, which is nearly 50 times more than the energy dissipated by commercial foams with similar densities.

In the forth chapter, we demonstrate the synthesis of high-surface area, polymer-modified carbon nanotube (or helically coiled carbon nanotube (HCNT)) "paper" electrodes for high-power, high-energy density supercapacitors using simple fabrication methods. The use of conductive, high surface area carbon nanomaterials allows for the utilization of low-cost, non-conductive polymers containing reversible redox groups with higher charge capacity, such as sulfonated lignin. Compared to electrodes containing only helically coiled carbon nanotubes (80 Fg^{-1}), paper electrodes fabricated with redox polymers show an increase in electrode capacitance to over 600 Fg^{-1} along with an increase in charge capacity from 20 mA hrg^{-1} to 80 mA hrg^{-1}.

Chapter Five presents a scalable roll-to-roll (R2R) spray coating process for synthesizing randomly oriented multi-walled carbon nanotubes electrodes on Al foils. The coin and jellyroll type supercapacitors comprised such electrodes yield high power densities (~700 mW/cm^3) and energy densities (1 mW h/cm^3) on par with Li-ion thin film batteries. These devices exhibit excellent cycle stability with no loss in performance over more than a thousand cycles.

In the sixth chapter, we have indicated a methodology for both increasing and decreasing the electrochemical capacitance of Few Layer Graphene based nano-graphites through a combination of argon and hydrogen-based plasma processing. In addition to the utility for charge storage, our work contributes to understanding and controlling the charge storage characteristics.

In the final chapter, we have investigated a nitrogen-doped graphene. We demonstrate through Raman spectroscopy, nonlinear optical and ultrafast spectroscopy, and density functional theory that the graphitic dopant configuration is stable in graphene and does not significantly alter electron–electron or electron–phonon scattering, that is otherwise present in doped graphene, by preserving the crystal coherence length (L_a).

DEDICATION

To my family, without their support, continuous love and encouragement over the past few years, the completion of this work would not have been possible.

ACKNOWLEDGMENTS

I would like to express my special appreciation to my advisor, Dr. Apparao M. Rao for his valuable guidance, scholarly inputs and consistent encouragement. His confidence and guidance have helped me accomplish my goal and overcome obstacles in academic research. Some of the work done in this thesis would not have been possible without the insights of Dr. Ramakrishna Podila. I would like to thank Dr. Malcom Skove and Dr. Jian He for their valuable suggestions. I would also like to thank Dr. Chiara Daraio (ETH Zurich University) and Dr. Thevamaran Ramathasan (Rice University) for dynamic and static impact testing on HCNT and BAG samples. I also would like to thank Dr. Mark Roberts for HCNT/bio-polymer composite project. I also would like to thank Dr. Prabhakar Bandaru for the graphene quantum capacitance project. I also would like to thank Dr. Pooja Puneet for the thermoelectric performance of Bi_2Te_3 project.

I would like to thank Dr. Deepika Saini, Dr. Sriparna Bhattacharya and Herbert Behlow for their help and my fellow students Jingyi Zhu, Anhony Childress, Sai Mallineni, Achyut Raghavendra, Yongchang Dong, Wren Gregory, Fengjiao Liu and Bishwambhar Sengupta.

I would like to thank the Ministry of National Education of Turkey for supporting me to achieve my goal.

Finally I would like to thank my parents at home for supporting me through these years, and my roommates Mustafa and Ahmet, and my good friend, Kemal who have accompanied me on the long road to a doctoral degree, and whose friendship will be treasured.

TABLE OF CONTENTS

Page

TITLE PAGE i

ABSTRACT ii

DEDICATION v

ACKNOWLEDGMENTS vi

LIST OF TABLES xi

LIST OF FIGURES xii

CHAPTER

I. INTRODUCTION 1

1.1 Carbon Nanomaterials introduction 3
1.1.1 Carbon Nanotubes 4
1.1.2 Carbon Nanotubes Synthesis 7
1.2 Defects in Carbon Nanotubes 9
1.2.1 CNTs in different morphology 10
1.2.2 Chemical defects in CNTs 11
1.3 Summary 12

II. ANOMALOUS IMPACT AND STRAIN RESPONSES IN HELICAL CARBON NANOTUBE FOAMS 13
2.1 Introduction 13
2.2 Experimental methods 15
2.2.1 Synthesis 15
2.2.2 Mechanical characterization 16
2.2.3 Sample preparation for TEM 17
2.3 Morphology and structure 17
2.3.1 Quasistatic response 19
2.3.2 Dynamic response 24
2.4 Conclusion 31

Table of Contents (Continued)

Page

III. SELF-ASSEMBLED RECYCLABLE HIERARCHICAL BUCKY AEROGELS 32

3.1 Introduction 32
3.2 Experimental section 33
3.3 Characterization 34
3.3.1 SEM and Porosity measurement 34
3.3.2 Absorption characterization 36
3.3.3 Quasistatic compression test 41
3.4 Conclusion 44

IV. SCALABLE, HIGH-CHARGE CAPACITY CARBON COMPOSITE ELECTRODES BASED ON RENEWABLE REDOX POLYMERS 45

4.1 Introduction 45
4.2 Experimental 49
4.2.1 Materials 49
4.2.2 Preparation 50
4.2.3 Structural Analysis 51
4.2.4 Electrochemical Analysis 51
4.3 Results and discussion 52
4.4 Conclusion 67

V. ROLL-TO-ROLL PRODUCTION OF SPRAY COATED N-DOPED CARBON NANOTUBE ELECTRODES FOR SUPERCAPACITORS 69

5.1 Introduction 69
5.2 Experiment 71
5.2.1 Electrode preparation 71
5.2.2 Electrochemical characterization 73
5.3 Cost Analysis 79
5.4 Conclusion 80

Table of Contents (Continued)

Page

VI. MODULATION OF THE ELECTROSTATIC AND QUANTUM CAPACITANCES OF FEW LAYERED GRAPHENES THROUGH PLASMA PROCESSING 81

6.1 Introduction 81
6.2 Experimental section 82
6.3 Results and discussion 83
6.4 Conclusion 96

VII. DOPANT-CONFIGURATION CONTROLLED CARRIER SCATTERINGIN GRAPHENE 98

7.1 Introduction 98
7.2 Experimental section 102
7.2.1 N-doped bilayer graphene synthesis 102
7.2.2 Open aperture Z-scan measurement 103
7.2.3 Ultrafast degenerate pump-probe measurement 104
7.3 Theoretical section 104
7.3.1 DFT Modeling 104
7.4 Results and discussion 105
7.5 Conclusion 124

VIII. SUMMARY AND FUTURE WORK 126

APPENDICES 129

Appendix A: 130
Appendix B 133
Appendix C 140

REFERENCES 142

LIST OF TABLES

Table Page

3.1 Pore size distribution for various BAG samples obtained from BET measurements. 39

4.1 Sample descriptions for MWCNT and HCNT composite paper electrodes with and without adsorbed sodium lignosulfate (SLS). 59

6.1 Argon plasma power (P) used to systematically modulate the experimentally measured capacitance (C_{meas}) of the few-Layer graphenes, which deconvolved to yield the space-charge capacitance (C_{SC}) and the quantum capacitance (C_Q) in accordance with equations 6.1, 6.2, and 6.3. 89

7.1 Carrier relaxation times of both pristine and N-doped graphene obtained from the analysis of time resolved ultrafast pump–probe measurements. Consistent with conclusions drawn from the Raman and NLO data, S2 exhibits similar carrier–carrier (τ_1) and carrier–phonon (τ_2) relaxation times due to its graphitic N-dopant configuration. 121

LIST OF FIGURES

Figure Page

1.1 (a) (a) Classification of nanomaterials as in described in Ref. [1], (b) a high resolution transmission electron microscope (HRTEM) image of a graphene quantum dot produced by the hydrothermal method [2], (c) a scanning electron microscope (SEM) image of silver nanoparticles produced by laser ablation, (d) TEM image of helically coiled carbon nanotubes (HCNT) [3], (e) SEM image of helically coiled carbon nano wires [3], (f) a HRTEM image of single wall carbon nanotubes, (g) SEM image of a single layer graphene sheet which is shown schematically in (h). (i) An optical image of graphene foam [4], and its corresponding SEM image in (j) which reveals the foam-like structure. (k) A SEM image of a buckyaerogel which is comprised CNTs and carbon fiber (CF) [5]..... 2

1.2 (a) Schematic of a single wall carbon nanotube (a) and a multi wall carbon nanotube (b). Panel (c) shows a honeycomb lattice defined by its two unit vectors **a** and **b**, and the chiral vector $\mathbf{c}_h$ and angle θ. (d) Classification of SWNTs into metallic and semiconducting SWNTs, and their relationship to the (n, m) indices..... 6

1.3 Chemical Vapor Deposition (CVD) setup 8

2.1 Parameters of coil diameter *R*, diameter of wire *d* and coil pitch..... 14

2.2 HCNT foams and structural characteristics: (a) a SEM image of vertically aligned bundles of entangled HCNTs, (b) a TEM image of few HCNTs, (c) measured mass density gradient along the height of the HCNT foam sample, and (d) measured alignment of the HCNTs within the foam, along the height of the sample. 18

List of Figures (Continued)

Figure Page

2.3 (a) Stress–strain response of an HCNT foam subjected to five quasistatic compression cycles. (b) Variation of unloading modulus and the hysteretic energy dissipation as a function of the number of loading cycles; error bars represent the standard deviation of three samples measured. (c) Strain localization and loading history dependent response of an HCNT foam. C1–C5, C6–C10 and C11–C15 correspond to compression cycles with 0.3, 0.5, and 0.8 maximum strains, respectively. 20

2.4 SEM images showing microstructural deformation mechanisms under compression: (a) collective structural buckling of the HCNTs exhibiting brittleness in the response, (b) snap region of a bundle showing that the deformation extends to several pitches of the individual HCNTs, which changes their pristine configuration. (c) TEM images taken at turning points of pristine individual HCNTs revealing defective/broken walls. 21

2.5 Impact response of the HCNT foams. (a) Response of an HCNT foam subjected to repeated impacts at increasing velocities. (b) Dynamic stress–strain response of different HCNT foams at increasing impact velocities. (c) Dynamic unloading modulus with the impact velocity. (d) Dynamic cushion factor (peak stress divided by energy absorbed up to peak stress) with maximum strain reached on impacts. (e) Characteristic stress–time history of an HCNT foam compared to a VACNT foam with similar density; both samples were impacted at similar velocities (~3 ms^{-1}). (f) Dynamic stress–strain response of the HCNT and VACNT foams, for comparison. 26

List of Figures (Continued)

Figure Page

2.6 (a) Dynamic cushions factor with maximum strain reached on impact, (b) hysteretic energy dissipation with impact velocity, and (c) peak stress with impact velocity. 28

2.7 Stress–strain response and deformation micrographs of an HCNT foam impacted by a striker at 4.43 ms^{-1}. In the dynamic stress-strain diagram (left figure) the circled numbers identify snapshots (shown on the right) selected from the high-speed microscopic image sequence. 30

3.1 Scanning electron microscope (SEM) images of as-prepared bucky aerogels (BAGs). (a) The cross-sectional view clearly shows the layered composition of the carbon nanotubes (CNTs) and carbon fibers (CFs). The inset (i) depicts the as-prepared BAG disk, which is robust and easy to handle. The inset (ii) is the SEM image of the BAG top surface, which together with the image in (a) suggests that the BAG is predominantly an entangled microstructure containing sheets of CNTs with inter penetrating CFs. (b) Magnified image of the marked area in panel (a). 35

3.2 Panels (a) and (b) depicts a qualitative comparison of the hydrophobic and oleophilic properties of the BAG, respectively. A water droplet exhibits an apparent contact angle of ≈160° and remains on the surface of the BAG while an oil droplet (Fischer vacuum pump oil) gets fully absorbed by the BAG after wetting the BAG with an apparent contact angle of ≈35°. Note that the cosine of apparent contact angle (on a rough surface) is related to the cosine of Young contact angle (on a flat surface) through the roughness ratio. (c) Dependence of the quality factor Q on time and the macro porosity of the BAG. Evidently, the BAG comprised of the highest amount of CFs exhibits the highest Q, or absorbs the maximum oil. (d) The absorption process follows a pseudo-first order rate kinematics. The solid lines show the least square fits to the experimental data and of the corresponding rate constants (k_{p1}) for each sample are indicated within parentheses. 37

List of Figures (Continued)

Figure Page

3.3 (a) The *Q* plotted for a variety of organic liquids. (b) A SEM image of the cross-section of a burnt BAG-50 with its layered architecture (cf. Fig 3.1) left intact with no noticeable deterioration in its physical and absorptive properties.....40

3.4 Mechanical response. (a) Characteristic stress–strain responses of BAG-10, BAG-20, BAG-50 samples; the inset shows a schematic of the test setup. (b) Cyclic compression response of a BAG-10 sample. (c) Variation of peak stress values reached in consecutive cycles. (d) Variation of the energy dissipation with consecutive cycles 42

4.1 Illustrative schematic of a supercapacitor utilizing freestanding carbon "paper" electrodes fabricated with carbon nanotubes. An electrode comprising helically coiled carbon nanotubes coated with sodium lignosulfonate is shown along with a scanning electron micrograph. The chemical structure and redox functionality proposed in sodium lignosulfonate is also shown 46

4.2 Schematic of fabrication process for sodium lignosulfonate-modified buckypaper (BP) electrodes. Carbon nanotubes are dispersed in aqueous solutions with SDS or sodium lignosulfonate (SLS), sonicated at high power, and filtered to produce freestanding BP electrodes. BP electrodes are then soaked in aqueous solutions containing 40 g/L SLS, rinsed with DI water, and dried in vacuum. 54

List of Figures (Continued)

Figure Page

4.3 Physical properties of paper-like electrodes comprising helically coiled carbon nanotubes (HCNT) and sodium lignosulfonate (SLS). Scanning electron micrographs (SEM) of: HCNT electrodes fabricated using SDS as the surfactant (A); HCNT electrodes fabricated using SLS as the surfactant (B); and HCNT electrodes fabricated with SDS surfactant followed by soaking in SLS for 24 hr (C). TEM images of each respective films is shown in the inset. (D) Thermal gravimetric analysis (TGA) of composition polymer-nanotube electrodes containing HCNT with varying amounts of lignin: pure HCNT (HCNT), electrodes soaked in SLS for 24 hr (HCNT-22), HCNT papers prepared using SLS as the surfactant (HCNT-30), and these electrodes soaked in SLS for 24 hr (HCNT-36). Also shown are two other HCNT-based electrodes that were soaked in SLS for 24 hr: one prepared using a surfactant ratio of 90/10 SDS/SLS (HCNT-27) and the other with a surfactant ratio of 75/25 SDS/SLS (HCNT-29). 56

4.4 Chemical structure of lignin and representation of the oxidation reduction processes that can occur within the phenolic groups. Oxygen rich forms of lignin can have charge capacities as high as 160-170 mA hr g^{-1}. 57

4.5 Electrochemical properties of paper-like electrodes comprising sodium lignosulfate (SLS) and either MWNTs and HCNTs obtained from single electrode configurations. (A) Capacitance vs. voltage profiles for MWNT with and without 18 wt% SLS. (B) Capacitance vs. voltage for HCNT electrodes with increasing SLS wt % (0-36 wt %). (C) Peak current vs square root scan rate for select electrodes from panel b. (D) Galvanostatic discharge curves for MWNT electrodes soaked in SLS 24 hr (MWCNT-15) at varying discharge rates. (E) Galvanostatic discharge curves for HCNT and HCNT-29 electrodes at varying discharge rates. (G) Nyquist plots for HCNT electrodes with varying SLS content. The mass of HNCTs used in each film is ~2-3 mg in an area of 0.5 cm^2. 62

List of Figures (Continued)

Figure Page

5.1(a) A schematic of the spray coating set up for roll-to-roll production of carbon nanotube (CNT) coated Al electrodes (inset: scanning electron microscope image of spray coated CNTs on Al foil). (b) Scanning electron microscope cross-sectional image of CD20 Al foil showing the Al channels/ pores. (c) Upon spraying, CNT bundles are adsorbed into the Al foils and adhere well without the need of a binder. The electrolyte ions can access high surface area of entangled bundles on the surface to exhibit an increased electrical double layer capacitance. (d) A photograph of an Al electrode after CNT spray coating. The inset shows that the electrodes can be easily rolled without creating any disruption in CNT conduction network. 72

5.2 (a)–(c) Scan rate normalized cyclic voltammetry loops for two types of pristine CNTs (PCNT1 and PCNT 2) and NCNTs on CD20 Al foil. Clearly, no redox peaks are observed, indicating that the samples exhibit good electrical double layer capacitor behavior. The net capacitance of NCNTs in (c) is higher compared to PCNT1 and PCNT2 due to an increased quantum capacitance resulting from the presence of N-dopants. Quantum capacitance is directly proportional to the density of electronic states at the Fermi level ($DOS(E_F)$). N-dopants can increase the $DOS\ (E_F)$ by providing additional electrons to the honeycomb carbon lattice, and thereby result in an increase in $DOS\ (E_F)$. 74

List of Figures (Continued)

Figure Page

5.3 (a) The top panel shows a coin cell assembly for testing spray coated nitrogen doped carbon nanotube (NCNT) electrodes, while the bottom panel shows the structure of a jellyroll capacitor. (b) Cyclic voltammetry profiles of as-assembled coin cell with electrolyte of [BMIM][BF4]. (c) The charge–discharge characteristics of CD20-NCNT coin cells at 0.8 and 1 mA. (d) Ragone plot comparing the performance of CD20 NCNT coin cell and jellyroll devices with TEABF4-ACN and [BMIM][BF4] electrolytes to conventional supercapacitors, Li-thin film batteries, and other energy storage devices (see Ref. [6]), and (e) the coin cell device made from CD20-NCNT electrodes exhibited excellent cycle stability with only ~12.3% degradation in performance over 10 000 cycles. After 10 000 cycles, the Al foil current collector and NCNT material were used for the second time to make recycled electrodes. The recycled device (with recycled electrodes) exhibited 60% specific capacity (see inset) of the as-prepared NCNTs (electrodes in run-1 shown in Fig 5.3(b)) indicating excellent material recyclability..... 77

6.1 Artificial introduction of charged states in few layer graphenes. (a) Argon ion based plasma processing was used to purposefully create defects, such as dangling bond rich edge plane defects of the armchair or zigzag varieties, in few layer graphene (FLG) structures. (b) Enhanced plasma processing applied to the pristine sample, results in a substantial intensity enhancement of the *D*- and *D′*-peaks as seen in the Raman spectra (normalized to the G-peak). An increase in power, say to 50 W, may result in irreversible changes due to graphene removal. The plot of the Tuinstra−Koenig correlation length (L_a) obtained from the area integrated *D*- to *G*-peak intensity ratio is shown in the inset and indicates decreased crystallite size with increased plasma power. 84

List of Figures (Continued)

Figure Page

6.2 Atomic Force Microscopy (AFM) indicating the typical thickness of the investigated FLG samples. The figure on the right indicates a 5±1 layer FLG as has also been corroborated through electron diffraction studies. 86

6.3 Electrochemical characterization of argon plasma processed FLGs. (a) CV characterization of plasma processed FLG samples (in 0.25 M TBAHFP dissolved in a 1 M acetonitrile). The area enclosed by the CV curves was used to parameterize the C_{meas}, which increases with plasma power (indicated on the figure). (b) A close to 3-fold enhancement in the C_{meas} (left axis) and the aggregated contributions of the computed C_{SC} and the C_Q (right axis), i.e., $1/C_{gr} = 1/C_{SC} + 1/C_Q$, as a function of the plasma power. The C_{gr} is in series with the nominal double-layer capacitance and is related to the induced charged defect density. 88

6.4 Determination of the charge configurations and charge correlation length scales. (a) The energy dispersion of the *G′*-peak indicated a blue-shift and was composed of individual variation of the deconvolved $2D_1$ and $2D_2$ constituents. The laser energies, used for the Raman spectroscopy, are indicated on the individual plots. The relatively prominent left shoulder as well as the overall peak width (of ~70 cm^{-1}) seems to indicate a HOPG character to the processed FLGs. (b) The variation of the $2D_1$ and $2D_2$ peak frequency ($\omega G'$) with Raman laser energy was fit to a straight-line, as expressed through $\omega G' = aE_L + b$ with a related to the phonon velocity/Fermi velocity (v_F) ratio and b indicative of the phonon frequency at the *K*-point of the Brillouin zone. A larger change in the *a* was seen for the $2D_1$ peak and was used to infer a v_F modulation due to plasma processing. The inset shows the variation of the computed v_F with plasma power. (c) While the interlayer interaction in FLG has been implicated in a non-linear energy dispersion, for example, a hyperbolic dispersion for bilayer graphene in the vicinity of the E_F, a linear $E-k$ energy dispersion relation could be considered for insight. The plasma processing introduced positive charges akin to p-type doping into the FLG. The enhanced charge density increased the E_F from ~247 to ~661 meV (at 20 W plasma power), which was reckoned with respect to $E = 0$ point, along with a reduced v_F that was indicated by the decreased slope. (d) A charge correlation length, L_d (right axis), as deduced from the carrier density in the graphene sheet closest to the electrolyte, was smaller compared to the Tuinstra−Koenig correlation length, L_a (left axis), as deduced from Raman spectroscopy. 91

List of Figures (Continued)

Figure Page

6.5 Tuning the capacitance of FLGs through hydrogen plasma treatment. (a) A pronounced 2-fold reduction of the capacitance was observed through CV characterization of H^{3+} ion plasma exposed plasma processed samples. Such observations validate the hypothesis that hydrogen passivates the charged defect sites and reduces the capacitance tending toward the pristine state. A residual capacitance on hydrogen exposure may indicate that there may be some residual defects that resist passivation. (b) The decrease in the FLG defect density on hydrogen ion exposure was manifested in the Raman spectra through a decreased A_D/A_G ratio and an increase in the L_a. 96

7.1 (a) Different configurations of nitrogen dopants in graphene include graphitic (yellow), pyridinic (orange), and pyrrolic (blue) dopants. (b) Regarding graphene as a two-dimensional electron gas system (2DEG), the average wavelength (l) of its electrons is determined by the Fermi wavevector (k_F) $k_F \sim (2\pi n)^{1/2}$, which depends solely on the net carrier density (n). When the crystal coherence length or inter-defect spacing (L_a) is comparable to l, carriers scatter off the defects (short relaxation time τ) and the carrier mobility μ is compromised as depicted to the left of the dashed line in the above schematic. Such is the case in doped graphene, where vacancies or dopants present in non-graphitic configurations (e.g., pyrrolic N-dopants shown in purple) significantly reduce L_a due to their extended interaction volume and thereby scatter electrons (scattering shown by red and maroon colored waves) very effectively. To the contrary, dopants present in graphitic configurations (orange atoms) act as point defects and do not adversely affect τ and μ as shown schematically on the right side of the dashed line. 101

Figure Page

7.2 Raman spectra for pristine and N doped graphene (S1 – S3) obtained using 514.5 nm excitation. The *D* and *D′* bands in panel a) are intense for S1 and S3, and are attributed to N dopants present in the non-graphitic doping configuration. Notably, the *D* and *G* band intensities for S2 (graphitic doping configuration) are similar to those exhibited by pristine graphene, except for the defect-induced broadening. The electron-phonon energy renormalization upon doping results in a net downshift of the peak position of the *G′* band for S1and S3 relative to that for pristine and S2. 109

7.3 The lattice structure (top 4 panels) of pristine (a), graphitic (b), pyridinic (c), and pyrrolic (d) defects in graphene along with their electron density shown in the bottom panels. The energy released on the formation of structure from free atoms for all the configurations was found to be positive (pristine-9.90 eV, graphitic-10.22 eV, pyridinic- 9.77 eV, and pyrrolic-9.55 eV) confirming the stability of N doped configurations experimentally observed from XPS and Raman spectroscopy. 111

7.4 (a–c) Raman spectra of CVD grown samples show the presence of two peaks in *G** band ~2450 cm^{-1} in pristine samples at 3 different Raman excitations. The solid curves below the spectrum are the deconvoluted fits to the experimental data. The *G** band broadens in S2 and disappears in S1 and S3 samples due to defect-induced broadening..... 113

List of Figures (Continued)

Figure Page

7.5 (a) The Raman spectra of pristine and N-doped samples showing various combination modes between 1800–2500 cm^{-1}. Clearly, these modes broaden and disappear upon the introduction of dopants due to increase in inhomogenous broadening and electron defect scattering. The solid curves below each spectrum are the deconvoluted fits. (b) A Fourier transform of time-resolved pump–probe spectrum (discussed later in Fig. 6) showing the low-frequency Raman modes in CVD grown graphene. The broad feature ~45 cm^{-1} may be attributed the doubly degenerate (E_{2g}) shear mode shown in (c). 115

7.6 Open aperture Z-scan data for pristine graphene, S1, S2 and S3 collected with the (a) ns and (b) fs excitations. The on-axis peak intensity (I_o) is 0.16 GW cm^{-2} and 12.5 TW cm^{-2}, respectively. Solid lines represent theoretical fits to the experimental data obtained from eqn (1) (see text for details). Panels (c) and (d) show the variation of saturation intensity (I_s) and the 2PA coefficient (b) obtained from the best fit curves to the Z-scan data in panels (a) and (b). Both I_s and β are higher for non-graphitic dopant configuration due to the larger defect density arising from pores and arm-chair like edges (cf. Fig. 3(a)). 117

List of Figures (Continued)

Figure Page

7.7 (a) Time-resolved differential transmission spectra for pristine graphene and S1–S3 obtained through a degenerate pump–probe method using 70 fs pulses of 780 nm excitation wavelength. Solid lines represent the bi-exponential fits based on carrier–carrier and carrier– phonon scattering time scales (see Table 1). The inset shows the parabolic energy dispersion for bilayer graphene and the arrow indicates excitation of electrons from the valence to the conduction band. (b) Under intense photo-excitation, the non-equilibrium carrier distribution (in the *E–k* space depicted by the parabolic energy dispersion in the inset shown in (a)) results in an initial rise in the transmitted intensity. The carriers (electron and hole distribution shown in blue and orange respectively) equilibrate by carrier–carrier scattering on a timescale τ_1. Subsequently, the carrier thermalization and decay occur through carrier–phonon scattering on a timescale τ_2. ..... *120*

CHAPTER ONE

INTRODUCTION

Nanomaterials are defined as materials with at least one of its physical dimensions in the size ranging from 1-100 nanometers. Due to the high aspect ratio, surface morphology, and crystallinity of nanomaterials, they have attracted a great deal of attention both from the fundamental properties and applications standpoints. Notably, nanomaterials research continues with renewed interest due to an increasing volume of discoveries about their unique optical, magnetic, electrical, and other properties, which are generally absent in the corresponding bulk materials. When the dimensions of a material is shrunk to the nanometer scale, their surface area and spatial confinement will change, and will be accompanied by new imperfections (defects) that did not exist in their bulk forms. Some nanomaterials occur naturally, nonetheless scientists are particularly interested in engineered nanomaterials, which are deliberately produced with controlled shape, size, surface morphology, *etc.,* for creating a platform through which in-depth knowledge of fundamental science and novel applications can be explored.

Nanostructured materials (Fig 1.1(a) [1]) are classified as zero dimensional (quantum dots, Ag nanoparticles, *etc.* Fig 1.1(b-c)), one dimensional (carbon nanotubes (CNT), Si nonowire, *etc.* Fig 1.1(d-f)), two dimensional (graphene, single layer MoS_2, *etc.* Fig 1.1(g-h)), and three-dimensional nanostructures (graphene foam, CNT sponge, *etc.* Fig 1.1(i-k)).

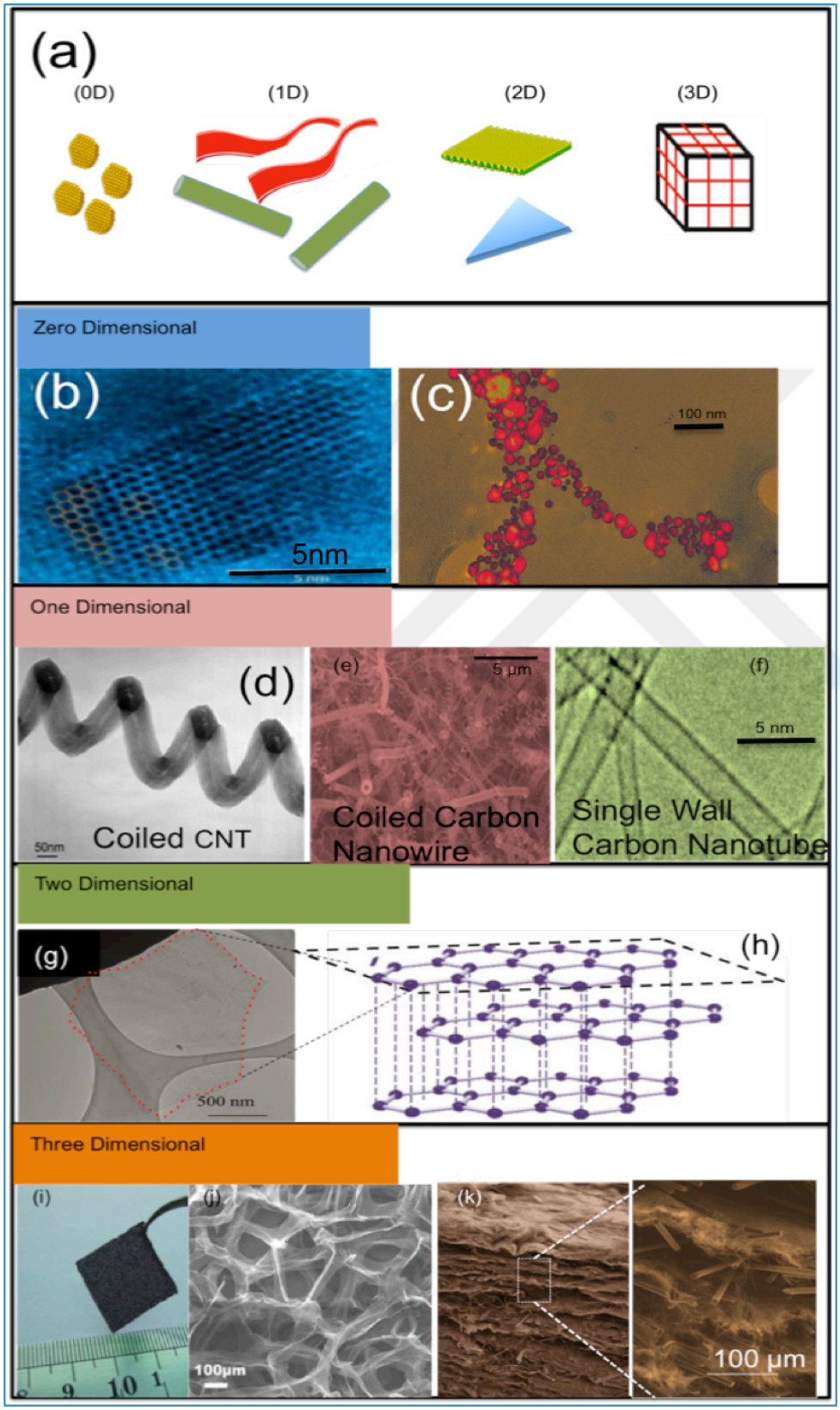

(a)
(0D)
(1D)
(2D)
(3D)
Zero Dimensional
(b)
5nm
(c)
100 nm
One Dimensional
(d)
50nm
Coiled CNT
(e)
5 µm
Coiled Carbon Nanowire
(f)
5 nm
Single Wall Carbon Nanotube
Two Dimensional
(g)
500 nm
(h)
Three Dimensional
(i)
(j)
100µm
(k)
100 µm

Figure 1.1: (a) Classification of nanomaterials as in described in Ref. [1] (b) a high resolution transmission electron microscope (HRTEM) image of a graphene quantum dot produced by the hydrothermal method [2], (c) a scanning electron microscope (SEM) image of silver nanoparticles produced by laser ablation, (d) TEM image of helically coiled carbon nanotubes (HCNT) [3], (e) SEM image of helically coiled carbon nano wires [3], (f) a HRTEM image of single wall carbon nanotubes, (g) SEM image of a single layer graphene sheet which is shown schematically in (h). (i) An optical image of graphene foam [4], and its corresponding SEM image in (j) which reveals the foam-like structure. (k) A SEM image of a buckyaerogel which is comprised CNTs and carbon fiber (CF) [5].

1.1 Carbon Nanomaterials

Carbon is one of the basic elements for life on Earth and plays a key role in the Earth's evolutions. Carbon atoms participate in robust covalent bonds with other carbon atoms in various hybridization states (sp, sp^2, sp^3) or with nonmetallic elements. It exists in diverse allotropic forms with graphite and diamond as the two natural allotropes of carbon. Although diamond and graphite both consist exclusively of carbon atoms, their physical and chemical properties are very different. Diamond favors a C− C sp^3 hybridization, which makes it the hardest natural 3D material whereas graphite favors C−

C sp^2 hybridization, which makes graphite as a 2D solid lubricant due to weak van der Waals interactions between its graphene sheets. Diamond is a transparent electrical insulator, and conversely graphite is a black opaque soft material with remarkable electrical conductivity. In the last three decades, new allotropes of carbon nanomaterials were discovered including the 0D fullerenes, 1D CNTs, and 2D graphene.

1.1.1 Carbon Nanotubes

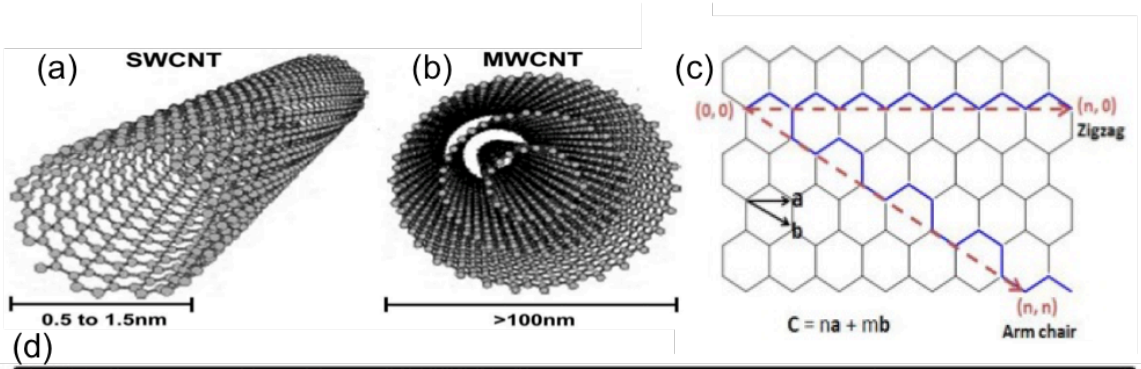
Carbon nanotubes (CNTs) are one of the most promising materials with their high strength, elasticity and electric conductivity for novel applications, for example, composite materials. CNTs have attracted an enormous attention since their discovery by Iijima in 1991 [7]. Since its discovery, theoretical and experimental studies in different fields (mechanics, optics, electronics) have focused on both fundamental physical properties and the potential applications of nanotubes. Topologically, a CNT is a hollow cylinder (~1 nm in diameter and ~μm in length) of a graphene sheet with quasi-one dimensional with translational periodicity along the tube axis. There are two types of CNTs: (i) single-walled carbon nanotubes (SWCNTs) (Fig. 1.2(a)) and (ii) multi-walled carbon nanotubes (MWCNTs) (Fig. 1.2(b)). SWCNTs have a single graphene roll, however MWCNTs have more than one concentric rolled graphene sheets. Most of the CNTs are in MWCNTs form. MWCNTs interwall spacing is typically ~0.34 nm, but this can be little bit higher depending on diameter and the number of walls [8]. A single-walled CNT (SWCNT) can be considered as a single molecule and shows a great deal of

diversity in structure including diameter, length, and chirality. The diameter and chirality of a SWCNT is governed by its so-called (n, m) indices that define the chiral vector c_h = n$\boldsymbol{a}$ + m$\boldsymbol{b}$ which connects crystallographically equivalent sites in a two-dimensional graphene sheet (Fig. 1.2(c)). The vectors $\boldsymbol{a}$ and $\boldsymbol{b}$ are the unit vectors in the honeycomb lattice, as indicated in Fig. 1.2(c), and n and m are integers. Using simple geometry, the diameter D and the chiral angle θ of a SWNT can be expressed as,

$$D = a(n^2 + nm + m^2)^{1/2}/\pi \quad (1.1)$$

$$\theta = tan^{-1}\left[3^{1/2}m/(m + 2n)\right] \quad (1.2)$$

When n = m, the chiral angle θ collapses to zero, and the resulting CNT represents an armchair CNT. On the other hand, when n = m, the chiral angle is 30^o, and the resulting CNT is an armchair CNT. For $0 < \theta < 30$, the resulting CNTs are called chiral CNTs. Both theory and experiments have shown that the electrical properties of CNTs depend on their diameters and chiralities (Fig. 1.2 (d)). If (2n + m) is a multiple of 3, the CNTs exhibit a metallic behavior, and if not, they exhibit a semiconducting behavior. Multi walled CNTs (MWCNTs), because of the dominant properties of their metallic shells, are predominantly metallic.



(d)

(n,m)	Form of SWNTs	Electrical Conductivity
(n,0)	Zigzag	Metallic when n is the multiple of 3, otherwise, semiconducting
(n,n)	Armchair	Metallic
(n,m) when m≠0, and n	Chiral	Metallic when (2n+m)/3 is an integer, otherwise, semiconducting

Figure 1.2: Schematic of a single wall carbon nanotube (a) and a multi wall carbon nanotube (b). Panel (c) shows a honeycomb lattice defined by its two unit vectors **a** and **b**, and the chiral vector $\mathbf{c}_h$ and angle θ. (d) Classification of SWNTs into metallic and semiconducting SWNTs, and their relationship to the (n, m) indices.

By introducing defects within the honeycomb lattice, novel mechanical, optical and electronic properties can be elicited [9]. Murata *et al.* observed observed super-conductivity in boron doped SWCNTs at 12 K, which is absent in pristine SWCNTs [10]. Morphological defects as in helically coiled MWNTs, which is absent or present to a negligible extent in MWNTs, are found to change the overall mechanical and electro-chemical properties respect to straight CNTs [3].

1.1.2 Carbon nanotubes Synthesis

Following Iijima's discovery of nanotubes in his electric arc generated soot,[7], CNT the exploration of synthesize methods escalated rapidly. CNTs have also been synthesized via the pulsed laser deposition (PLD) or chemical vapor deposition (CVD). Two types of CVD method are widely used - the plasma enhanced CVD (PECVD) and the thermal CVD. The thermal CVD method has been used to produce large amount of CNTs production due to its simple design for high production rate of CNTs.

Transition metal (Fe, Co, Ni) nanoparticles are ideal for catalyzing carbon in a CVD, PLD or electric arc process, and serve as templates for seeding the growth of CNTs. Firstly, the vaporized hydrocarbon source (acetylene, methane, etc.) is adsorbed and decomposed on the surface of the metal catalyst nanoparticles. The absorbed carbons start to dissolve into and diffuse around the metal catalyst nanoparticles. Under hydrocarbon flow, the dissolved carbon precipitates on the surface of the metal catalyst nanoparticles and results in the formation of CNTs. The morphology and crystallinity of resulting CNTs are dependent on the reaction temperature, chemical composition and size of the nanoparticle, hydrocarbon source, etc. The metal catalyst nanoparticles can be deposited on the substrate as a thin film prior to loading the substrates in the furnace, or can be deposited during synthesis in the vapor phase. The former approach can result in the growth of very pure CNTs with a controlled morphology. The thin film of catalyst

nanoparticles can be prepared either via dip coating, [11], sputtering [12], thermal evaporation of metal catalyst and electron beam evaporation [13]. In the latter method (the vapor-phase approach), the precursor is prepared by dissolving appropriate amounts of metallocenes (such as ferrocene or cobaltocene) in organic solvents (such as benzene, xylene). The Fe or Co atoms are released from the corresponding metallocene at temperatures above 500 ^{o}C and form nanosized clusters which subsequently seed the growth of CNTs [14]. By carefully controlling the synthesis parameters such as gas flow rates, temperature, gas compositions, catalyst types, *etc.*, researchers have been successful in controlling the length, diameter, and alignment of CNTs. CNTs grow on a support substrate such as quartz, SiO_2/Si wafer, and stainless steel, and when several MWNTs grow in an aligned fashion on the substrates, they are referred to as vertically aligned MWNTS (VACNTs) or a forest of MWNTs. A schematic of a typical CVD setup for the growth of a MWNT forest is shown in Fig. 1.3.

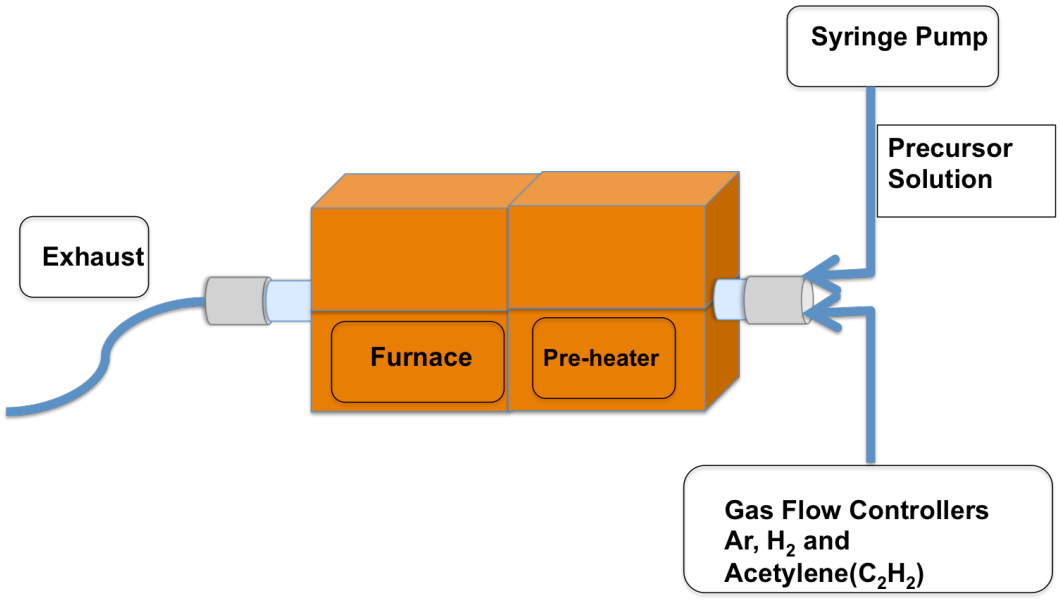


Figure 1.3: Chemical Vapor Deposition (CVD) setup

Continuous production of CNTs for scalable manufacturing of current electrodes, and carbon nanotube paper (buckypaper) have also been demonstrated. Atkinson *et al.* [15] have demonstrated a scalable production of CNT yarns which are potentially useful in applications such as mechanical actuators for artificial muscles, flexible conductors for sensors embedded in textiles, flexible batteries and solar cells.. Polsen *et al.* showed continuous production of vertically aligned CNTs on Si wafer [16]. Arcile-Velez *et al.* synthesized VACNTs on roll of aluminum foil to demonstrate scalable and continuous production of MWNTs and their use as current collectors in energy storage devices [17].

1.2 Defects in carbon nanotubes

CNTs have been widely investigated for their combined mechanical, electronic and thermal properties. Theoretical and experimental studies indicate that CNTs exhibits high Young's modulus, tensile strength, and electrical conductivity. Besides that, researchers are also interested in introducing defects in CNTs to tune their mechanical, electronic and thermal properties. These defects can be morphological, chemical or both. Defects such as pentagons, heptagons, vacancies, or dopant are found to drastically alter the electronic properties of these nano-systems. The introduction of defects in the carbon network is thus an interesting way to tailor its intrinsic properties, with a view towards creating new nanodevices.

1.2.1 CNTs in different morphology

CNTs with different morphology have their own special properties and potential applications. CNTs with many different morphologies (straight, wavy, coiled, and branched) have been reported in the literature. In VACNTs arrays, the CNTs grow in the perpendicular direction to the substrate. Typical diameter of a CNT within a VACNT sample is ~30 nm, while its height can range from hundreds of microns to millimeters. Due to their high Young's modulus, tensile strength and lightweight, the VACNTs are an attractive candidate for impact protection devices. Lattanzi *et al.* synthesized micro-patterned VACNTs and performed impact tests at different strain rates.[18]. The energy absorption of the micro-patterned VACNT foams was higher than most other energy absorbing materials with comparable density.

In contrast to the straight MWNTs that are present in a VACNT, the helically coiled CNTs (HCNTs) exhibit a helical morphology. The most common method to grow HCNTs is the thermal CVD method in which two or more catalyst nanoparticles are used [19]. Wang *et al.* showed that by using Fe-In and Fe-Sn catalyst (Indium isopropoxide and Tin isopropoxide are dissolved in xylene-ferrocene mixture) vertically aligned helically coiled CNTs can be synthesized on SiO_2/Si substrates [3]. The growth mechanism of HCNTs is not well understood and researchers are still striving to understand the role of the dual catalysts. One proposed mechanism by Bandaru *et al.* suggests that HCNT growth is dependent on the use of certain catalysts combinations

[20]. They considered the interfacial tension between the metal catalyst and graphite surface, also known as wettability, and found it to be an important factor to promote coiling of CNTs. Liquid metals such as Sn, In, and Cu, which are known to induce coiling have larger wetting angles (>150°), whereas Ni, Fe and Co which mostly produce linear carbon materials have smaller wetting angles (< 75°). Fe catalyst promotes CNT growth, whereas carbon atoms that interact with the In or Sn catalysts, the CNT prefer to orient themselves in a direction that avoid wettability of the catalyst, and results in an helical growth. HCNTs can have different coil diameter, coil pitch and nanotube diameter. These parameters will affect the mechanical, electronic and thermal properties of HCNTs. Coiled CNTs are interesting because their unique morphology enables them to be used as, sensors, resonators, nanoscale mechanical springs and electrical inductors.

Another morphology of the CNTs is the branched CNTs. Different branching configurations (Y, T and L shape CNTs) have been reported in the literature [21]. As explained above, in addition to the dependence of the electrical properties of CNTs on the tube chirality and diameter, useful logic functionality has been achieved at the junction of metallic and/or semiconducting CNTs [22,23].

1.2.2 Chemical defects in CNTs

The most common dopants for CNTs are boron, nitrogen and sulfur, which can be incorporated into the nanotube framework either during synthesis, or during post-synthesis [24]. B, N and S doping not only change the chemical properties but also

change morphology of CNTs. For example, Jang *et al.* [25] and Savage et al. [26] investigated the effects of nitrogen doping and discovered the emergence of the bamboo-shaped CNTs. Similar strategies are now being used to dope graphene by several groups around the globe.

1.3 Summary

This dissertation focuses on the synthesis, properties and applications of defect introduced CNTs. Firstly, the remarkable mechanical properties of HCNTs arrays will be compared to the corresponding properties of VACNTs, which suggests that the former are useful for impact protection of shock-sensitive devices. The enhanced energy dissipation properties of HCNT arrays will be elucidated through a detailed examination of the impact-induce microstructural changes of individual HCNTs. In chapter 3, I present a CNT/Carbon fiber (CF) composite and investigate its oil absorption capacity and mechanical properties. In chapter 4, the electro-chemical properties of HCNT composites coated with redox polymer will be discussed. In chapter 5, I show that nitrogen doping in CNTs enhances the capacitance of a device (supercapacitor) over that of a similar device made of pristine CNTs. I also demonstrate scalable production of the CNT electrodes on aluminum foils for use as electrodes in supercapacitors. In chapter 6, defects in the graphene induced by reactive ion etching (RIE) will be discussed, and its role in enhancing its capacitance will be elucidated. Finally, in chapter 7, I will elucidate the influence of substitutional N-doping on the electronic, vibrational, and optical properties of CVD grown bi-layer graphene.

CHAPTER TWO

ANOMALOUS IMPACT AND STRAIN RESPONSES IN HELICAL CARBON NANOTUBE FOAMS

2.1 Introduction

Helically coiled carbon nanotubes (HCNTs) have previously been synthesized in several forms, including individual fibers [27], self-assembled ropes [28], or in macroscopic arrays [3,29]. Small-scale HCNT fibers have been synthesized for a variety of potential applications such as nano-electronics, nano-mechanical systems [30], self-sensing mechanical resonators [31], reinforcement in epoxy based composites [32,33], energy applications including fuel cells, hydrogen storage, and super-capacitors [34,35]. Macroscopic arrays of HCNTs have been suggested for applications such as flat panel field emission displays [36], electromagnetic shielding [37], and energy dissipative cushioning and packaging [38]. However, unlike non-helical vertically aligned carbon nanotube (VACNT) arrays [39,40], studies on the mechanical response of bulk HCNT foams are sparse in the literature [32,33,38,41], and their fundamental deformation mechanisms at different loading rates are not yet fully characterized.

Bulk HCNT foams derive their unique mechanical properties from their hierarchically organized microstructure, characterized by aligned and entangled helical coils of multi-walled CNTs. Their mechanical properties are governed by the unique

behavior of individual nanocoils as well as the collective response of the interacting and entangled neighbors. The carbon nano-coils act like elastic springs, with their deformation behavior governed by geometric nonlinearity. The spring constant (*k)* of a helical coil is proportional to the quadratic power of the diameter (*d)* of the coiled wire (CNT diameter) ($k \propto d^4$), and inversely proportional to the cube of the radius (R) of the coil ($k \propto 1/R^3$) in Fig. 2.1 [42].

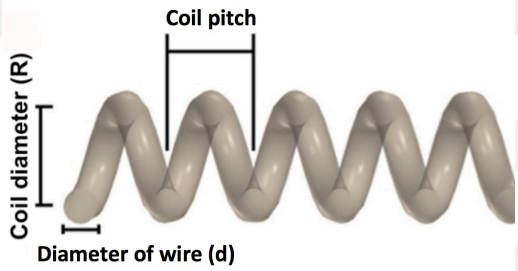


Figure 2.1: Parameters of coil diameter *R*, diameter of wire *d* and coil pitch

Such geometric nonlinearity in the deformation of the individual nano-coils leads to an interesting collective mechanical response in the HCNT foams. For example, the contact interaction of a spherical indenter with HCNT foams is highly nonlinear and non-Hertzian, and different from the contact interaction of a spherical indenter with VACNT foams. This highly nonlinear collective response is attributed primarily to the unusual entanglement between neighboring coils and to the collective bending behavior of the coil tips when impacted by a spherical indenter [43]. The HCNT foams have been shown to mitigate low velocity (0.2 ms^{-1}) impact forces efficiently and fully recover deformation of the order ~5 mm (5% strain). However, their fundamental deformation mechanisms at large strains and at different strain-rates have not been studied yet. In this chapter, we

present a comprehensive study of the mechanical response of HCNT foams in both quasistatic and dynamic loading regimes with structural characterizations. We performed structural characterization using synchrotron X-ray scattering and mass attenuation, and correlated the structural characteristics to the observed fundamental deformation mechanisms under compressive loading. We used *in-situ* high-speed microscopy, and *ex-situ* scanning electron microscopy (SEM) and transmission electron microscopy (TEM) to identify the deformation mechanisms that govern the bulk mechanical behavior.

2.2 Experimental methods

2.2.1 Synthesis

HCNT foams were synthesized using a two-stage thermal chemical vapor deposition (CVD) process. The two stages in our CVD reactor: the preheater and the furnace were maintained at 200 and 700 °C respectively. Silicon wafers (3 cm x 3 cm) were then placed in the CVD reactor and heated from room temperature to reaction temperature in the presence of an Ar (flow rate of 500 sccm (cubic centimeters per minute at standard temperature and pressure)) and an H_2 flow rate of 100 sccm. The rate of temperature increase was 15 °C min^{-1} during heating. Ferrocene and xylene were used as the catalyst precursor and carbon source respectively. Indium (In) and Tin (Sn) sources (indium isopropoxide and tin isopropoxide) were dissolved in a xylene–ferrocene mixture where the ratio of C : Fe : In : Sn was maintained at 99.16 : 0.36 : 0.1 : 0.38, which was then continuously injected into the quartz tube CVD reactor using a syringe

pump at an injection rate of 1.5 ml h^{-1} after reaching the desired temperature. Simultaneously, acetylene along with Ar carrier gas was passed into the CVD reactor at atmospheric pressure with flow rates of 50 sccm and 500 sccm respectively. Subsequently, after ca. 1 hour of reaction time, the syringe pump and acetylene injection were shut off and the CVD reactor was allowed to cool to room temperature under a flowing Ar atmosphere. The HCNTs were grown on silicon wafer substrates that were placed inside the furnace tube prior to the synthesis run. The resultant HCNT foams were ~1 mm in height.

2.2.2 Mechanical characterizations

The quasistatic compression tests were performed on an Instron ElectroPulse E3000 testing system. All the quasistatic experiments were performed at 0.01 s^{-1} strain rate. The dynamic experiments were performed on an impact testing setup developed in Dr. Daraio's laboratory at Swiss Federal Institute of Technology (ETH Zurich) [44]. The experimental setup delivers flat plunge striker impacts on the test specimens at controlled velocities. Geometric Moire´ transducer was used for microscale dynamic displacement measurements while a PCB piezotronic impact force sensor measured the impact force. A high-speed microscope was used for *in-situ* visualization and characterization of the micro-scale deformation mechanisms.

2.2.3 Sample preparation for transmission electron microscopy (TEM)

Samples for TEM imaging were prepared by dispersing HCNT arrays in a 2% sodium dodecyl sulfate (SDS) solution [45] using tip sonication. A drop of the HCNT suspension was transferred to a holey carbon grid for the TEM. The grid was viewed on a Hitachi 7600 TEM at Microscope facilities at Clemson University.

2.3 Morphology and structure

The HCNT foams used in this study were synthesized on Si substrates using a chemical vapor deposition (CVD) process as described in the experimental methods section. SEM images of the foam's microstructure reveal the uniformity of the coiling and pitch of the HCNTs present in the array (Fig. 2.2(a)). A TEM image showing a representative nano-coils found in our HCNT foams can be seen in Fig. 2.2(b). The overall thickness of the HCNT foams studied was ~1 mm and the dominant HCNT diameter and pitch were around 25± 5 nm and 150 nm respectively. We performed small-angle X-ray scattering (SAXS) and mass attenuation measurements using a synchrotron light source to nondestructively quantify the HCNT density and alignment. We used an incident photon energy of 10 keV with a beam height of less than 300 mm at the sample in order to spatially map structural characteristics along the vertical height of the HCNT foams. Monitoring the drop in X-ray intensity across the sample enabled the determination of the sample's mass density using the Beer–Lambert law [46]. The mass

density was found to decrease linearly with the height of the HCNT foam (with the lowest density found on the side of the foam adjacent to the substrate). The foam's average density was 0.15 g cm^{-3} with a 59% variation along its height (Fig. 2.2(c)). The HCNT alignment was quantified from the anisotropy of the SAXS patterns, using Herman's orientation factor (*f*)[47,48], where *f* equals 1 for perfectly aligned CNTs and 0 for random order (no alignment).

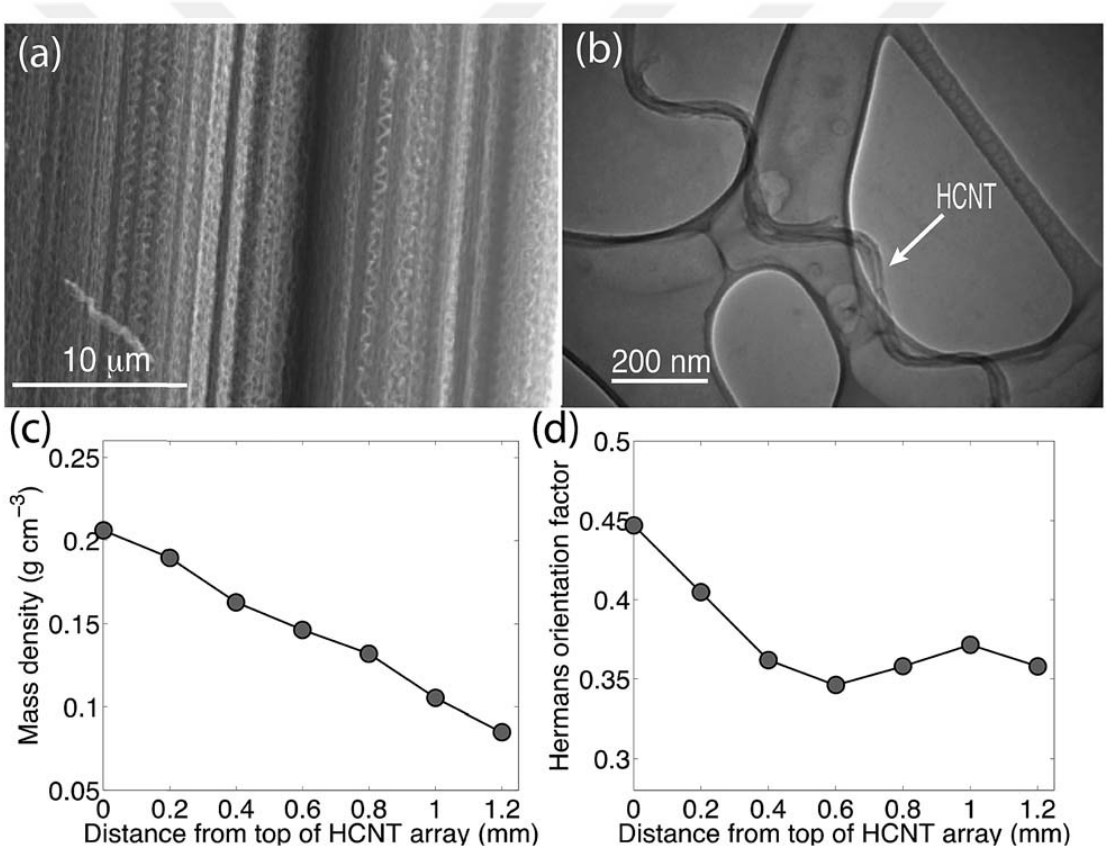


Figure 2.2: HCNT foams and structural characteristics: (a) SEM image of vertically aligned bundles of entangled HCNTs, (b) TEM image of few HCNTs, (c) measured mass

density gradient along the height of the HCNT foam sample, and (d) measured alignment of the HCNTs within the foam along the height of the sample.

We found that the alignment decreased from the top to the bottom of the sample, with the bulk samples having an average alignment of 0.38 (Fig. 2.2(d)). Although the HCNTs are generally aligned in the vertical direction, their coiled nature yields a projected zigzag structure, which results in a low Herman's orientation factor. The statistical distribution of orientation angles arising from the helical nano-coils is highlighted in the 2D SAXS patterns (Appendix A: Fig. 1(b)). Details of the synchrotron X-ray scattering experimental methods and analysis can be found in Appendix A.

2.3.1 Quasistatic response

We tested the HCNT foams under quasistatic compression cycles at 0.01 s^{-1} strain rate. The HCNT foams exhibit a hysteretic, nonlinear stress–strain response (Fig. 2.3(a)) when subjected to quasistatic compressive loading–unloading cycles, similar to the response reported for other typical foam materials [49] as well as VACNT foams [39]. The area enclosed by the hysteresis loop represents the energy dissipated at each compression cycle ($W_{dissipated}$ in Fig. 2.3(b)). The HCNT foams also have the ability to recover large compressive strains of up to 80%. When a HCNT foam is compressed multiple times, the loading path differs from cycle to cycle, a characteristic behavior found in materials with preconditioning effects (Fig. 2.3(a)). The preconditioning is

pronounced in the first three loading–unloading cycles, but the mechanical response stabilizes after the third cycle. A similar preconditioning effect was also reported in VACNT foams and was attributed to microstructural rearrangements of the CNTs during the loading–unloading cycles [39,50].

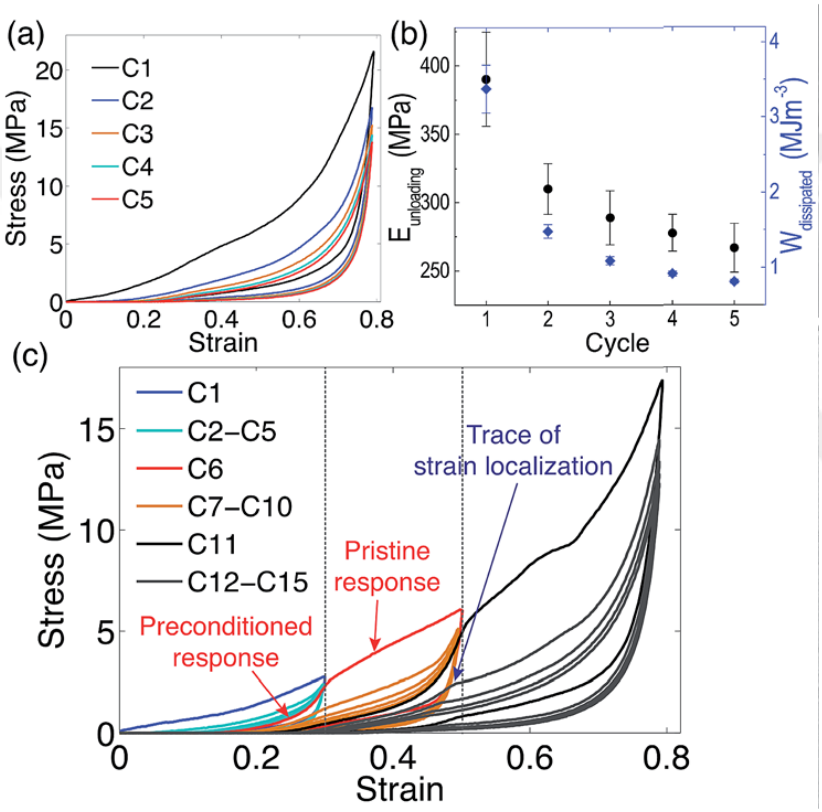


Figure 2.3: (a) Stress–strain response of an HCNT foam subjected to five quasistatic compression cycles. (b) Variation of unloading modulus and the hysteretic energy dissipation as a function of the number of loading cycles; error bars represent the standard deviation of three samples measured. (c) Strain localization and loading history dependent response of an HCNT foam. C1–C5, C6–C10 and C11–C15 correspond to compression cycles with 0.3, 0.5, and 0.8 maximum strains, respectively.

In the case of HCNT foams, in addition to the microstructural rearrangements, we also observed permanent microstructural damage and brittle fracture of HCNT bundles in the deformed region (Fig. 2.4(a)). The unloading modulus, the hysteretic energy dissipation (Fig. 2.3(b)), and the peak stress also decrease rapidly within the first three cycles and remain nearly constant for the later cycles, implying that the mechanical properties of HCNT foams are loading-history dependent.

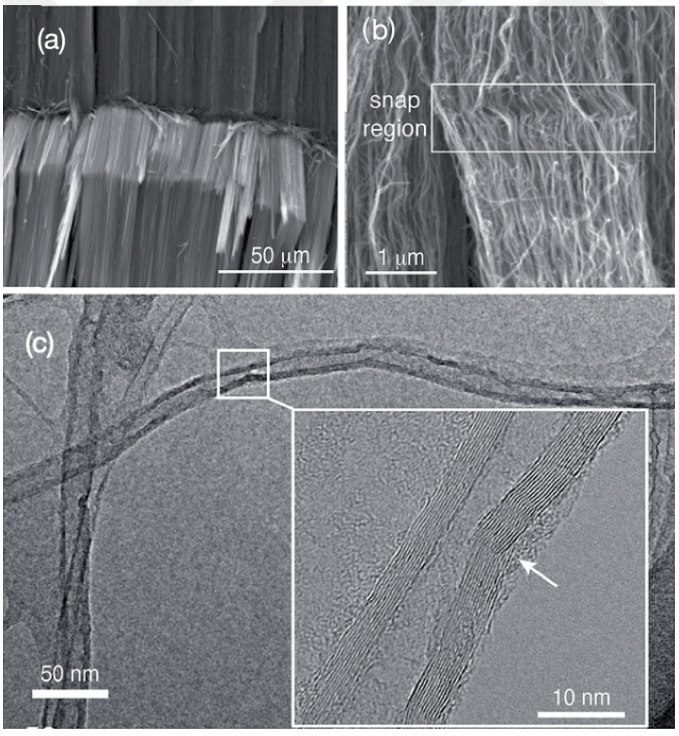


Figure 2.4: (a and b) SEM images showing microstructural deformation mechanisms under compression: (a) collective structural buckling of the HCNTs exhibiting brittleness in the response, (b) snap region of a bundle showing that the deformation extends to several pitches of the individual HCNTs, which changes their pristine configuration. (c)

TEM images taken at turning points of pristine individual HCNTs revealing defective/broken walls.

The compressive strength (peak stress at 80% strain) of the HCNT foams (22.2±1.4 MPa) and the hysteretic energy dissipation (3.38±0.32 MJ m^{-3}) are comparable to that of the VACNT foams with similar densities [51].

When an HCNT foam that was subjected to repeated cyclic loading at a moderate strain was compressed beyond the previous maximum strain (30%), the loading path changed from the preconditioned path to the pristine sample's loading path (Fig. 2.3(c)). This change from preconditioned to pristine response suggests that the strain in the sample is localized and the deformation is not uniform. These regions of strain localization (occurring during the first cycle) are also identifiable in the consecutive cycles (second and later cycles), as indicated in Fig. 2.3(c). This kind of strain localization was also observed for VACNT foams, where the vertically aligned bundles of CNTs undergo a well-defined sequential periodic buckling that is governed by the intrinsic density gradient within the material [39,52–54]. However, the strain localization in HCNT foams is surprising, since previous studies suggested primarily a spring-like bulk compressive behavior. We correlate this response to the HCNT foam's microstructure, consisting of long entangled HCNTs with length (l ~ 1 mm) three orders of magnitude greater than the coil diameter (d_{coil} ~ 450 nm) [37]. Due to (i) the very high aspect ratio (l/d_{coil} ~ 2000), (ii) the entanglement with neighboring coils, and (iii) the

vertical alignment of HCNT bundles, the deformation is localized rather than the whole HCNT foam undergoing a uniform deformation. *In-situ* microscopy and *ex-situ* SEM characterization of a HCNT foam under compression revealed that the strain initially localizes near the substrate where the sample's density is the lowest. After a critical strain of ~10%, localization begins to appear in different regions along the sample's height, without any periodic sequential progression. Several consecutive structural buckles with observable brittleness follow the initial deformation (Fig. 2.4(a)). The SEM images also reveal the presence of several permanent microstructural deformations and HCNT bundles that underwent brittle fracturing during loading. TEM analysis of pristine (as-grown) HCNTs show that the pristine nano-coils have numerous structural defects: the multiwalled HCNTs have highly deformed or defective walls as indicated by arrow in Fig. 2.4(c). The presence of a large number of such nanoscale defects present in the pristine samples may have led to the fracture of the bundles when compressed. Despite the microstructural damages, the bulk samples show significant recovery upon unloading. This suggests that the interactions among HCNT bundles at the mesoscale play a dominant role in the bulk response of foams, and are more important than the nanoscale permanent damages observed in the individual coils.

The presence of quasistatic compression-induced strain localization, at arbitrary regions along the height of the sample, also implies that the influence of the intrinsic density gradient along the thickness of the foam is less significant compared to the influence of the nanoscale defects described above. A closer look at the stress–strain

response of the HCNT foams (Fig. 2.3(c)) shows that the transition regions from preconditioned to pristine loading paths are smooth—in contrast to the sharp transitions observed in VACNT foams [54]. This implies that the strain localization in HCNT foams is not confined to a narrow region of the foam's thickness (as in the case of the well-defined periodic sequential buckles forming in VACNT foams), but the deformation extends to several adjacent pitches of the individual HCNTs. This is also evident from SEM images obtained on a compressed sample where several adjacent pitches of the individual helical coils are distorted by bending, buckling and twisting (Fig. 2.4(b)). Due to these drastically different deformation mechanisms, the loading path of the stress–strain diagram does not show any saw-tooth plateau region with local stress rise and drop, which is a typical characteristic of the formation of localized periodic sequential instabilities [39,53].

2.3.2 Dynamic response

To study the dynamic response of HCNT foams, we performed controlled impact experiments using a flat plunge striker [44]. In the dynamic regime, the HCNT foams exhibit a nonlinear stress–strain response with a hysteresis loop (Fig. 2.5(a) and (b)), similar to the response observed in the quasistatic regime. Fig. 2.5(a) shows the stress–strain response of an HCNT foam that was impacted repeatedly at increasing velocities. The stress-strain diagrams show the presence of preconditioning effects and strain localization. Similar to the quasistatic response, the preconditioned loading path returns

to the pristine loading path as soon as the previous maximum strain is exceeded. In addition to conforming the strain localization in dynamics, this observation suggests that the dynamic loading response is rate-independent. We further verified the rate-independent nature of the loading response of HCNT foams by testing different HCNT foams at controlled impact velocities, between 1 ms^{-1} and 6 ms^{-1} (Fig. 2.5(b)). The stress–strain diagrams followed similar loading paths for the samples tested at increasing velocities (Fig. 2.4(b)). The dynamic unloading modulus increases with increasing impact velocities, due to the samples reaching higher maximum strains (and densification) with increasing impact velocities (Fig. 2.4(c)). The dynamic unloading moduli measured were nearly half of the quasistatic unloading moduli (at 0.8 strain), suggesting that HCNT foams are more compliant in the dynamic state than in the quasistatic state. This dynamic effect may have arisen from the faster, spring-like pushback response of HCNT foams during striker impacts.

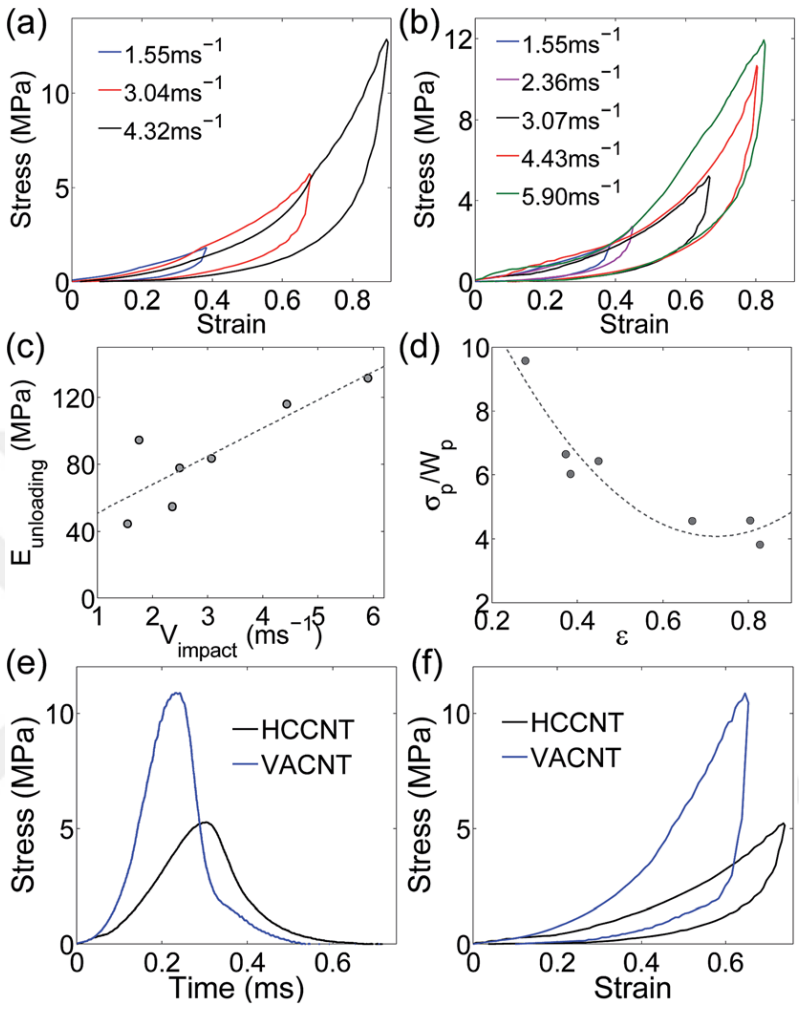


Figure 2.5: Impact response of the HCNT foams. (a) Response of an HCNT foam subjected to repeated impacts at increasing velocities. (b) Dynamic stress–strain response of different HCNT foams at increasing impact velocities. (c) Dynamic unloading modulus with the impact velocity. (d) Dynamic cushion factor (peak stress divided by energy absorbed up to peak stress) with maximum strain reached on impacts. (e) Characteristic stress–time history of an HCNT foam compared to a VACNT foam with similar density; both samples were impacted at similar velocities (~3 ms^{-1}). (f) Dynamic stress–strain response of the HCNT and VACNT foams, for comparison.

To show the ability of the HCNT foams to cushion dynamic impacts, we plot the variation of the dynamic cushion factor with the maximum strain reached on impact (Fig. 2.5(d)). The dynamic cushion factor is calculated by dividing the peak stress by the energy absorbed by the sample up to the peak stress. A decrease in peak stress and/or an increase in energy absorption reduce the dynamic cushion factor—characteristics that would be beneficial in impact-protective applications. The dynamic cushion factors of HCNT foams are comparable to those of VACNT foams with similar densities [40]. Fig. 2.6(a) presents a comparison of the dynamic cushion factor obtained in HCNT foams and VACNT foams with comparable densities. Even though the HCNT foams and VACNT foams exhibit similar dynamic cushion factors, it should be noted that the VACNT foams exhibit higher hysteretic energy dissipation (Fig. 2.6(b)), by reaching higher peak stresses for a given impact velocity. HCNT foams, however, perform better in damping the impact stress amplitude in the considered range of impact velocities (Fig. 2.6(c)). This improved damping for the HCNTs is also evident from the comparison of characteristic dynamic stress–time histories (Fig. 2.5(e)), and dynamic stress–strain diagrams (Fig. 2.4(f)), for HCNT foams and VACNT foams impacted at similar velocities (2.99 ± 0.07 ms^{-1}). At this impact velocity (2.99 ± 0.07 ms^{-1}), the HCNT foams show ~53% improved impact stress damping over the VACNT foams. The HCNT foams deform more at moderate stress levels and the stress profiles span over a longer duration than the VACNT foams. This demonstrates that HCNT foams mitigate impacts more effectively

by reducing the amplitude of transmitted stresses in the considered range of impact velocities.

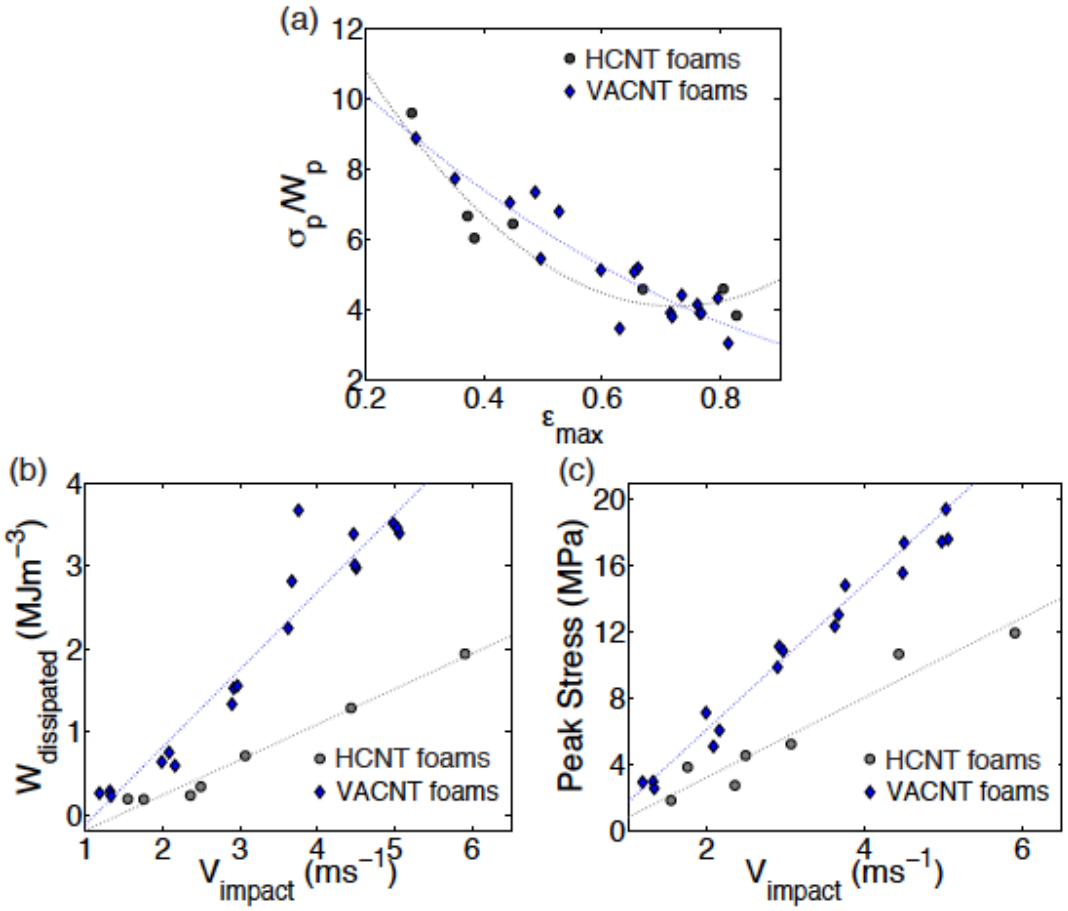


Figure 2.6: (a) Dynamic cushion factor with maximum strain reached on impact, (b) hysteretic energy dissipation with impact velocity, and (c) peak stress with impact velocity.

The specific damping capacity—i.e., the hysteretic energy dissipated normalized by the energy absorbed up to the peak stress—of all the HCNT foams tested in this study is on average ~0.56 ± 0.07. This implies that ~45% of the energy absorbed by the HCNT foams is stored elastically and released as the striker gains rebound velocity. VACNT foams with similar densities stored only 28% of the absorbed energy as elastic energy and dissipated the rest (72%) through hysteresis [40] (see also Fig. 2.6(b)). The higher elasticity of the HCNT foams is also observable from their narrower hysteresis compared to the VACNT foams. This comparison demonstrates the fundamental difference of the helically coiled microstructure of the HCNT foams as opposed to the straight CNT structure of the VACNT foams.

We characterized the fundamental deformation mechanisms during impact using *in-situ* high-speed microscopy [44]. Characteristic deformation micrographs and the corresponding dynamic stress–strain diagram of an HCNT foam impacted at 4.43 ms^{-1} are shown in Fig. 2.7. As evident from the image sequence, when the HCNT foam is impacted it undergoes an initial compression without apparent deformation localization. Then, crushing initiates in the low-density region of the sample adjacent to the substrate and progresses as the striker compresses the foam. After reaching the peak stress at maximum compression (image 4 of Fig. 2.7), the sample unloads rapidly by pushing the striker back and eventually detaches from the force sensor. This deformation mechanism in dynamic loading is significantly different from the previously described quasistatic deformation mechanisms of HCNT foams: the intrinsic density gradient governs the

progressive deformation in the dynamic state whereas, in the quasistatic compression state, the presence of nanoscale defects dominates the strain localization at arbitrary weak locations.

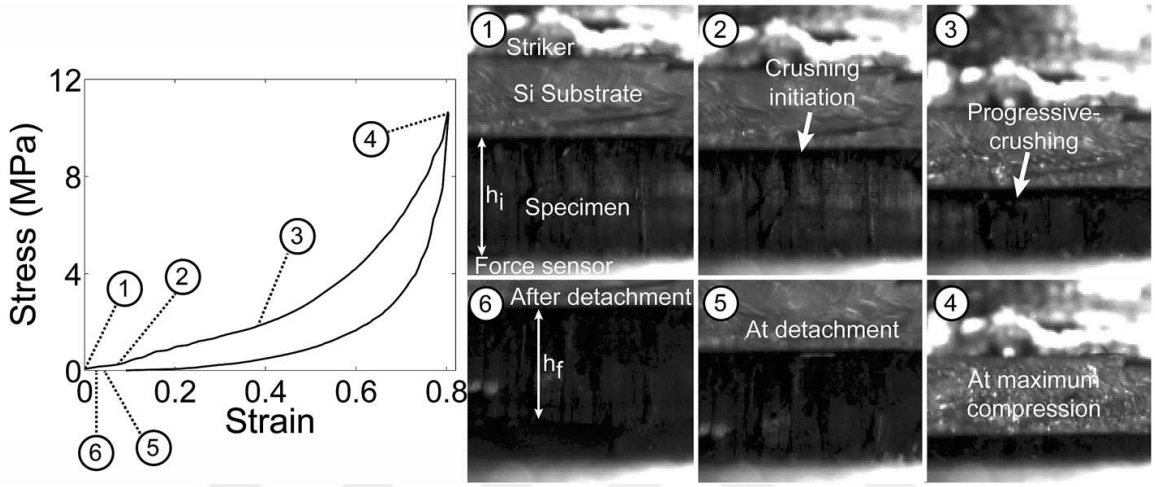


Figure 2.7: Stress–strain response and deformation micrographs of an HCNT foam impacted by a striker at 4.43 ms^{-1}. In the dynamic stress-strain diagram (left figure) the circled numbers identify snapshots (shown on the right) selected from the high-speed microscopic image sequence.

At high impact velocities, the edges of the samples underwent brittle fracture (image 5 of Fig. 2.7) and a plume of fractured debris could be seen flying off the sample on the high-speed video, when the sample detaches from the force sensor. Despite the presence of these microscale fractures, the HCNT foam shown in Fig. 2.7 recovered 90% of its bulk compressive strain upon unloading. All HCNT foams tested in impact showed a significant bulk recovery, on average 91.5 ± 6.3%.

2.5 Conclusions

We studied the mechanical response of HCNT foams subjected to quasistatic and dynamic loadings and identified their fundamental deformation responses. In the quasistatic regime, HCNT foams present strain localizations and structural buckles occurring at arbitrary, weak sections through the sample thickness. Micro-scale brittle fracture of HCNT bundles is also commonly observed, although in bulk, all samples recover most of their deformation. We supported the mechanical tests with SEM/TEM analysis and identified the microstructure contributions to the observed deformation mechanisms and the bulk recovery of the sample. In the dynamic regime, the HCNT foams follow different deformation mechanisms, characterized by the progressive crushing. We correlate this progressive crushing to the intrinsic density gradient that we quantitatively measured using synchrotron X-ray scattering and mass attenuation. We compared the response of HCNT foams to VACNT foams and identified significantly different rate-dependent micro-scale deformation mechanisms. HCNT foams exhibit better impact absorption characteristics compared to VACNT foams in the considered range of impact velocities. These observations suggest that the HCNT foams can serve as excellent candidates in developing advanced protective materials for energy dissipation and impact absorption.

CHAPTER THREE

SELF-ASSEMBLED RECYCLABLE HIERARCHICAL BUCKY AEROGELS

3.1 Introduction

Aerogels are synthetic, ultralight, and highly porous materials known for their low thermal conductivity, low bulk density, and high surface area. These unique properties have led to the use of aerogels in multifunctional applications [55–57], which include artificial muscles [55], solar cells,[56] radiation detection [58], supercapacitor electrodes [59], and catalysis [60]. Traditionally, aerogels are oxide-based (e.g., SiO_2 [61] and SnO_2 [62]), however in the recent past, scientists have developed non-traditional hierarchically nanostructured aerogels, viz., multi-walled carbon nanotubes (MWCNTs) films,[63] nanosponges [64–66], nanofoams [67], nanowire membranes [68], and organic and inorganic composites [69]. To date, these hierarchically nanostructured aerogels are either synthesized via chemical vapor deposition (CVD) [64], sol–gel or critical point drying (CPD) techniques [66], which are not only tedious but lack easy scalability, and use expensive equipment or toxic precursors [64].

In this chapter, we demonstrate the fabrication of 3D hierarchical all-carbon aerogel, which we refer to as buckyaerogel (BAG). We synthesize large BAG samples with tunable porosity and characterize their microstructure, hydrophobicity, and

oleophilicity, and mechanical properties. We show that BAG is highly oleophilic across a moderate range of surface tensions (20–40 mN m^{-1}) and displays a strong affinity toward a variety of organic and inorganic solvents. Our top-down synthesis allows for the porosity of BAG to be tuned to facilitate selective absorption of solvents up to 20 times its weight, which is comparable to the performance observed in other nanowire-based sponges and is at least 5–10 times better compared to absorptive properties of activated carbon aerogels [68]. Notably, BAG has the unique ability to absorb oil from oil-in-water (o/w) emulsions, which continues to be a formidable challenge in oil-spill cleanup efforts critically endangering our environment. The absorbed oils/solvents may be efficiently recovered by simply squeezing the BAG, or disposed via burning the BAG under ambient conditions. Lastly, the exceptional MWCNTs properties render BAG highly stable and resistant to harsh chemical exposure (including strong acids), high pressure, and high temperature environments.

3.2 Experimental Section

For preparing a BAG, ≈50 mg MWCNTs (Sai Global Technologies, Inc., San Antonio,TX, dia: 30–50 nm) were added to 1 wt% sodium dodecyl sulfate (SDS: 100 ml) aqueous solution. About 10, 20, and 50 wt% CF (avg dia 8 μm) were added to this mixture and tip sonicated (Branson Sonifier 200 Watt) for 10–15 min (at 40% power) to prepare a homogenous dispersion in the SDS solution. Subsequent to vacuum filtration through a nylon filter membrane (Whatman, 0.45mm), three different BAGs (labeled as

BAG-10, BAG-20, and BAG-50) were obtained. Following a heat treatment in air at 70 °C for 30 min, each BAG was peeled off the filter paper as a freestanding disc (inset (i) of Fig 3.1a). When the loading of CF exceeded 50 wt%, the above procedure did not yield a BAG, presumably due to the insufficent amount of MWCNTs to form a robust network in which the CFs could be held. Scanning electron microscopy characterization was performed using Hitachi S-3400N. The contact angle was determined from the optical images obtained using a tabletop Celestron 100X microscope and *ImageJ* software. For characterizing the oil absorption ability, a known mass of BAG sample was allowed to adsorb oil and then weighed later to measure the absorbed oil. The mechanical performance of the BAG structures was tested using a commercial testing system (Instron ElectroPulse E3000).

3.3 Characterization

3.3.1 SEM and N_2 Adsorption

As evident from the scanning electron microscope (SEM) images of a BAG cross-section (Fig. 3.1), vacuum filtration of CFs containing MWCNT dispersions results in a self-assembly of stacked layers of randomly entangled MWCNTs (similar to a MWCNT buckypaper) supported by interpenetrating CFs. The standard N_2 adsorption isotherms (at 77 K) revealed an average mesoporous (2– 50 nm, ≈5–7%) and macroporous (1–10 μm, ≈93–95%) size distribution, which stem from the intra-and inter-layer distribution of

MWCNT layers (Fig 3.1). As discussed later, such pore distribution allows an easier access to the BAG interior resulting in a higher absorption capacity.

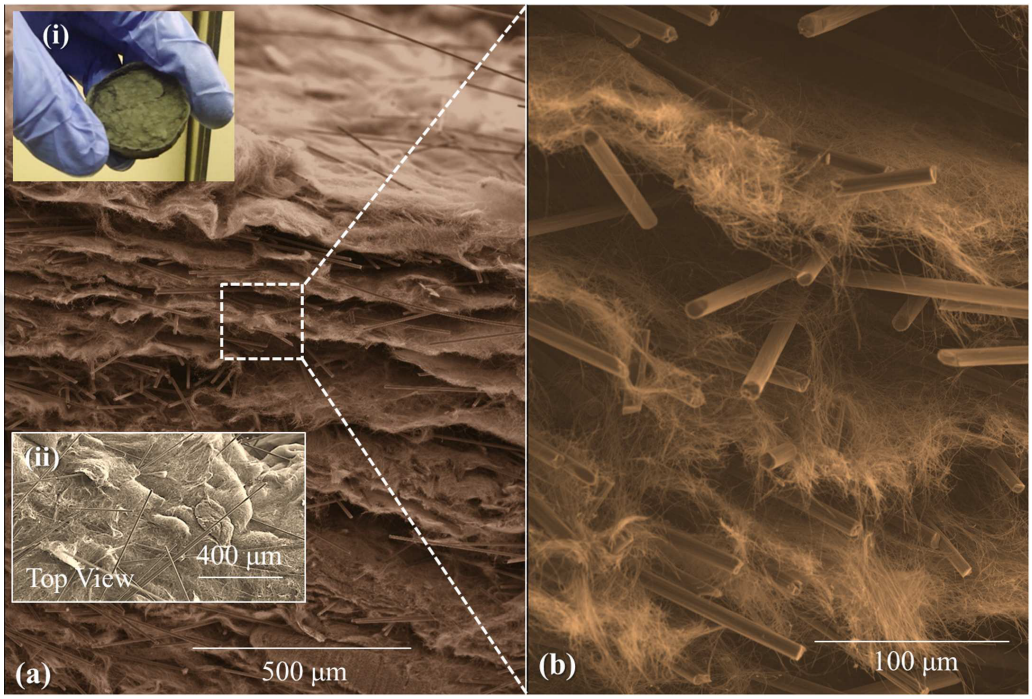


Figure 3.1: Scanning electron microscope (SEM) images of as-prepared bucky aerogels (BAGs). (a) The crosssectional view clearly shows the layered composition of the carbon nanotubes (CNTs) and carbon fibers (CFs). The inset (i) depicts the as-prepared BAG disk, which is robust and easy to handle. The inset (ii) is the SEM image of the BAG top surface, which together with the image in (a) suggests that the BAG is predominatly an entangled microstructure containing sheets of CNTs with inter penetrating CFs. (b) Magnified image of the marked area in panel (a).

The wetting angle of ≈160° by a water droplet in Fig. 3.2(a) implies that the BAGs exhibit superhydrophobicity (contact angle >150°). An obverse response

(oleophilicity) was seen for an oil drop, which wets the BAG with a contact angle of ≈35° (Fig. 3.2(b)) before getting fully absorbed by the BAG. As a result, BAG is an ideal material for separating oil from water due to its highly selective absorption capacity for oil over water.

3.3.2 Absorption characterization

To characterize BAG's absorption efficiency and gauge the influence of its meso- and macro-porosity, we undertook a study in which 10–50 wt% of diesel oil (density ≈0.85 g cm^{-3}) was separated from a mixture of oil and water (Fig. 3.2(c)). Following the immersion of a BAG in the oil–water mixture for a time *t*, the BAG was weighed after wiping the unabsorbed oil from surface with a clean razor blade. Based on the amount of absorbed oil, a quality factor *Q* = (weight after absorption of weight of as-synthesized BAG)/weight of as-synthesized BAG) x 100 for each of the three BAGs was calculated (Fig. 3.2c). The *Q* for each of the BAGs was found to increase linearly with time, indicating a constant rate of absorption, before attaining a saturation absorption at $t \approx 1$ min. Interestingly, a maximum *Q* of 1800% was recorded for BAG-50 implying that the amount of oil absorbed was 18 times the weight of the BAG. Such absorptive properties of BAGs are at least 5–10 times better than the traditional activated carbon aerogels. The enhanced *Q* for BAG-50 compared to those for BAG-10 and BAG-20 is attributed to the increased number of macropores accessible to oil in BAG-50.

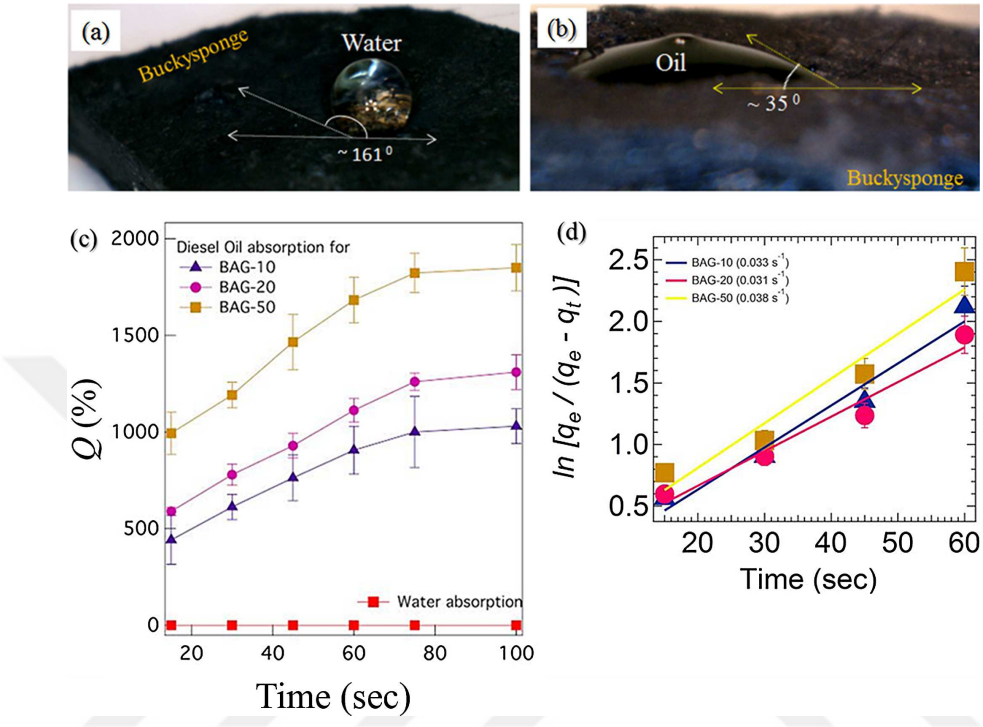


Figure 3.2: Panels (a) and (b) depicts a qualitative comparison of the hydrophobic and oleophilic properties of the BAG, respectively. A water droplet exhibits an apparent contact angle of ≈160° and remains on the surface of the BAG while an oil droplet (Fischer vacuum pump oil) gets fully absorbed by the BAG after wetting the BAG with an apparent contact angle of ≈35°. Note that the cosine of apparent contact angle (on a rough surface) is related to the cosine of the Young contact angle (on a flat surface) through the roughness ratio. (c) Dependence of the quality factor Q on time and the macroporosity of the BAG. Evidently, the BAG comprised of the highest amount of CFs exhibits the highest Q, or absorbs the maximum oil. (d) The absorption process follows a pseudo-first order rate kinematics. The solid lines show the least square fits to the

experimental data and of the corresponding rate constants (k_{p1}) for each sample are indicated within parentheses.

The increased macroporosity, as seen in Table 3.1, is likely due to an increased amount of CFs in the BAG, which in turn increases the interlayer spacing in the BAG (cf. Fig. 3.1). The increased interlayer spacing facilitates transport of a larger amount of oil through the macroporous channels. The absorption is conjectured to be a simple physical process at the macropores corroborated by the exclusively physisorption capacities, which follow pseudo-first order kinetics [70] (Fig. 3.2d) as described in Eq 3.1

$$ln\left(\frac{q_e}{q_e - q_t}\right) = k_{p1}t \qquad (3.1)$$

where q_e is the maximum saturated Q, q_t is the Q value at any given time t, and k_{p1} is the pseudo 1st order rate constant. BAG-50 samples exhibited a slightly higher rate constant (Fig 3.2(d)) compared to BAG-10 and BAG-20 suggesting that the absorption process is indeed driven through the macroporous channels. Interestingly, the physical absorption and mass transfer play a major role with no evidence for chemisorption in the kinetics, which affirms our hypothesis, and makes BAGs attractive for a wide range of applications due to its tunable macroporosity.

Sample	Micropores (dia <2 nm)	Mesopores (2 nm <dia<50nm)	Macropores (dia >50 nm)	Pore volume (cm^3/g)	BET Surface Area (m^2/g)
BAG-10	3.2%	28.8%	68%	0.072	24
BAG-20	1.6%	26.9%	71.5%	0.065	22
BAG-50	3.1%	16.9%	80%	0.060	21

Table 3.1: Pore size distribution for various BAG samples obtained from BET measurements.

Besides diesel oil, we also investigated BAG-50's capacity to absorb other organic solvents (dimethyl formamide (DMF), ethanol), saturated fats (vegetable oil), and other oils (motor oil). As indicated in Fig. 3.3(a), all solvents could be readily separated from their corresponding aqueous mixtures (10– 50wt% in water). DMF was the most absorbed liquid ($Q \approx 2000\%$) while all other liquids exhibited a Q>1200%, which is comparable to existing nanowire materials [49].

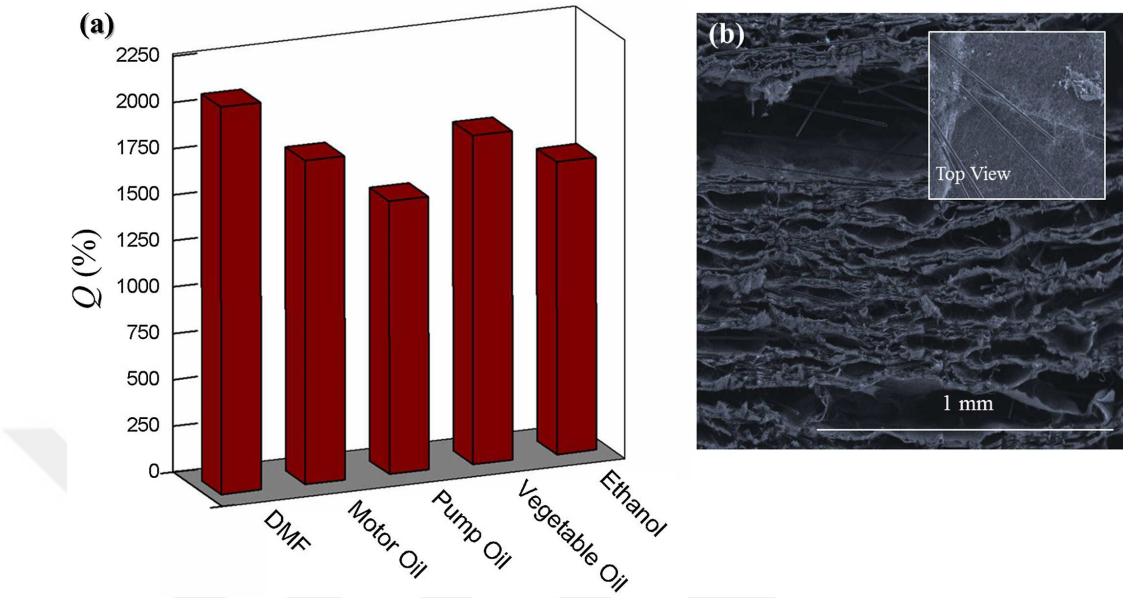


Figure 3.3: (a) The *Q* plotted for a variety of organic liquids. (b) A SEM image of the cross-section of a burnt BAG-50 with its layered architecture (cf. Fig 3.1) left intact with no noticeable deterioration in its physical and absorptive properties.

In order to retrieve the adsorbed oil, the oil saturated BAG could be either mechanically squeezed, as discussed in the later section, or ignited to burn off the oil and reused, thus facilitating energy harvesting as heat. To test this hypothesis, we allowed BAG-50 to absorb regular vacuum pump oil for 15 s and then subsequently burnt it to release 736 kJ of heat energy. We measured the released energy by heating de-ionized water and measuring the change in the temperature (ΔT) of 100 ml of water in a glass beaker using a thermocouple (Omega J thermocouple, part number CHAL-32). Assuming the heat capacity of water (c_w) to be 4186 J kg^{-1} °C, we obtained the heat energy $E=mc_w\Delta T$ to be 736 kJ, where m is the mass of water. The oil burns at about 300 °C, which is not high enough to damage the BAG's carbon constituents. Hence, even after

prolonged and repeated burning, the layered morphology, flexural, and absorption properties of the BAGs remained intact (Fig. 3.3(b)) with no measurable mass loss.

One of the bigger challenges currently faced by the petroleum industry is to separate oil from its emulsion phase. Hence, we tested the BAG's performance in separating oil and water from two oil-in-water (o/w) emulsions with 50 and 33% (by wt) oil. The emulsion was prepared by tip sonicating oil (density 820 mg ml^{-1}) with water (density 991 mg ml^{-1}). The density of the emulsion was measured to be 908 mg ml^{-1} (50% o/w emulsion) and 934 mg ml^{-1} (33% o/w emulsion). A BAG-50 was then immersed in the emulsion in a petri dish. After 5 min, the oil saturated BAG was removed, and the density of the remaining emulsion increased to 976.3 mg ml^{-1} (50% o/w emulsion) and 951.26 mg ml^{-1} (33% o/w emulsion). This dramatic increase in the final density arose from 90% removal of oil from the emulsion confirming that BAG is an effective emulsion separator.

3.3.3 Quasistatic compression test

Another unique attribute of the BAG is its ability to deform elastically under an applied external force, and revert to its original shape upon removal of the external force. This elasticity of the BAG is essential for efficient recovery of absorbed liquids. To characterize its mechanical performance, we performed strain-controlled quasistatic compression tests at 0.01 s^{-1} strain-rate. The characteristic loading–unloading stress–

strain responses of BAG-10, BAG-20, and BAG-50 samples up to 80% compression are shown in Fig 3.4(a). When a BAG sample is compressed, it exhibits a foam-like response, i.e., the stress increases nonlinearly with strain up to the peak stress, and then follows a rapid unloading along a different stress–strain path, forming a hysteresis loop. The presence of this hysteresis, similar to other foam materials [71], is responsible for the dissipation of mechanical energy.

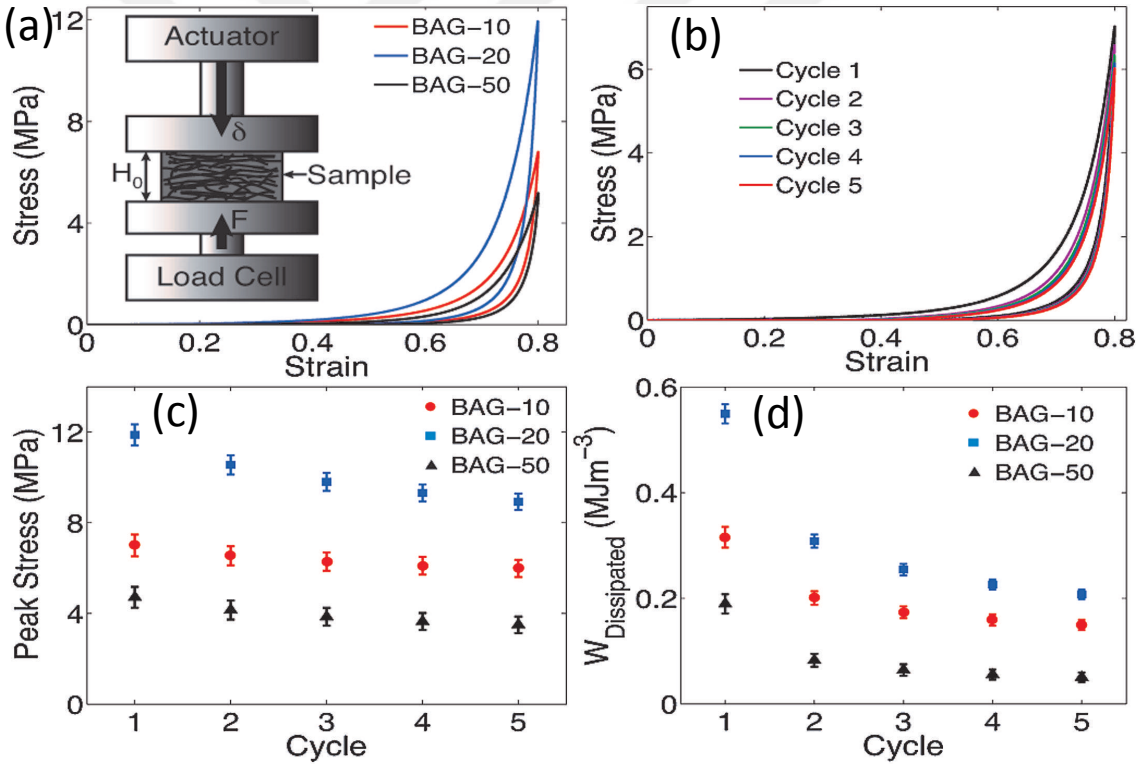


Figure 3.4: Mechanical response. (a) Characteristic stress–strain responses of BAG-10, BAG-20, BAG-50 samples; the inset shows a schematic of the test setup. (b) Cyclic compression response of a BAG-10 sample. (c) Variation of peak stress values reached in consecutive cycles. (d) Variation of the energy dissipation with consecutive cycles.

On an average, BAGs dissipate ≈500 kJ m^{-3} energy in the initial compression cycle, which is more than 50 times higher than the energy dissipated by commercial polymeric foams with comparable bulk densities [71].

BAG-20 (with 20% CFs) exhibits a stiffer response compared to BAG-10 (with 10% CFs), as expected, due to the increased presence of CFs in the former. However, BAG-50 (with 50% CFs) exhibits a more compliant response, which is a result of its relatively high porosity. To evaluate the robustness of the BAG materials, we performed quasistatic cyclic compression tests. Fig. 3.4(b) shows the characteristic response of a BAG-10 sample for five consecutive cycles. All samples exhibit preconditioning effects – the first cycles follow a different loading path than the consecutive cycles. This preconditioning effect, common in MWCNT materials [50], is more pronounced in the first three cycles, beyond which the response of the samples stabilizes to a repeatable loading–unloading path. The preconditioning is also evident in the measured peak stress and energy dissipation as a function of the number of loading cycles (Fig. 3.4(c and d)). For example, for the BAG-10, the peak stress decreases by ≈ 15% in the first three cycles, and remains nearly constant in the following cycles. The energy dissipation decreases ≈ 45% in the first three cycles and remains nearly constant in the consecutive cycles. Importantly, all samples show an average recovery of ≈ 50% in compression even after repeated cycles at 80% strain. This ability to recover large deformation is important in oil absorption applications. Since the oils/ solvents are physisorbed by the BAG, it is

possible to retrieve most of the absorbed oil/solvent by simply squeezing the saturated BAG without compromising the BAG structure. In other words, after squeezing out the physisorbed oil, the BAG reverts to its original shape and can be reused.

3.4 Conclusions

The self-assembly of an inter-connected network of MWCNTs and carbon fibers (CF) can be used to synthesize hierarchical BAG structures with controlled porosity. BAGs exhibit excellent oil/solvent absorption properties (as much as 20 times their weight) for a variety of solvents (surface tensions: 20–40 mN m^{-1}). More importantly, BAGs can efficiently separate oil not only from slicks but also from oil-in-water emulsions with ≈ 90% efficiency. More importantly, BAGs exhibit a highly nonlinear foam-like stress–strain response with hysteretic dissipation and high-strain recovery.

CHAPTER FOUR

SCALABLE, HIGH-CHARGE CAPACITY CARBON COMPOSITE ELECTRODES BASED ON RENEWABLE REDOX POLYMERS

4.1 Introduction

New materials and approaches to energy storage are being pursued in an attempt to obtain energy security and reduce greenhouse gas emission from fossil fuels [72–75]. Considerable resources are being expended on renewable energy sources, and these systems will require energy storage systems that store and deliver the energy to maintain our ability to use energy on demand. Supercapacitors and advanced battery systems (nickel, lithium, sodium-sulfur, etc.) have been identified as promising devices for supporting the emergence of renewable energy and offsetting the petroleum demands of transportation [72–76]. The push for new energy storage materials and systems is evidenced by the steady increase in federal funding in this area. As the demand for alternative energy increases, it is important to consider the availability of active storage materials. Regardless of how mature Li-ion technology becomes, the world supply of lithium may not be sufficient to meet future energy storage demands [77]. In order to push technologies towards practical use, it is important to explore new directions using compatible, widely available materials.

Electrochemical capacitors, also referred to as Supercapacitors (Fig. 4.1), function as "fast batteries" by supplying high amounts electrical energy on short time scales, with rapid switching speeds and long-term cycle stability. Supercapacitors have been proposed to bridge the gap between batteries and capacitors by incorporating elements of both technologies. High power densities are achieved due to the charge storage mechanism, which involves ion adsorption to polarized electrode interfaces.

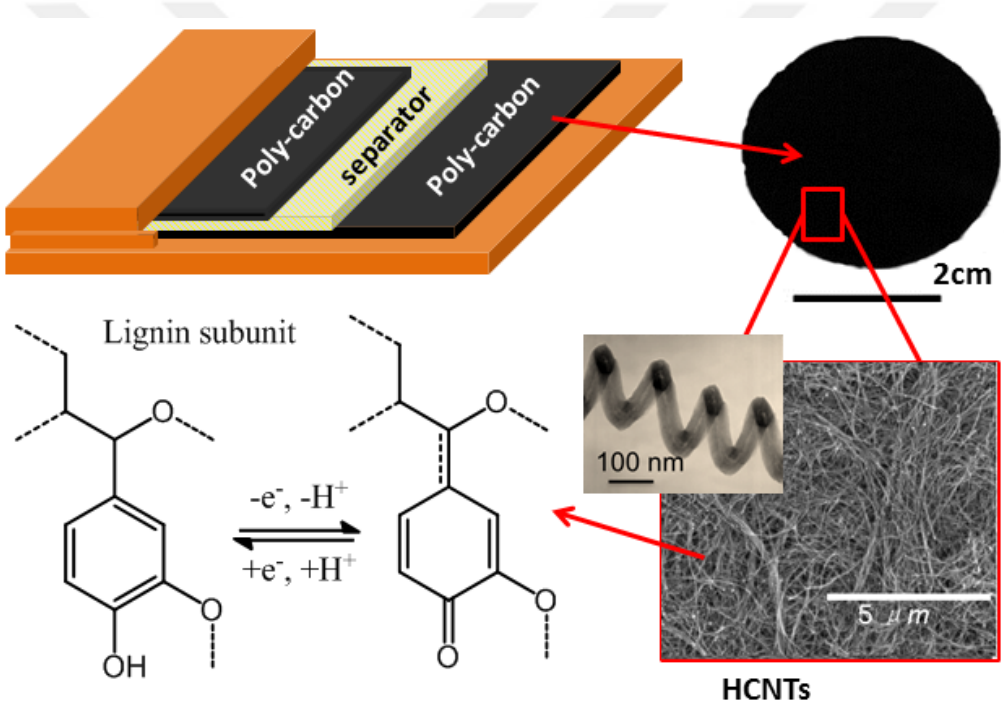


Figure 4.1: Illustrative schematic of a supercapacitor utilizing free-standing carbon "paper" electrodes fabricated with carbon nanotubes. An electrode comprising helically coiled carbon nanotubes (HCNTs) coated with sodium lignosulfate is shown along with a scanning electron micrograph. The chemical structure and redox functionality proposed in sodium lignosulfate is also shown.

Commercial electrochemical double-layer capacitors (EDLCs) use graphitic, conductive carbon electrodes with a high specific surface area. Carbon is attractive due to its chemical and thermal stability; however, the maximum attainable gravimetric capacitance is around 150-200 F g^{-1} in aqueous electrolytes due to fundamental surface area limitations [78]. Various forms of high surface area carbon materials have been evaluated extensively for supercapacitor electrodes in a wide range of electrolytes. Mesoporous carbon, with surface areas up to 2500 m^2 g^{-1}, has found application in commercial systems supercapacitors with high cycle stability and chemical compatibility in organic solvents over a voltage range of 2.5-3V. By replacing the inert carbon with redox materials, such as ruthenium oxide (RuO2) or electro-active conducting polymers (ECP), the capacitance can be increased up to 1400 F g^{-1} [79].

Research efforts focused on carbon nanotubes, graphene, graphene oxide and other carbon nanomaterials have been increasing at a high rate to understand how to maximize the energy and power density of materials comprised of carbon for EDLC devices or within composite electrodes containing various classes of redox materials. Composite electrodes comprising ECPs and various carbon allotropes have been reported extensively. These materials utilize conductive nanotube or graphene materials with high surface area, but low redox activity. Composite polymer-carbon electrodes have been prepared by chemically polymerizing ECPs in solutions with dispersed carbon nanotubes (CNTs) or by electrochemically polymerizing ECPs on surfaces coated with CNTs. Chemically synthesized materials still require additives and current collectors when

assembling the device electrode. On the other hand, electrochemically synthesized electrodes are generally limited to submicron thick films with limited overall charge capacity. The carbon "paper" electrode platform reported here avoids these restrictions by providing more than 1 mm-thick mechanically robust electrodes with the capability of easily varying nanotube density and electro-active material composition.

ECPs exhibit excellent electrochemical properties for supercapacitors; however, their poor stability, low theoretical capacity and relatively low potential range for operation limit their use in large format and light weight energy storage systems [80]. Non-conductive polymers with pendant redox groups, on the other hand, may find use in battery and supercapacitor systems because they have theoretical charge capacities as high as 496 mA hr g^{-1} (quinone-based polymers) and their redox potential can be tailored to fall within an operating voltage range of interest [81]. These materials have not found use in energy storage because they are intrinsically insulating and cost-effective, lightweight, conductive scaffolds have not yet been reported to support their utilization.

In this chapter, we demonstrate the synthesis of high-surface area, polymer-modified carbon nanotubes (or helically coiled carbon nanotube) "paper" electrodes for high-power, high-energy density supercapacitors using simple fabrication methods. The use of conductive, high surface area carbon nanomaterials allows for the utilization of low-cost, non-conductive polymers containing reversible redox groups with higher charge capacity, such as sulfonated lignin. In these composite electrodes, the carbon

nanomaterial provides high conductivity three-dimensional network structure for efficient electron transport, and the thin polymer coating provides redox active groups for increased charge capacity through Faradaic charge transfer. The simple electrode fabrication process comprising polymer and nanotube dispersion followed by filtration produces a convenient platform for large-scale device production and material characterization. Importantly, our approach allows for the use of non-conductive materials on highly porous networks for battery and supercapacitor electrodes. Materials have been previously dismissed for use in carbon-based energy storage systems may now find a role by applying this unique and robust platform and synthesis process. The ability to make electrodes with large quantities of a lignin derivative (the 2nd most abundant polymer) provides a battery / supercapacitor electrode that is both environmental friendly and extremely low-cost.

4.2 Experimental

4.2.1 Materials

All materials were purchased from Aldrich and used as received unless otherwise noted. Concentrated sulfuric was obtained from Acros Organic. MWCNTs were purchased from Cheap Tubes Inc. and HCNTs were synthesized at the Clemson Nano materials Center (CNC) at Clemson University

4.2.2 Preparation

Pristine MWCNTs or as-prepared HCNTs were suspended in 1% aqueous solution of sodium dodecyl sulfate (SDS) or 0.3% sodium lignosulfonate (SLS) (Na-Lignin or simply indicated as *L*) using a tip sonicator probe (1/8" diameter, Branson 250) for 15 min. Subsequently, the suspension was poured onto a polyamide filtration membrane (Whatman, 0.45 μm pore diameter) and filtrated using a vacuum filtration setup (Synthware Filtration Apparatus, Kemtech America). The filtered solute on the supporting filter membrane was washed with distilled water several times to remove the residual SDS, oven dried at ~60 °C for 8 hrs. The resulting film was peeled off the membrane to yield a freestanding carbon paper film, with or without polymer. Several electrodes with different thicknesses were prepared by varying the volume of the suspension and the concentration of MWCNTs. In some cases, dried carbon electrode substrates were submerged into lignin solutions (40 g/L) for various times. Next, films were removed from solution, rinsed copiously with DI water, and dried under vacuum at 80 °C overnight.

The polymer content within the HCNT (or MWCNT) composite electrode was varied using two approaches: first, HCNTs were dispersed in aqueous solutions using varying ratios of SDS, a conventional surfactant, and SLS, the redox polymer surfactant. Electrodes were formed by filtering solutions of HCNTs dispersed with pure SDS

(HCNT), 10% SLS (HCNT-5), 25% SLS (HCNT-8), and pure SLS (HCNT-30). These films were soaked in SLS solutions for 24 hr, then rinsed with DI and dried in vacuum.

4.2.3 Structural Analysis

Thermal gravimetric analysis (TGA) was performed on 1-2 mg samples in an alumina crucible over a temperature range of 25 °C to 800 °C at a rate of 40 °C /min (TA Instruments, Q600 SDT). Scanning and transmission electron microscopy (SEM and TEM) were performed using a Hitachi S4800 field-emission electron microscope and a Hitachi H7600 microscope.

4.2.4 Electrochemical Analysis.

Electrochemical properties were measured in 1 M perchloric acid or 0.5-1.5 M sulfuric acid aqueous solutions (Princeton Applied Research VersaSTAT 4) using the polymer-modified carbon as the working electrode, an Ag/AgCl reference electrode and a Pt mesh counter electrode. Carbon-polymer electrodes were adhered in a Teflon cell with an exposed area of 0.5 cm^2 and contacted with Ti foil. Films were characterized using cyclic voltammetry (υ = 1-0.003 V/s) over a potential range of -0.5 to 1.2 V, Galvanostatic cycling (i = 30-0.2 mA) between -0.2 and 1.2 V, and electrical impedance spectroscopy over a frequency range of 10 kHz to 0.1 Hz (20 mV amplitude). 2-electrode asymmetric supercapacitor testing was carried out in a coin cell apparatus (MTI Corp). In

this set up, activated carbon (2.5 mg, 0.5 cm^2) is designated as the anode and the HCNT-lignin paper as the cathode. Electrodes separated by a glass microfiber separator (whatman). The cell performance was evaluated using CV, EIS and galvanostatic charge discharge measurements over a cell voltage range of 0 to 1.5 V.

4.3 Results and Discussion

Two primary charge storage mechanisms can occur in redox polymers, and each mechanism has an important impact on the electrode properties. Charges in electroactive conducting polymers (ECPs) are delocalized across large segments of the polymer resulting in a range of energy states, and therefore, potentials over which redox processes can occur. In general, higher energy densities can be achieved in redox polymers where charge is localized to a given group (e.g., quinone) and higher power densities are obtained in electrodes comprised of ECPs due to their electron conductivity. In non-conductive polymers with pendant groups containing reversible redox couples, such as ferrocene or quinones, charges are localized to a given group, which limits their conductivity, and they're considered for energy storage. Adding redox polymers with high charge capacity can increase the energy density of polymer electrodes. Since quinone has a greater capacity (~500 mA hr g^{-1}) compared to pyrrole (~100 mA hr g^{-1}), a significant increase in performance may be achieved [81]. With the low cost associated with polymers materials and processing, in addition to the widespread availability of biopolymers from green sources, such as lignin, the opportunity for *extremely* low-cost

energy storage becomes obvious. Previously, Inganas *et al.* showed that lignin can be incorporated into conducting polymer electrodes using electrochemical polymerization [82]. While they achieved relatively high charge capacities within all-polymer electrodes, their method is only amenable to the synthesis of low quantity materials (thin films), whereas films with thickness greater than 2 μm begin to exhibit significant performance (transport) limitations. Lignin, a renewable biopolymer from plants and trees, is not electrically conductive, therefore pure lignin electrodes show negligible electrochemical activity, which is limited to the redox groups at the electrode interface.

Here, robust, carbon nanotube paper-like electrodes are prepared using simple dispersion and filtration methods, which have been previously reported as electronic materials. Briefly, multiwall carbon nanotubes (MWCNTs) or helically coiled carbon nanotubes (HCNTs), are dispersed in aqueous solutions using a surfactant, sodium dodecyl sulfate (SDS). After ultrasonicating the solution for 15 min to disperse the aggregated nanomaterials, the aqueous dispersion are vacuum-filtered through a polyamide membrane, copiously rinsed with deionized water and dried at 60 °C for 8 hr. Freestanding paper electrodes are obtained by peeling the MWCNT or HCNT films from the polyamide membrane. A schematic of the fabrication process is shown in Fig. 4.2. Conveniently, the freestanding paper electrodes are very robust and durable; they can be burned under a flame, soaked in acids, bases, and organic solvents and still handled with ease. Redox polymers are incorporated within the carbon nanotube paper using two methods. In one case, the sodium lignosulfate is used as a surfactant (in addition to or in

place of SDS) to disperse the carbon nanotubes during sonication. In the second case, the CNT paper electrodes are simply soaked in an aqueous SLS solution for a designated time, then copiously rinsed with water and dried.

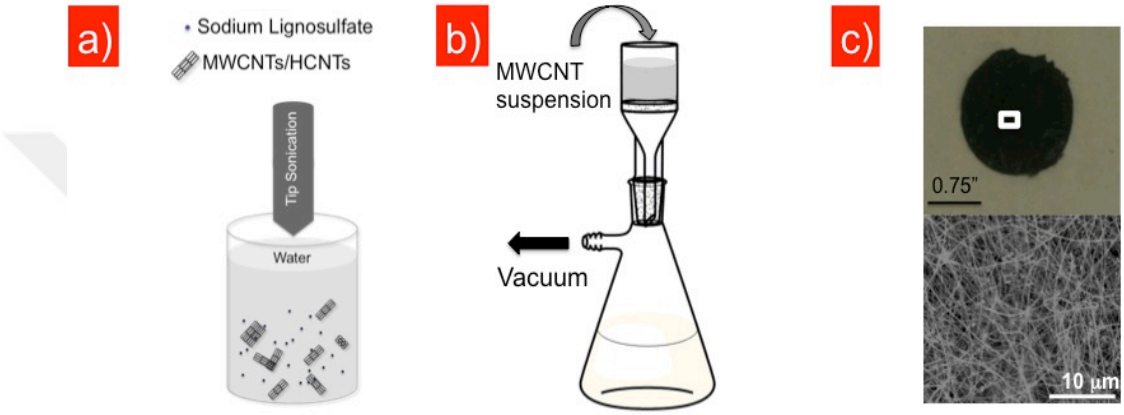


Figure 4.2: Schematic of fabrication process for sodium lignosulfonate-modified buckypaper (BP) electrodes. Carbon nanotubes are dispersed in aqueous solutions with SDS or sodium lignosulfonate (SLS), sonicated at high power, and filtered to produce freestanding BP electrodes. BP electrodes are then soaked in aqueous solutions containing 40 g/L SLS, rinsed with deionized (DI) water, and dried in vacuum.

The polymer content and structure of the composite electrode were investigated using thermal gravimetric analysis (TGA), due to the highly contrasting thermal stability between the polymer and the carbon nanomaterial, and electron microscopy to capture the surface morphology and structure. Pure MWCNT and HCNT paper electrodes are prepared by dispersing the carbon nanomaterial (0.3 mg/mL) in 10 mg/mL SDS. After filtering the dispersions to generate the paper-like electrode, the surfactant is washed

away by rinsing copiously with DI water and methanol. The thermal gravimetric profiles for the pure, vacuum-dried HCNT papers are shown in Fig 4.3(d). Each scan displays a slight decrease in mass around 150 °C from the loss of residual SDS. Under dry air, the MWNT paper decomposes at 600 °C and the HCNT paper decomposes around 570 °C. The lower density and aggregation in the helically coiled carbon nanotubes leads to a slightly lower decomposition temperature compared to the papers containing more aggregated MWNTs.

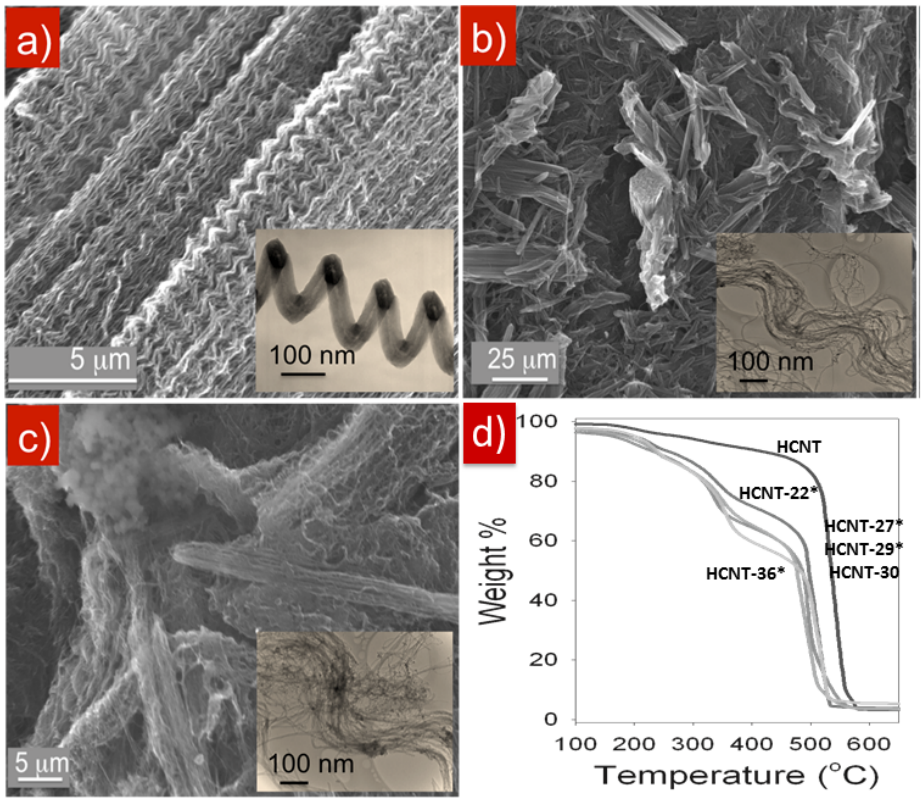


Figure 4.3: Physical properties of paper-like electrodes comprising HCNT and SLS. SEM image of: HCNT electrodes fabricated using SDS as the surfactant (a); HCNT electrodes fabricated using SLS as the surfactant (b); and HCNT electrodes fabricated with SDS surfactant followed by soaking in SLS for 24 hr (c). TEM images of each respective films is shown in the inset. (d) Thermal gravimetric analysis (TGA) of composition polymer-nanotube electrodes containing HCNT with varying amounts of lignin: pure HCNT (HCNT), electrodes soaked in SLS for 24 hr (HCNT-22), HCNT papers prepared using SLS as the surfactant (HCNT-30), and these electrodes soaked in SLS for 24 hr (HCNT-36). Also shown are two other HCNT-based electrodes that were soaked in SLS for 24 hr: one prepared using a surfactant ratio of 90/10 SDS/SLS (HCNT-27) and the other with a surfactant ratio of 75/25 SDS/SLS (HCNT-29).

Carbon papers comprising MWCNTs and HCNTs were also prepared using redox polymers as the surfactant for dispersing the CNTs. Sodium lignosulfonate (SLS), which is shown in Fig. 4.4, contains aromatic rings to promote binding to the MWNTs and HCNTs, sulfonated groups for aqueous solubility and reversible redox groups to provide Faradaic capacitance.

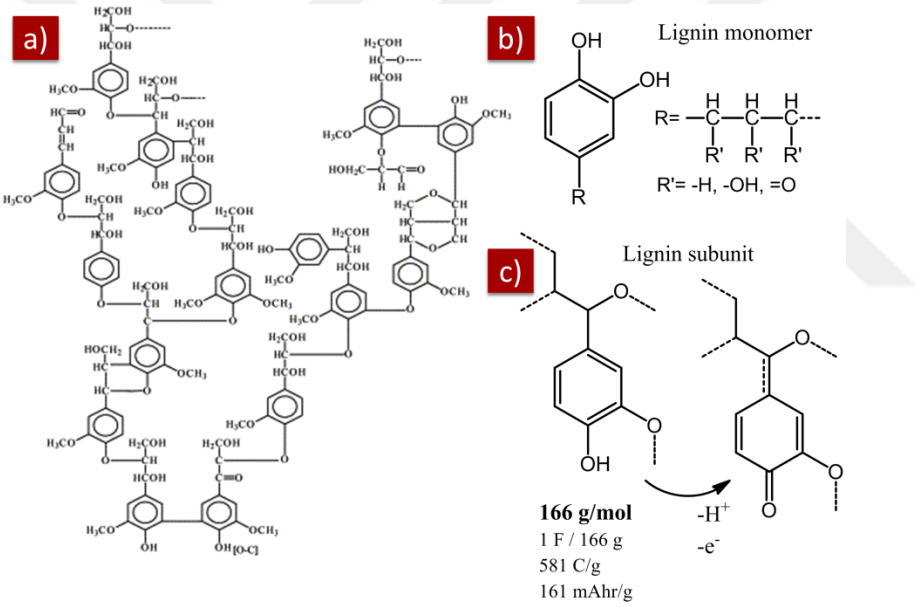


Figure 4.4: Chemical structure of lignin and representation of the oxidation-reduction processes that can occur within the phenolic groups. Oxygen rich forms of lignin can have charge capacities as high as 160-170 mA hr g^{-1}.

Dispersions were prepared with 0.3 mg/mL MWCNTs (or HCNTs) in 3 mg/mL SLS in DI water and filtered to achieve polymer modified paper electrodes. Thermo gravimetric

profiles show that that paper electrodes prepared using SLS as the surfactant retain 13 wt % polymer in the MWCNT electrodes (MWCNT-100L) and 25 wt % polymer in the HCNT electrodes (HCNT-100L). The curvature and higher surface area of the multi-wall coiled nanotubes leads to a significant increase in polymer mass adsorbed relative to the multiwalled nanotubes. The amount of SLS adsorbed to the HCNT could be tailored by varying the ratio of SLS to SDS as the surfactant (total 0.3 mg/mL). As the ratio of SLS in the surface solution increased from 10 to 100 %, the portion of SLS in the sample increased from 5 to 30 wt-%. The amount of polymer adsorbed to the carbon can be increased by soaking the electrodes in 40 mg/mL sodium lignosulfonate (SLS) solution after electrode preparation. As shown by TGA, HCNT electrodes prepared with the pure SDS surfactant adsorbed the least amount of SLS (20 wt%) upon soaking, presumably due to the HCNT aggregates in the paper electrode observed when only using SDS as the surfactant. Electrodes prepared from solutions dispersed with even a small amount of SLS showed a significant increase in polymer adsorption (30 wt%), which can be attributed to the improved dispersion and separation of HCNTs in the as-prepared electrodes. HCNT electrodes were shown to absorb up to 38-39 wt% SLS, which can be tailored by varying soak time (Fig. 4.3(d)). The influence of polymer composition on the electrochemical performance is described below. Corresponding data for MWCNT elcetrodes shows a maximum of 18-19 wt % SLS adsorbed in these electrodes. The preparation conditions for synthesizing SLS-coated HCNT and MWCNT electrodes, along with the equivalent sample design captions and mass composition, are presented in Table 4.1.

Electrode	Carbon Source	Surfactant SDS / SLS		Soak Duration (hr)
HCNT	HCNT	100%	0%	None
HCNT-24h	HCNT	100%	0%	24
HCNT-100L	HCNT	0%	100%	None
HCNT-100L-24h	HCNT	0%	100%	24
HCNT-10L-24h	HCNT	90%	10%	24
HCNT-25L-24h	HCNT	75%	25%	24

Electrode	Carbon Source	Surfactant SDS / SLS		Soak Duration (hour)
MWCNT	MWCNT	100%	0%	None
MWCNT-100L	MWCNT	0%	100%	None
MWCNT-1h	MWCNT	100%	0%	1
MWCNT-24h	MWCNT	100%	0%	24

Table 4.1: Sample descriptions for MWCNT and HCNT composite paper electrodes with and without adsorbed sodium lignosulfate (SLS).

The microstructures of the carbon electrodes were examined using scanning electron microscopy (SEM) and transmission electron microscopy (TEM). HCNT paper electrodes prepared using the standard SDS surfactant is shown in Fig. 4.3(a). The low conductivity of the redox polymer causes blurriness in the image; however, the individual nanocoils can still be identified. Although the surface area of the three-dimension network of nanocoils is expected to be high, close packing of nanocoils in aggregates will limit the electrochemical performance. When paper electrodes are fabricated using SLS polymer surfactant (HCNT-100L), shown in Figure 4.3(b), the nanocoils experience a significant decrease in aggregation and maintain spacing between individual tubes. The physical structure is ideal for efficient ion transport and adsorption during the electrochemical processes. SEM images show a more homogenous structure when the

HCNTs are dispersed in SLS compared to those prepared using SDS as the surfactant. As mentioned above, polymer composites can also be prepared by soaking the electrodes in SLS for 24 hrs after fabrication (HCNT-24h). SEM images show a similar structure compared to the as-prepared substrates (HCNT), except for the addition of adsorbed polymer (Fig. 4.3(c)).

Transmission electron micrographs are shown for each material as insets in Fig. 4.3. The bare HCNT electrodes show sharp edges along the nanocoils. When polymer is incorporated, the nanotube edges are blurred due to the presence of the non-conductive polymer. Polymer aggregates are also visible along the surface of the coiled-nanotubes.

Electrochemical analysis was performed on the freestanding lignin-modified carbon electrodes without incorporating any additional components, such as binder or conductive material. In fact, each component of our system displays characteristics of these typical additives: the high surface area carbon is also highly conductive and the redox polymer acts like a glue to hold the nanotubes in place. Single electrode half-cell measurements are conducted by placing the carbon papers in a Teflon cell with 0.5 cm^2 area exposed to an acid electrolyte. Prior to electrochemical analysis, electrodes were conditioned by cycling the electrode potential between -0.2 and 1.2 at a scan rate of 50 mV/s. With each cycle, the redox peak associated with the lignosulfonate increases as the redox active group migrates toward the nanotube, and after 5-10 cycles, a stable

voltammogram is achieved. The electrode is characterized using cyclic voltammetry, electrical impedance spectroscopy and galvanostatic cycling.

Cyclic voltammograms were recorded in 1M perchloric acid using potential scan rates (ν) between 3 and 1000 mV/s to evaluate the redox processes and ion-transport properties. The gravimetric capacitance is reported by normalizing the measured current by scan rate and mass, which was measured with a microbalance (~2-3 mg for 0.5 cm^2 electrodes). The electrochemical properties of electrodes prepared using MWCNTs dispersed with SDS are shown in Fig. 4.5(a)**.** As expected, a rectangular voltammogram is observed due to the charge storage mechanism associated with EDL capacitance, which is independent of electrode mass for electrodes measured at 30 mV/s (reported as mass per 0.5 cm^2 substrate). An average capacitance of 50 F g^{-1} is obtained for the MWCNT papers, which is expected due to the surface area of ~60-100 m^2 g^{-1}. When the MWCNT electrodes are coated with 15 wt % lignosulfonate, a significant increase in performance is obtained. The redox peak is observed near 0.55 V corresponds to the redox potential of the quinone/phenol groups within the sulfonated lignin. A peak gravimetric capacitance of 250 F g^{-1} is measured with an average capacitance of 150 F g^{-1} in the range of 0 to 1 V.

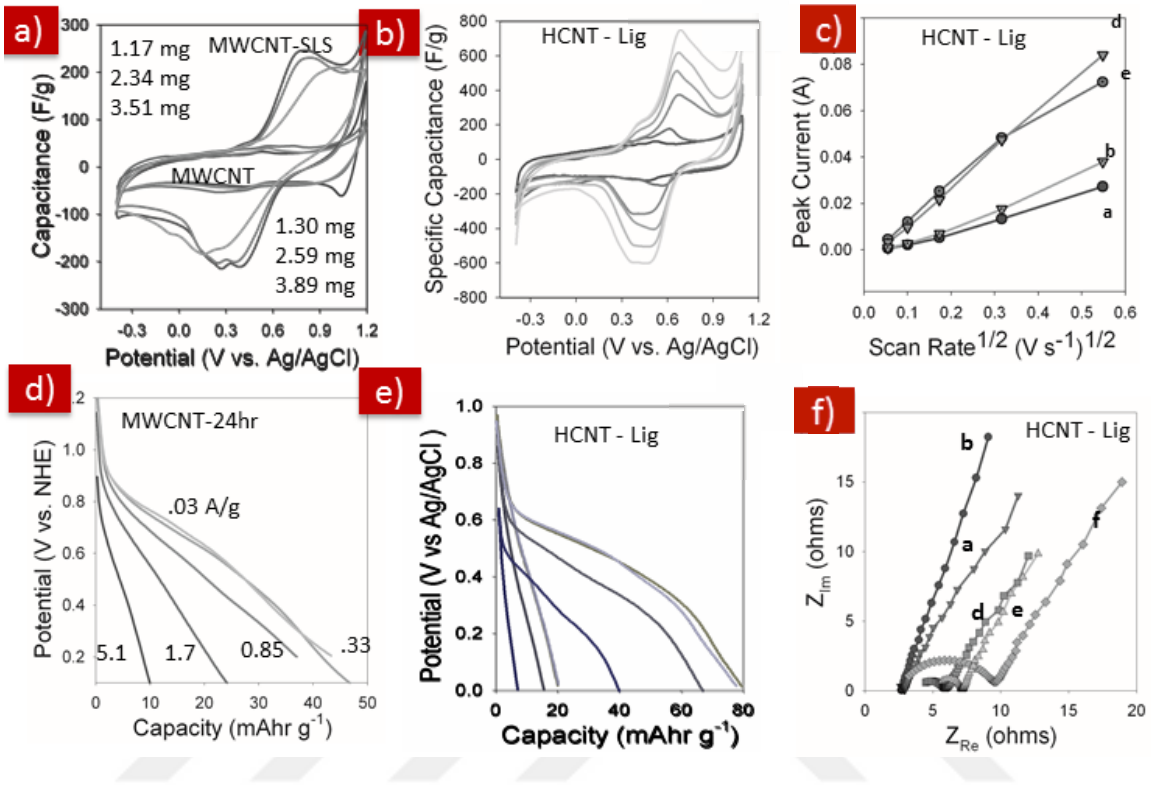


Figure 4.5: Electrochemical properties of paper-like electrodes comprising sodium lignosulfate (SLS) and either MWNTs and HCNTs obtained from single electrode configurations. (a) Capacitance vs. voltage profiles for MWNT with and without 18 wt% SLS. (b) Capacitance vs. voltage for HCNT electrodes with increasing SLS wt % (0-36 wt %). (c) Peak current vs square root scan rate for select electrodes from panel b. (d) Galvanostatic discharge curves for MWNT electrodes soaked in SLS 24 hr (MWCNT-15) at varying discharge rates. (e) Galvanostatic discharge curves for HCNT and HCNT-29 electrodes at varying discharge rates. (f) Nyquist plots for HCNT electrodes with varying SLS content. The mass of HNCTs used in each film is ~2-3 mg in an area of 0.5 cm^2.

MWCNT paper electrodes provide a high surface area and conductive scaffold for integrating non-conductive redox polymers; however, the nature of the multiwall tubes imposes a few key limitations on electrode performance. First, the multiwall structure leads to higher carbon nanotube weight content in the composite material than necessary to achieve a suitable conductivity. The nanotubes within the multi-walled structures may not contribute significantly to the EDLC properties due to the internal spacing. Additionally, the multiwall nanotubes investigated in this study typically exhibit lower aspect ratios and contain additional amorphous material, which may limit the surface area for polymer adsorption. For this reason, carbon electrodes were also synthesized using high aspect ratio helically-coiled carbon nanotubes (HCNTs) [3]. The helically-coiled carbon nanotubes (HCNTs) contain numerous defects providing a higher surface area for polymer adsorption compared to straight tubes.

The electrochemical properties of the HCNT electrodes were investigated in a similar manner to the MWCNTs. Fig. 4.5(b) shows cyclic voltammograms normalized by scan rate and mass (F/g) of HCNT papers prepared using SDS as the surfactant, along with electrodes containing increasing amounts of SLS. Pure HCNT electrodes could be cycled with scan rates up to 1000 mV/s without a significant reduction in capacitance. An average gravimetric capacitance of 80 F g^{-1} was observed for the lowest scan rate, ν = 30 mV /s, which is nearly double that of MWCNT electrodes, presumably due to the higher surface area. When the HCNT composite electrodes were prepared with SLS

(either as the surfactant, or post synthesis adsorption), a significant increase in capacitance was observed due to the additional up to 39 wt % polymer. Fig. 4.5(b) shows the specific capacitance of HCNT paper electrodes with varying lignosulfonate (SLS) composition over the voltage range of interest. The composite electrode (HCNT-29) with the best electrochemical performance displayed a peak capacitance as high at 800 F g^{-1} with an average capacitance near 400 F g^{-1} in the range of 0 to 1V. These capacitance values are significant because these are measured on electrodes with a significant mass, average 2.3-2.5 mg HCNT with up to 1.0 mg polymer (per 0.5 cm^2) compared to sub microgram quantities typically reported.

With polymer peak capacitance approaching 800 F g^{-1} at a scan rate of 3 mV/s. The addition of lignosulfate to the HCNT electrodes resulting in a significant increase in capacitance through Faradaic charge transfer in the phenolic/quinone groups; however, the presence of the resistive layer limits the use of very fast scan rates. Further increases in lignin content above 30 weight % begins to inhibit the redox properties due to the resistive nature of the polymer and large distance between the carbon nanotubes and the exterior redox groups, which cannot be electrochemically addressed.

It should be noted that electrodes prepared from HCNTs dispersed in 25% SLS/75% SDS (b) showed a greater than 4x increase in capacitance after soaking in SLS solutions after electrode fabrication. These films gave the highest electrochemical performance of all the composites tested, and was verified through multiple independent

tests. The increase in performance is attributed to the combination of surfactant materials, where the SDS initially helps disperse the NCs in solution. The SLS does not completely cover the HCNTs; therefore, additional polymer can be adsorbed after the paper electrode is formed. Similar properties are observed for electrodes prepared from dispersions containing 10% SLS and 25% SLS, which indicates that a small amount of polymer in the dispersion solution helps prevent the NCs from aggregating during the filtration process.

As shown for the MWNT composite electrodes, HCNT-polymer composites also exhibit diffusion-controlled redox properties, as evidenced by the linear relationship between peak current and square root of scan rate (Fig. 4.5(c)). Redox peaks were not observed above a scan rate of 100 mV/s, which was therefore used as the upper rate limit. Because the redox group in the polymer must migrate to and from the electrode upon oxidation and reduction, it is expected that all composites containing carbon nanomaterials and non-conductive redox polymers exhibit similar characteristics. In order to be utilized for Faradaic energy storage, the redox groups within the polymer must be in contact, or close vicinity to the nanotubes in the electrode, leading to a more significant time-dependence than pure carbon nanomaterials.

Electrode charge capacities as a function of discharge rate (in terms of A g^{-1}) were measured using galvanostatic cycling with varying discharge currents. Electrodes were cycled between potentials of 0 to 1.2 V vs. NHE with rates of 0.03 to 5.1 A g^{-1}. Fig. 4.5d

shows the discharge characteristics of MWCNT papers coated with 18 wt% polymer. A linear decrease in potential is observed from 1.2 to 0.8 V, followed by a potential plateau in the region of 0.6-0.8 V, associated with the redox potential of the lignosulfonate, followed by a linear decrease in potential from 0.6V to 0V. These features starkly contrast that of a purely carbon based electrochemical capacitor that exhibits a linear decrease in potential as ion desorb from the electrode surfaces. The presence of the voltage plateau confirms that a localized redox process occurs on the electrode surface. Lignin-modified MWCNT electrodes display charge capacities as high as 50 mA hr g^{-1}, which is notable for fully-assembled electrodes comprising purely organic materials.

Galvanostatic cycling measurements were used to determine the charge capacity of the composite electrodes and the results are shown for pure HCNTs and SLS-modified HCNT paper electrodes in Fig. 4.5(e). Pure HCNT electrodes show a charge capacity of 20 mAhr g^{-1}, which can be expected from the nanomaterial surface area. The highest charge capacity was obtained using HCNT-29 electrodes, which showed values of 80 mA hr g^{-1} for discharge rates below than 1 A g^{-1}. Increasing discharge rates result in an expected decrease in capacity. These values are significant because they represent fully assembled carbon electrode capacities; that is, no additional material is needed for a binder or current collector. The masses of HCNT electrodes investigated are on the order of mg quantities; however, we expect that the mass could be increased by simply fabricating thicker electrodes without significantly influencing the electrode performance, as shown for the MWNT electrodes.

Nyquist plots shown in Fig. 4.5(f) confirm the diffusion-controlled behavior at lower frequencies (long time scales) as evidenced by the 45° Warburg diffusion character. Furthermore, the impedance measurements show an increase in charge transfer resistance at high frequency when lignin is added to the electrode, and a significant increase in resistance when excess polymer coats to HCNTs Fig. 4.5(f). This is consistent with the decrease in gravimetric capacitance reported when HCNT-100L electrodes were coated with additional SLS.

4.4 Conclusion

The polymer modified carbon nanomaterial electrodes exemplify ideal structures for electrical energy storage electrodes. The high surface area of the carbon nanotubes provides a mechanism for energy storage through the electrical double layer capacitance (EDLC) and also promotes efficient binding of redox polymers. Electrodes without redox polymers exhibited purely EDLC energy storage which limits their charge capacity and energy density. Here, we showed that polymer modified HCNTs or MWCNTs demonstrates a clear example of how two disparate materials can be combined to exploit material properties. HCNTs provide the high surface area and electrical conductivity for high power density while the polymer provides the redox groups for Faradaic charge transfer for increased energy density. Furthermore, the three-dimensional nature of the porous network allows for the polymer to expand and contract upon oxidation in addition

to providing electrolyte saturation for fast ion transport. Compared to pure carbon nanomaterial (HCNT) electrodes that exhibit specific capacitance values and charge capacities of 80 F g^{-1} and 20 mA hr g^{-1}, respectively, electrodes containing lignosulfonate-modified HCNT electrodes exhibit capacitance values and charge capacities of over 400 F g^{-1} and 80 mA hr g^{-1}, respectively. As the cost of carbon nanotubes continues to decrease, such systems may find immediate use in low-cost energy storage devices. Importantly, the electrode fabrication process is scalable and can be applied to large format systems. The use of highly conductive, three dimensional scaffolds achieved by the carbon nanomaterials within the paper electrode provides new possibilities for low cost energy storage materials, such as solution processable redox polymers.

CHAPTER FIVE

ROLL-TO-ROLL PRODUCTION OF SPRAY COATED N-DOPED CARBON NANOTUBE ELECTRODES FOR SUPERCAPACITORS

5.1 Introduction

As the growth of portable electrical equipment, electronics, and hybrid electric vehicles continues to accelerate, there is a demand for efficient energy storage devices with high energy and high-power densities [83]. Even the most prominent energy systems, such as batteries which can exhibit energy densities as high as 400 mW h/cm^3, are limited by their slow power delivery (< 0.1 W/cm^3) [84]. Alternatively, electrochemical double layer capacitors (EDLCs) or supercapacitors can provide high power densities (~10–100W/cm^3) with an extremely long cycle life (> 10^5 cycle); however, their energy densities are significantly lower than batteries. In EDLC devices, the electrolyte ions are stored on the electrode surface without any chemical reactions allowing a fast charge or discharge. Accordingly, the capacitance of such devices (and in turn their energy density) is mostly dependent on the specific surface area of the electrode. Hence, in the recent years, there has been a concerted effort to increase the energy density of EDLCs through three approaches: (i) the addition of pseudo-capacitance materials where redox materials are added to the EDLC electrodes, (ii) increasing the specific surface area of the electrode by nanosizing, and (iii) preparation of

a hybrid electrode based on (i) and (ii). Among the multitude of emerging low-dimensional materials, carbon nanomaterials are considered as one of the ideal electrode materials due to their high electrical conductivity, chemical stability in different solutions (from strongly acidic to basic), and thermal robustness. In particular, EDLC devices with specific capacitances as high as 180 F/g have been realized using carbon nanotubes (CNTs) [85,86]. Although these values are an order of magnitude higher than traditional activated carbons, two main challenges still persist in realizing EDLC devices with a higher specific energy while retaining the ability to rapidly charge and discharge over multiple thousands of cycles for practical applications: (i) the net capacitance (C_{tot}) of the CNT electrodes is smaller than the predicted values (based on surface area) due to the presence of a series quantum capacitance (C_Q) [87,88] and (ii) the lack of facile scalable manufacturing methods and high production costs that limit the widespread use of CNT electrodes [89]. Although some potentially scalable methods such as chemical vapor deposition (CVD) [14,90,91], vacuum filtration [92], ink-jet printing [93], dip-coating [94], spray coating, or air-brushing [95] have been reported for producing nanostructured bulk electrodes, they suffer from poor CNT uniformity, delamination issues, and a high contact resistance between CNTs and current collectors.

Here, we address the two imminent challenges described above through a scalable roll-to-roll (R2R) technique for producing N-doped CNT (NCNT) electrodes with higher C_Q and higher energy and power density. Particularly, we show that N-dopants in the CNT structure introduce extra density of states (DOS) at the Fermi level allowing an

increase in C_Q and hence the net specific capacitance beyond the limits of pristine CNTs (PCNT). We developed a facile spray coating techniques, that is, amenable for R2R production of randomly aligned networks of pristine and N-doped CNTs at rates as high as ~4 cm^2/s. More importantly, we show that symmetric supercapacitor cells (coin and jelly roll type devices) consisting spray coated N-doped CNT electrodes exhibit energy density (~1 mW h/cm^3) comparable to Li-thin film batteries [6] with a relatively high power density (~0.7 W/cm^3) and > 1000 rapid charge/discharge cycles.

5.2 Experimental:

5.2.1 Electrode preparation

Two different types of pristine multi-walled CNTs (labeled PCNT1 with 15 nm diameter and PCNT2 with 70 nm diameter) and NCNTs (2% nitrogen substituted; 30 nm diameter) were acquired from Sai Global Technologies, Inc. Porous aluminum foils with varying thicknesses of 20, 30, 40, and 50 μm (labeled as CD20, CD30, CD40, and CD50) and an average pore size 1 μm were kindly provided by Cornell Dubilier (CD), Liberty, SC. All other chemicals are purchased from Alfa Aesar. For spray coating, CNTs were dispersed in isopropanol (1 mg/ml) using a tip sonicator (1/8 in. tip diameter, Branson 250W) for 30min. Subsequently, as shown in Fig. 5.1(a), CNT suspensions were spray coated on to CD aluminum foils using a paint gun (Iwata 5095 WS400) with 1.3mm nozzle and 29 psi ambient air pressure. From scanning electron microscope (SEM)

images of the cross-section of spray-coated electrodes (see inset in Fig. 5.1(a)), the thickness of CNT layer was found to be ~4 μm with an areal density of ~0.16 mg/cm^2. The porous structure of our Al foils allows the entrapment of CNTs resulting in a moderately strong adhesion even in the absence of a binder (Figs. 5.1(b) and 1(c)). Such an entrapment-assisted adhesion allows our CNT electrodes to be easily rolled into jellyroll structures for producing supercapacitor devices, without any micro-cracks that could disrupt electrode conductivity (Figs. 5.1(c) and 5.1(d)).

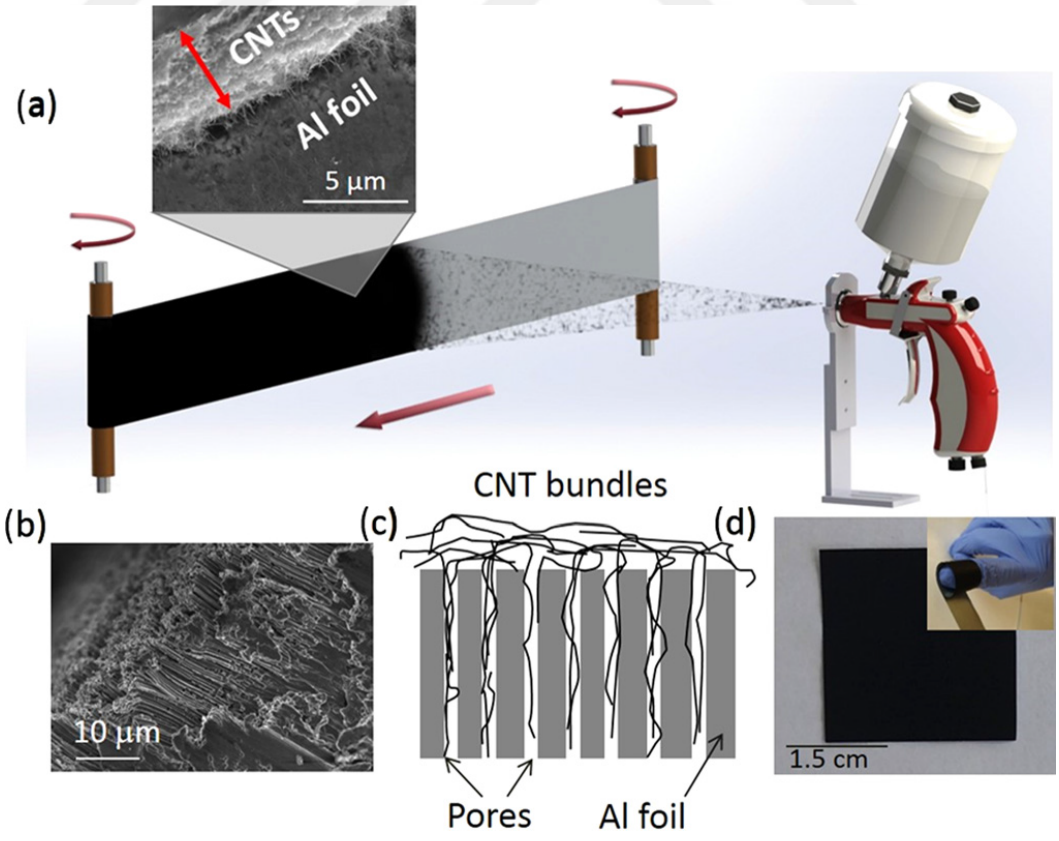


Figure 5.1: (a) A schematic of the spray coating set up for roll-to-roll production of carbon nanotube (CNT) coated Al electrodes (inset: scanning electron microscope image of spray coated CNTs on Al foil). (b) Scanning electron microscope cross-sectional image of CD20 Al foil showing the Al channels/ pores. (c) Upon spraying, CNT bundles are adsorbed into the Al foils and adhere well without the need of a binder. The electrolyte ions can access the high surface area of entangled bundles on the surface to exhibit an increased electrical double layer capacitance. (d) A photograph of an Al electrode after CNT spray coating. The inset shows that the electrodes can be easily rolled without creating any disruption in CNT conduction network.

5.2.2 Electrochemical characterization

We measured the electrochemical properties of spray coated CNT electrodes in a three-electrode (CNT working, Ag/Ag^{+} reference, and Pt counter electrodes) configuration using 1M tetraethylammonium tetrafluoroborate (TEABF4, > 99%) in acetonitrile (ACN) in a Gamry reference 3000 electrochemical system. In these experiments, spray coated CNT electrodes on Al foils were fastened in a Teflon cell with an exposed area of ~0.5 cm^2 and were contacted with Ti foil. All CNT electrodes were pre-treated using voltammetric cycling from 0 to 2.0V at a scan rate of 100 mV/s until the current profile became constant. A typical cyclic voltammetry (CV) profile (Figs. 2(a)–2(c)) for all our samples did not show the presence of any redox reactions suggesting

EDLC behavior. Interestingly, as evident from Fig. 2(c), the net capacitance of NCNT samples was found to be higher than PCNT samples. This increase in capacitance may be rationalized as follows. Previously, Yamada and Bandaru have suggested that the C_{tot} of nanomaterial electrodes consists of both their C_Q and the double layer capacitance (C_{dl}) in series, i.e., $1/C_{tot} = 1/C_Q + 1/C_{dl}$. C_Q depends upon the DOS at the Fermi energy (E_F) and may be quantified as $C_Q = e^2\ DOS(E_F)$. Traditionally, C_Q for CNTs is low because their quasi one-dimensional nature results in van Hove singularities in the DOS structure with vanishing DOS at E_F. It was earlier suggested that the measured capacitance of CNT structures is at least an order of magnitude lower than the expected C_{dl} (from the surface area measurements) due to the presence of lower C_Q in series.

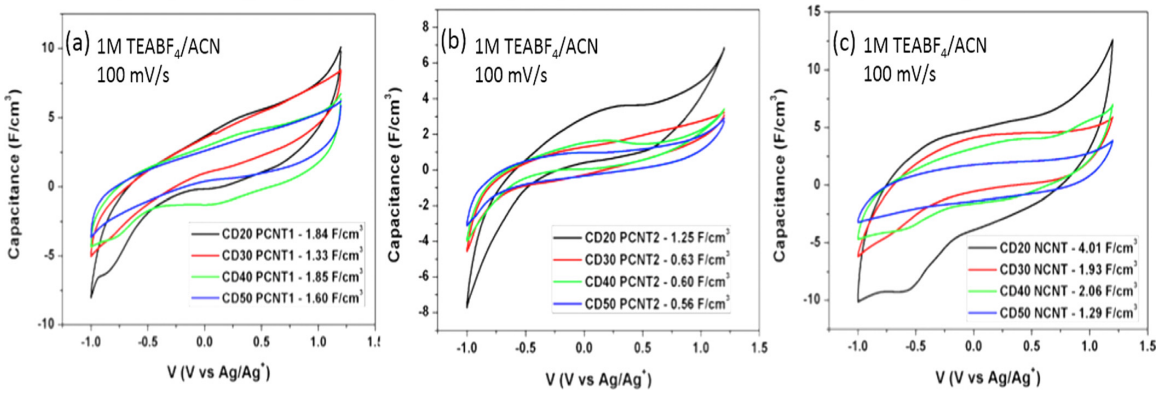


Figure 5.2: (a)–(c) Scan rate normalized cyclic voltammetry loops for two types of pristine CNTs (PCNT1 and PCNT 2) and NCNTs on CD20 Al foil. Clearly, no redox peaks are observed, indicating that the samples exhibit good electrical double layer capacitor behavior. The net capacitance of NCNTs in (c) is higher compared to PCNT1

and PCNT2 due to an increased quantum capacitance resulting from the presence of N-dopants. Quantum capacitance is directly proportional to the density of electronic states at the Fermi level (DOS(E_F)). N-dopants can increase the DOS(E_F) by providing additional electrons to the honeycomb carbon lattice, and thereby result in an increase in DOS(E_F).

Thus, N-doping in CNTs is expected to increase DOS (E_F) leading to an increase in the C_Q because N dopants can disrupt the CNT lattice and inject an extra lone pair of electrons into the delocalized carbon π-orbitals [88]. An increase C_Q through DOS (E_F), arising from N doping, diminishes the $1/C_Q$ component allowing one to harness the true double layer capacitance of CNTs, as shown in Fig. 5.2(c). The volumetric capacitance was calculated by the following equation:

$$C_{vol} = \frac{C_{meas}}{V_e} \tag{5.1}$$

where C_{meas} is the measured single electrode capacitance. The total volume of the electrode is calculated by $V_e = (T_{Al} + T_{CNT})$ *x Area of electrode*, where T_{Al} and T_{CNT} are the thickness of the Al substrate and CNT layer, respectively.

Based on the better performance of NCNT spray coated single-electrodes, we fabricated symmetric EDLC coin cells and jellyroll devices (see Fig. 5.3(a)) comprised CD20-NCNTs. The highest energy and power density of the CD20-NCNT coin cells in

TEABF4 -ACN (with Celgard 2325, 25 μm thick separators) were found to be ~0.75 mW h/cm^3 and 480 mW/cm^3. These energy and power density values are only moderate since the cell voltage is limited to 2V by the TEABF4 -ACN electrolyte. Accordingly, we repeated our coin cell measurement in an ionic liquid, viz., 1-Butyl-3-methylimidazolium tetrafluoroborate ([BMIM][BF4]) along with EnergainVR separator (DuPont) to increase the voltage window of the cell to 3 V. Prior to the coin cell assembly with ionic liquid, each electrode and separator were soaked overnight (~20 h) in [BMIM][BF4]. The separator was placed between the two electrodes in a coin cell apparatus (MTI Corp.), as shown in Fig. 5.3(a). CV profiles of as-assembled coin cell with [BMIM][BF4] electrolyte were recorded at various scan rates over a cell voltage range of 0 to 3 V, as shown in Fig. 5.3(b). The Nyquist plot for these coin cells showed that the internal resistance for our CD20-NCNT (~20 Ω) samples is moderately higher than CNTs directly grown on Al electrodes (~1 Ω) in Ref. [14]. Such a result is expected since CVD grown CNTs on Al foils are vertically aligned and have negligible inter-tube junction resistance unlike randomly oriented CNTs in the pores of CD20 Al foils.

The charge–discharge characteristics of CD20-NCNT coin cells at 0.8 and 1mA are shown in Fig. 5.3(c). From the discharge measurements, we calculated the energy and power density of the electrodes shown in Ragone plot (Fig 5.3(d)) using $W=1/2C_{tot}V^2$, where W is the energy density and V is the cell voltage, and $P=\Delta W/\Delta t$, where P is the power density and Δt is the discharge time. The volumetric specific energy and power densities are calculated by normalizing the W and P value by the total volume

of the two electrodes. We observed that the performance of all the EDLC coin cells was stable for over ten thousand cycles with a drop of 12% in performance (Fig. 5.3(e)). After 10 000 cycles, we recovered the spray coated CNTs and recoated them on the tested Al foil, in other words, we recycled both the active (CNTs) and current collector (Al foil) materials. As seen in the inset of Fig. 5.3(e), the recycled supercapacitor coin cell exhibited a drop of ~40% performance but could be run at 60% of the original material performance for another 10 000 cycle, suggesting excellent sustainability of our spray coated electrodes.

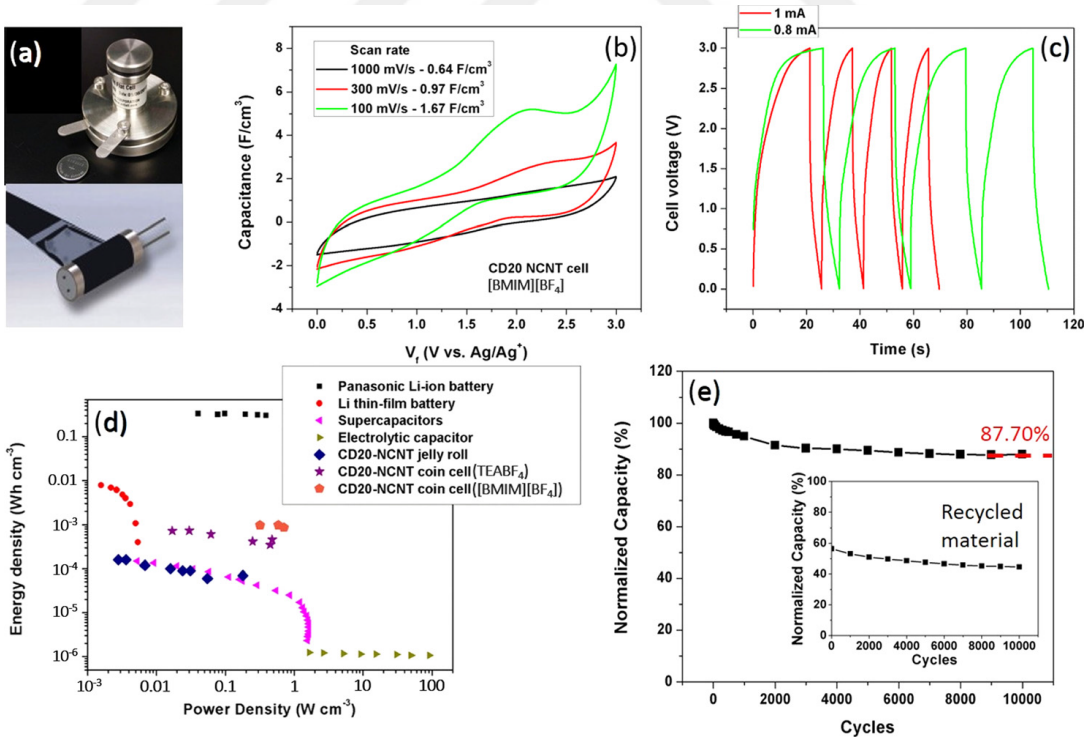


Figure 5.3: (a) The top panel shows a coin cell assembly for testing spray coated nitrogen doped carbon nanotube (NCNT) electrodes, while the bottom panel shows the

structure of a jellyroll capacitor. (b) Cyclic voltammetry profiles of as-assembled coin cell with electrolyte of [BMIM][BF4]. (c) The charge–discharge characteristics of CD20-NCNT coin cells at 0.8 and 1 mA. (d) Ragone plot comparing the performance of CD20 NCNT coin cell and jellyroll devices with TEABF4-ACN and [BMIM][BF4] electrolytes to conventional supercapacitors, Li-thin film batteries, and other energy storage devices (see Ref. [6]), and (e) the coin cell device made from CD20-NCNT electrodes exhibited excellent cycle stability with only ~12.3% degradation in performance over 10 000 cycles. After 10 000 cycles, the Al foil current collector and NCNT material were used for the second time to make recycled electrodes. The recycled device (with recycled electrodes) exhibited 60% specific capacity (see inset) of the as-prepared NCNTs (electrodes in run-1 shown in Fig. 5.3(b)) indicating excellent material recyclability.

As shown in Fig. 5.3(d), we found that the increase in the cell voltage leads to energy and power densities as high as 1 mWh/cm^3 and 700 mW/cm^3 on par with Li-thin film batteries. While the coin cells provide excellent platform to test devices in the laboratory, the main challenge is to fabricate supercapacitor devices in the jellyroll form without introducing any micro-cracks that adversely influence the electrode conductivity. Accordingly, we used the CD20-NCNT electrodes to fabricate jellyroll supercapacitor devices and evaluated their performance with the traditional organic electrolyte (viz., TEABF4 -ACN) used in commercial devices, as shown in Fig. 5.3(d) . The energy and power density values for these jellyroll devices are on par with the traditional supercapacitors which use binders to enhance the adhesion of activated carbon

to the current collector. Our facile spray coating method (cf. Fig. 5.1(a)) eliminates the use of binder by using the porosity of Al foils. The spraying rate of this coating system (~4 cm^2/s) is an order of magnitude higher than traditional CVD systems and could potentially lead to high-throughput EDLC device manufacturing.

5.3 Cost Analysis

A cost analysis of the supercapacitor coin cells produced in the laboratory by hand has little relevance to their economic performance application since the extrapolations do not scale linearly from lab-production to large-scale manufacturing. Accordingly, in order to estimate industrial largescale production of supercapacitor cells, up-scaling needs must be included. As reported by Dura *et al*. [96], the sustaining costs of supercapacitor production (K_{cell}) may be expressed as

$$K_{cell} = M_i \cdot P_{Ei} + E_i \cdot P_{Ei} + X_i \cdot P_{Xi} + Y_i \cdot P_{Yi} \quad (5.2)$$

In Eq. (5.2), *M , E , X , and Y* represent the rate of consumption of materials, energy, labor, and maintenance, while P_n *(n.M, E, X, and Y)* is the corresponding price for the considered material, energy, labor, and maintenance for the individual process steps *i* of the production line. It has been previously shown that term 1 in Eq. (5.2) contributes up to 60% of K_{cell}, leaving the other three terms sum up to 40%. Traditional supercapacitor production is a 12 step process (each step contributing ~3.5% to *Kcell*) wherein 5 steps involve electrode production (viz., mixing active material with binder, coating, calendering, slitting, and drying), while 7 steps are necessary for the cell assembly [96].

Considering that our electrode production involves three-step process (sonication, spraying, and drying), we expect that the production costs are reduced by ~7% in our process. Furthermore, our spray coating process also eliminates the use of binder materials that contribute ~10% of the materials cost. Overall, using our approach, the cost of rolling a jellyroll capacitor can be reduced by ~17%. More importantly, conventional supercapacitors containing activated carbon provide energy densities only as high as ~0.1 mW h/cm^3.

5.4 Conclusion

We present a scalable roll-to-roll (R2R) spray coating process for synthesizing randomly oriented multi-walled carbon nanotubes electrodes on Al foils. The coin and jellyroll type supercapacitors comprising such electrodes yield high power densities (~700 mW/cm^3) and energy densities (1 mWh/cm^3) on par with Li-ion thin film batteries. These devices exhibit excellent cycle stability with no loss in performance over more than a thousand cycles. Our cost analysis shows that the R2R spray coating process can produce supercapacitors with 10 times the energy density of conventional activated carbon devices at ~17% lower cost.

CHAPTER SIX

MODULATION OF THE ELECTROSTATIC AND QUANTUM CAPACITANCES OF FEW LAYERED GRAPHENES THROUGH PLASMA PROCESSING

6.1 Introduction

A comprehensive understanding of the characteristics of graphene [97] with regard to its unique electrical and structural attributes would be incomplete unless the inevitable presences of defects have been considered. While such imperfections may limit the realization of theoretically predicted characteristics [98], they may also be vital for uncovering new fundamental phenomena and related applications. Here we show that the charged defect generation, through argon ion based plasma processing, in few layer graphene (FLG) could be integral to the substantial enhancement of the electrical capacitance and be of potential use [99] in electrochemical (EC) energy storage [76]. By combining EC characterization techniques with detailed Raman spectroscopic analysis, we elucidate the contributions of plasma-induced defects to electrostatic and quantum capacitance.

6.2 Experimental section

Few-layer graphene samples were prepared using chemical vapor deposition technique. Briefly, 25 μm Ni foils were placed away from the center of tube furnace (diameter: 24 mm), which was maintained at 900°C under a flow of Ar (230 sccm) and H_2 (120 sccm). After 60 min, Ni foils were moved to the center and graphene was synthesized by decomposing methane (10 sccm) for 10 min at a reduced temperature (850°C). Subsequently, methane flow was shut off and the samples were moved away from the center. The furnace temperature was ramped down to 400°C at 5°C/min and was maintained at 400°C for 90 min. The H_2 flow was shut off immediately upon reaching 400°C, and the samples were cooled to room temperature under Ar flow [100]. The prepared FLGs (referred to hereafter, as "pristine") were subsequently subjected to Ar based plasma processing to intentionally [101] induce charged defects. Argon was chosen because the constituent ionic species are limited [102] to Ar^+, implying relatively simple plasma chemistry [103]. The plasma processing was carried out in a customized reactive ion etching chamber with an electrode bias (~ −100 V) and an ion density [104] of the order of $10^{11}/cm^3$. The applied electrical power (in watts), which would be proportional to the electric field between the electrodes in the chamber, was used as a parameter to tune the extent of Ar^+ graphene interaction over a range of time.

6.3 Results and Discussion

It was hypothesized, based on previous experimental evidence [105], that dangling bond rich [106] edge plane defects could be created in the FLGs during Ar plasma exposure through the removal of carbon atoms [105], see Fig. 6.1(a). Considering that the formation energy of extended defects (~1.1 eV for divacancies) [98] is significantly smaller than that of point defects (~7 eV), the creation of pores (or extended defects) in graphene with chiral edges (i.e., containing a combination of armchair: AC, and zigzag: ZZ, type edges) is expected. Subsequently, the structural attributes of the processed FLG films were analyzed through Raman spectroscopy to characterize the effects of plasma processing; see Fig. 6.1(b). The relative variation of the *D*- peak observed at ~1350 cm^{-1} (which is disorder induced and originates from higher order electron−phonon scattering processes) with respect to the *G*- peak at ~1580 cm−1 (which arises due to normal first order scattering processes in graphene) was used as an initial metric [107]. The normalization of the Raman peaks was done with respect to the *G*-peak, per convention. It was seen that while the pristine FLG has an A_D/A_G ratio close to zero (where A refers to the net area integrated intensity of the respective peak), there was a substantial increase of the *D*-peak intensity with increasing Ar^+ plasma exposure [108]. The A_D/A_G ratio has often been used, through the Tuinstra-Koenig relation [109,110] (typically adapted [111] through $A_D/A_G = (560/E_L^4)(1/L_a)$, where E_L is the input laser energy, in electronvolts) as a measure of an effective crystallite size/correlation length

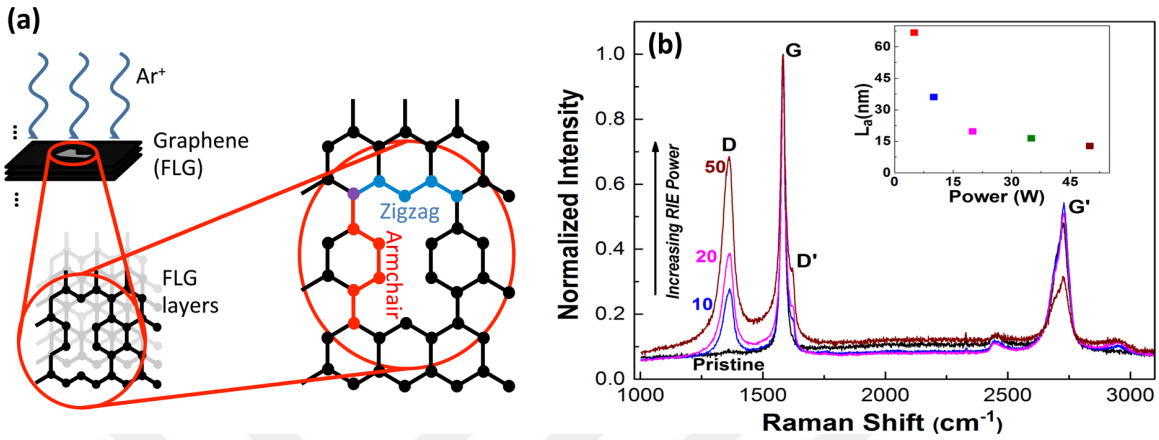


Figure 6.1: Artificial introduction of charged states in few layer graphenes. (a) Argon ion based plasma processing was used to purposefully create defects, such as dangling bond rich edge plane defects of the armchair or zigzag varieties, in few layer graphene (FLG) structures. (b) Enhanced plasma processing applied to the pristine sample, results in a substantial intensity enhancement of the *D*- and *D′*-peaks as seen in the Raman spectra (normalized to the *G*-peak). An increase in power, say to 50 W, may result in irreversible changes due to graphene removal. The plot of the Tuinstra−Koenig correlation length (L_a) obtained from the area integrated *D*- to *G*-peak intensity ratio is shown in the inset and indicates decreased crystallite size with increased plasma power.

(L_a) in nanographites; see inset Fig. 6.1(b). Concomitantly, the *G′* peak feature at ~2700 cm^{-1} (close to the second harmonic of the *D* peak and characteristic of double/triple resonance processes in graphene [107]) was also observed. It is well-known that the deconvolution of the *G′*-peak into either a single peak or multiple peaks is indicative of the state of the graphene, that is, the number as well as orientation of the layers in the

FLGs [112]. The decrease of the *G′*-peak intensity seen in Fig. 6.1(b) concurs with the enhancement in *D*-peak intensity, which is due to the defects induced by high plasma processing power.

While the *D*-peak increase in the processed FLGs seems to record a net increase in defect content, it has also been indicated that this feature is typical of AC edges and not of ZZ edge defects based on momentum conservation principles [113]. An important attribute of ZZ defects is that they may be electrically active and could contribute to an enhanced density of states (DOS) near the Fermi energy (E_F) [114], much more than the AC edge defects (which contribute less due to the two constituent carbon atoms belonging to different sublattices [111]).

In this context, a nanostructure characteristic that is DOS specific is the quantum capacitance [115,116], C_Q, which is defined through (see Appendix B)

$$C_Q = e^2 DOS(E_F) = e^2 \sqrt{\frac{4}{\pi} \frac{n_{2D}}{(\hbar v_F)^2}} \tag{6.1}$$

In the above relation, e is the unit of elementary electronic charge, n_{2D} is the carrier density (in cm^{-2}) of the 2D graphene, $\hbar$ is the reduced Planck constant (=1.05 $x10^{-34}$ Js), and v_F is the Fermi velocity in m/s. We have previously shown [87] through electrochemical characterization that the C_Q is in series with the nominal double-layer capacitance, C_{dl}, and could be inferred through the total measured capacitance (C_{meas}).

However, for the six-layer FLG used in our studies (see Fig. 6.2), it may also be necessary

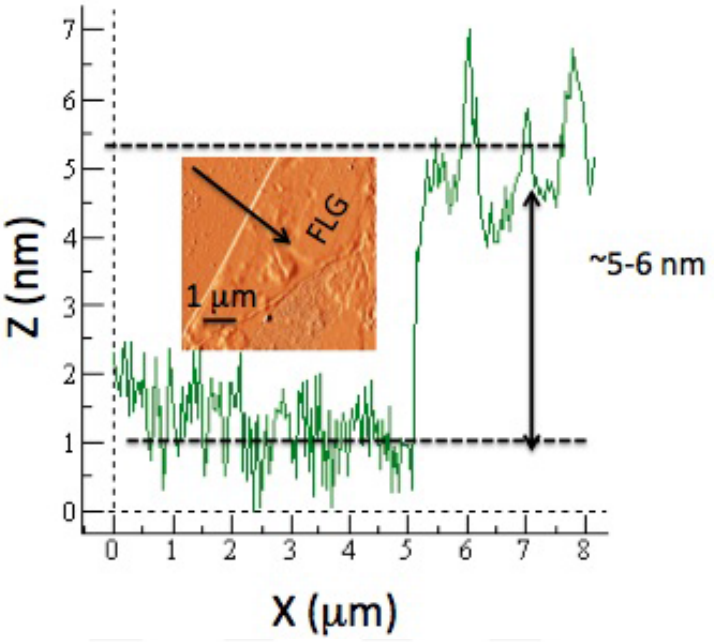


Figure 6.2: Atomic Force Microscopy (AFM) indicating the typical thickness of the investigated FLG samples. The step on the right indicates a 5±1 layer FLG.

to incorporate a space charge capacitance [117] (C_{SC}), which arises due to the screening of the electrolyte charge in the inner graphene layers by the outer graphene layers, and which would also be in series with C_{DL} (also see Appendix B). We consider the relevant length scale for the charge storage to be defined over an equivalent Thomas− Fermi screening length (λ_{TF}) [118]; see Appendix B with the C_{SC} given by

$$C_{SC} = \frac{\varepsilon}{\lambda_{TF}} = \sqrt{\frac{2\varepsilon e^2 n}{E_F}} \tag{6.2}$$

ε is the dielectric permittivity (~5.7 ε_0 for graphene [119], where ε_0 = 8.854 x 10^{-12} C^2/Nm^2) and n is the carrier density per unit volume in units of cm^{-3}. Consequently, the individual contributions to the C_{meas} would be manifested through:

$$\frac{1}{C_{meas}} = \frac{1}{C_{DL}} + \frac{1}{C_Q} + \frac{1}{C_{SC}} \tag{6.3}$$

For insight into C_Q and C_{SC} of plasma processed FLGs, we conducted cyclic voltammetry (CV) of FLG-based electrodes (as the working electrode in a three electrode setup), in an organic electrolyte consisting of 0.25 M tetrabutylammonium hexafl-uorophosphate (TBAHFP) dissolved in 1 M acetonitrile, the results of which are shown in Fig. 6.3(a). The area enclosed by the CV curves divided by the voltage scan rate (v) is directly related to the net charge, and was used to estimate C_{meas}. The absence of peaks in the CV plots indicates the lack of redox reactions and faradaic capacitance (C_F) contributions [120]. It was seen that the C_{meas} increased substantially as a function of the Ar^+ plasma power: Fig. 6.3(b) and Table 6.1. The more than doubling of the C_{meas} from 1.9 μF/cm^2 (for the pristine sample) to 4.7 μF/cm^2 (for the sample subject to 20 W plasma) is remarkable and suggests a novel means of substantially enhancing capacitance. While it is indicated in Fig. 6.3(b), as well as in Table 6.1, that increased power (for example, at and beyond 35 W) causes a reduction in the C_{meas}, the decrease may be due to the strong lattice disruption and/or etching away of graphene as suggested through the Raman spectra and optical microscopy. It was ensured that the Ni substrate was not involved in such estimates.

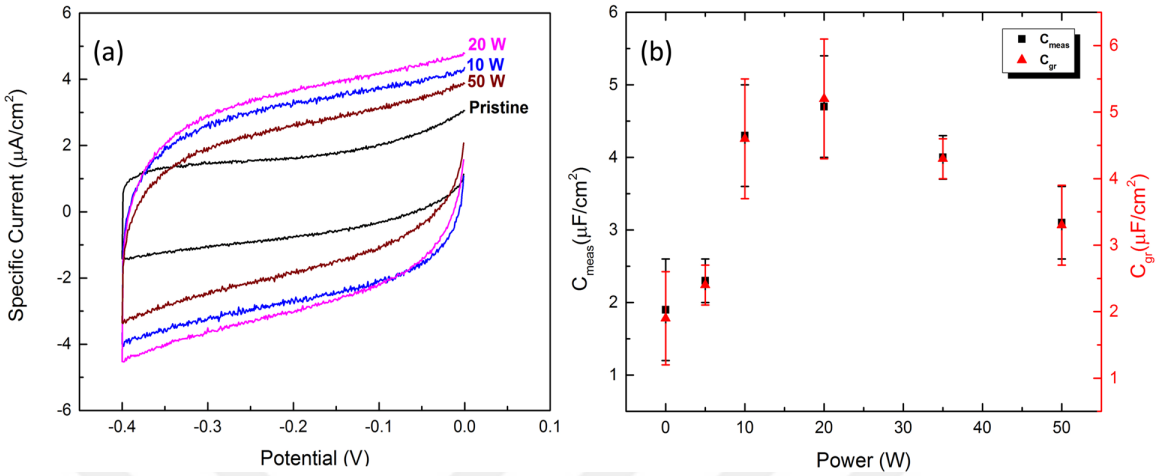


Figure 6.3: Electrochemical characterization of argon plasma processed FLGs. (a) CV characterization of plasma processed FLG samples (in 0.25 M TBAHFP dissolved in a 1 M acetonitrile). The area enclosed by the CV curves was used to parametrize the C_{meas}, which increases with plasma power (indicated on the figure). (b) A close to 3-fold enhancement in the C_{meas} (left axis) and the aggregated contributions of the computed C_{SC} and the C_Q (right axis), i.e., $1/C_{gr} = 1/C_{SC} + 1/C_Q$, as a function of the plasma power. The C_{gr} is in series with the nominal double-layer capacitance and is related to the induced charged defect density.

We do not use the F/g metric for reporting the capacitance values as is often done in extant literature, as the specific surface area (in m^2/g) is (a) not well-known, and (b) not easily measurable. Indeed, there have been a lot of exaggerations in literature through the use of the theoretical SSA.

P	C_{meas}	C_{sc}	C_Q	$n_{2D,0}$	n	v_F	E_F
w	$\mu F/cm^2$	$\mu F/cm^2$	$\mu F/cm^2$	$(\times 10^{12})$ cm^{-2}	$(\times 10^{19})$ cm^{-3}	$(\times 10^6)$ m/s	meV
0	1.9 ± 0.7	2.5	9.1	4.5	1.0	1.00	247
5	2.3 ± 0.3	3.2	11.0	7.1	1.9	0.97	302
10	4.3 ± 0.7	7.3	20.3	37	22	0.95	669
20	4.7 ± 0.7	8.4	23.1	43	29	0.86	661
35	4.0 ± 0.3	6.6	19.6	28	15	0.87	533
50	3.1 ± 0.5	5.0	14.2	19	8.5	1.10	562

[a]The values of the two-dimensional carrier density ($n_{2D,0}$), the volumetric charge density (n), the Fermi-velocity (v_F) and the Fermi energy (E_F) were consequently deduced.

Table 6.1: Argon plasma power (P) used to systematically modulate the experimentally measured capacitance (C_{meas}) of the FLG, which deconvolved to yield the space-charge capacitance (C_{SC}) and the quantum capacitance (C_Q) in accordance with Eq 6.1, 6.2, and 6.3.

Using nominally identical electrolyte and experimental conditions and assuming that C_{DL} would be a function only of the electrolyte concentration [120], an increased current in the voltammogram while the shape remains nearly rectangular, is characteristic of additional capacitance contributions, from C_{SC} and C_Q. For calibration of the constituents of C_{meas}, we used the bare Ni foil substrate, C_{SC}, and C_Q of which would be effectively very large due to its metallic nature. The C_{meas} should then be close to the C_{DL}, from eq 3. A value for the C_{DL} of around 20 μF/cm^2 was measured for polished Ni foil. It should be noted that any enhancement possibly due to the area increase brought about by, for example, a change in surface topography [121] would only further minimize the C_{DL} contribution and not substantially alter the conclusions. The difference between C_{meas} (in FLG samples), as in Fig. 6.3(b), and C_{DL} (obtained from Ni foil experiments) could then be attributed to the C_{SC} and C_Q of the FLG. We then proceeded to evaluate the relative partitioning of the C_{SC} and C_Q from eqs 6.1 and 6.2. In addition to the knowledge of the

v_F, the n_{2D} (for understanding the variation of C_Q) and n (for the C_{SC}) and the related E_F must be recognized and estimated (Table 6.1).

The v_F was found using Raman spectroscopy through considering the dispersion of the G' -peak frequency ($\omega_{G'}$) with laser energy (E_L). Such a variation has previously been understood [122] in terms of a relation of the form: $\omega G' = aE_L + b$, where a is the ratio [123] of the respective phonon velocity, v_{ph}, to the v_F near the K-point of the Brillouin zone. The b connotes the in-plane transverse optical phonon (iTO) frequency at the K-point with a larger value marking a hardening of the phonon mode frequency. The G'-peak, from Fig 6.1(b) could be adequately fitted through deconvolution into two peaks: Fig. 6.4(a), termed $2D_1$ (smaller energy/wavenumber peak) and $2D_2$ (the higher wavenumber peak). The relatively prominent left shoulder to the peak as well as the overall peak width (of ~70 cm^{-1}) may be indicative of highly oriented pyrolytic graphite (HOPG)-like character [124]. By plotting the energy dispersions of the $2D_1$ and $2D_2$ peaks at three laser energies (1.96 eV, 633 nm; 2.41 eV, 514 nm; and 2.54 eV, 488 nm), as shown in Fig. 6.4(b), we obtained increasing a values for the $2D_1$ peak as a function of plasma processing power (enhanced by ~16%; from ~92 cm^{-1}/eV for the pristine sample to ~107 cm^{-1}/eV for the 20 W processed sample) with a much smaller change for the $2D_2$ peak, from ~86 cm^{-1}/eV in the pristine sample to ~88 cm^{-1}/eV for the 20 W sample. Concomitantly, the b values for the $2D_1$ peak varied by ~1% on the application of plasma power, with a much smaller change for the $2D_2$ peak; see intercepts in Fig. 6.4(b). Because of the small change of the b, we assumed a relative constancy of the v_{ph} and the

origins of the change in *a*, for example, for the $2D_1$ peak, to be mostly from a change in the v_F. With the pristine sample as a reference, the v_F variation as a function of the plasma power was computed from the a (see Table 6.1) and has also been plotted in the inset to Fig. 6.4(b). The initially lowered v_F was suggestive of positively charged defects/p-type doping due to the plasma processing [122].

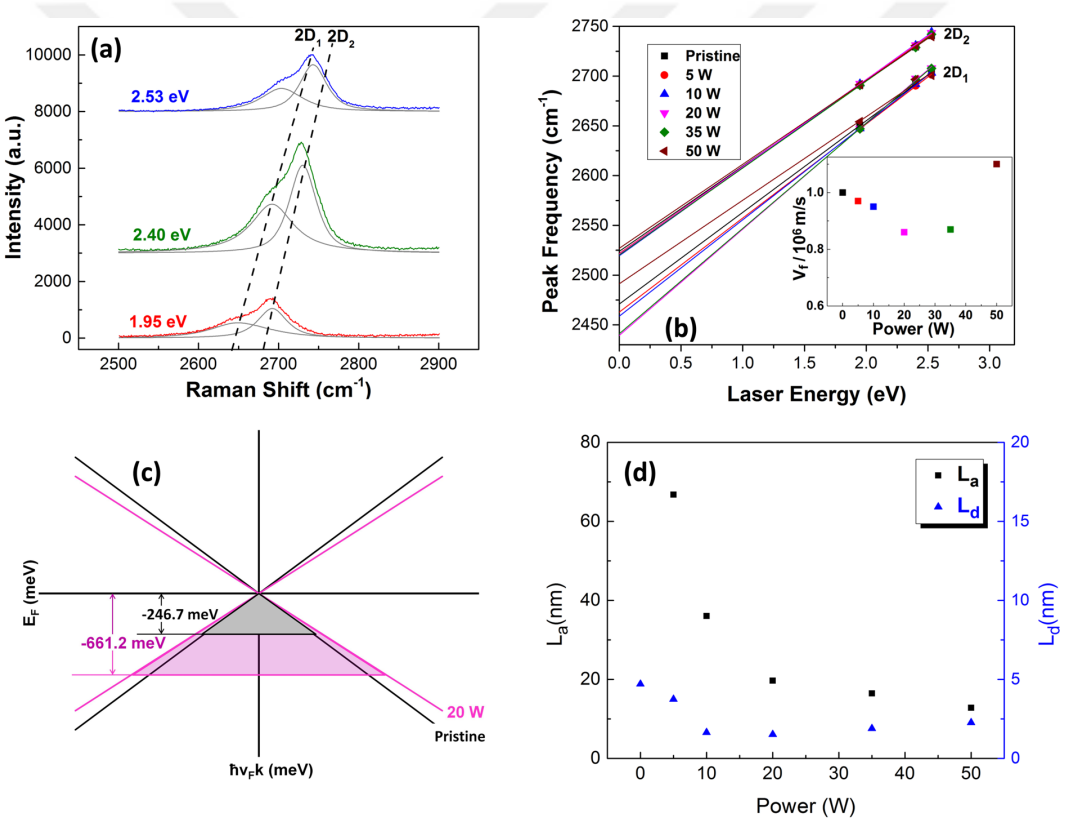


Figure 6.4: Determination of the charge configurations and charge correlation length scales. (a) The energy dispersion of the *G′*-peak indicated a blueshift and was composed of individual variation of the deconvolved $2D_1$ and $2D_2$ constituents. The laser energies, used for the Raman spectroscopy, are indicated on the individual plots. The relatively prominent left shoulder as well as the overall peak width (of ~70 cm^{-1}) seems to indicate

a HOPG character to the processed FLGs. (b) The variation of the $2D_1$ and $2D_2$ peak frequency ($\omega G'$) with Raman laser energy was fit to a straight-line, as expressed through $\omega G' = aE_L + b$ with a related to the phonon velocity (v_{ph}) / Fermi velocity (v_F) ratio and b A larger change in the was seen for the $2D_1$ peak and was used to infer a v_F modulation due to plasma processing. The inset shows the variation of the computed v_F with plasma power. (c) While the interlayer interaction in FLG has been implicated in a nonlinear energy dispersion, for example, a hyperbolic dispersion for bilayer graphene in the vicinity of the E_F, a linear $E-k$ energy dispersion relation could be considered[125] for insight. The plasma processing introduced positive charges akin to p-type doping into the FLG. The enhanced charge density increased the E_F from ~247 to ~661 meV (at 20 W plasma power), which was reckoned with respect to $E = 0$ point, along with a reduced v_F that was indicated by the decreased slope. (d) A charge correlation length, L_d (right axis), as deduced from the carrier density in the graphene sheet closest to the electrolyte, was smaller compared to the Tuinstra−Koenig correlation length, L_a (left axis), as deduced from Raman spectroscopy.

For obtaining the carrier concentrations to accommodate the partitioning into the various capacitances consistent with eqs 6.1− 6.3, we numerically varied the n_{2D} (i.e., = $n_{2D,0}$) of the graphene layer closest to the electrolyte until the respective C_{SC} and C_Q were obtained and their sum in accordance with eq 6.3 matched the C_{meas}; see Table 1. This involved for the C_Q in eq 6.1 the net n_{2D} calculated using the summation of the carrier

densities for all the FLG constituent layers, that is, $\sum_{l=0}^{N} = n_{2D,l}$, where $n_{2D,l}$ is the carrier density in the *l* th layer, for the N + 1 layer FLG. In our experiments, N = 5. The $n_{2D,\ l} = n_{2D,0}\ exp[-lx/\lambda_{TF}]$ with x being the distance between the layers of the FLG samples (see Appendix B). The estimation of the λ_{TF} for eq 6.2, also used an $E_F\ (= \hbar v_F(\pi\ n_{2D,\ 0})^{1/2}\ )$ (see Appendix B). The resultant variation of the series addition of the C_{SC} and the C_Q is indicated as C_{gr} and indicated in Fig. 6.3(b).

The estimated E_F (see Table 6.1), showed a close to 3-fold enhancement from ~247 meV (for the pristine sample) to ~661 meV (with 20 W plasma power). The underlying cause of an enhanced C_Q may then be ascribed to the decreasing E_F (in the negative sense, as would be the case for effective p-type doping) as schematically shown in Fig. 6.4(c). Generally, the effects of the Ar plasma treatment have been shown to be very reproducible, within the error bars represented by the data in Fig. 6.3(b). However, on further plasma processing (e.g., the 35 and 50 W cases), while the v_F appears to increase, the E_F diminishes (Table 6.1). FLG fragmentation at such high powers, yielding negatively charged defects due to dominance of edge states, could be playing a role in such observations [122,126].

Corresponding to the estimated $n_{2D,0}$, we defined a charge correlation length, $L_d=1/(n_{2D,\ 0})^{1/2}$, which may be understood as the average distance between charges (that could have arisen due to Ar^+ plasma induced defects) that contribute to the C_Q as well as the C_{SC}; also see Appendix A. Such a length scale should be compared to the more

conventional Tuinstra− Koenig correlation length (L_a), discussed earlier in the context of Raman spectroscopy, where $A_D/A_G \sim 1/L_a$. In Fig. 6.4(d) the respective variation of the L_d (right axis) and the L_a (left axis) as a function of the plasma power has been plotted. Note that the L_a is undefined for the pristine sample due to the negligible *D*-peak intensity; see Fig. 6.1(b). While a steady decrease of the L_a due to reduced crystallinity is expected, it was noted that (a) the L_d was typically smaller compared to the L_a, and (b) a definitive L_d may be prescribed even for the pristine sample. We further interpret L_d through the hypothesis that charged defects that contribute to electrochemical characteristics may not correspond to an effective crystallite size, considered through L_a. Instead, defects that are not diagnosed through Raman spectroscopy, e.g., ZZ edge states, may be relevant. An enhanced charged defect density would result in a lower L_d.

Having shown that the measured capacitance may be increased substantially through plasma processing, we now indicate further methodologies for the control of the net FLG capacitance. With such an aim, the argon plasma processed FLGs were subsequently subject to a hydrogen plasma, which had been shown [105] to be effective in passivating the number of dangling bonds and associated charged defect states. The influence of the charge contributing defects could then possibly be reduced with a concomitant decrease in the C_{meas}. In a typical hydrogen plasma [127], there is a large variety of hydrogen ions, e.g., H^+, H_2^+, H_3^+, etc. and the processing conditions, mainly the gas pressure, must be regulated for the dominance of specific ions. Also, lower pressures may cause the hydrogen ions to induce additional defects [105]. Considering

such factors, we used a hydrogen gas pressure of 1 Torr with H_3^+ as the predominant ion and obtained consistent and reproducible results. The hydrogen plasma power was set to be the same as that used for the initial Ar^+ plasma processing. The resultant lowering of the C_{meas} is indicated in Fig. 6.5(a) and the concomitant Raman spectra are shown in Fig. 6.5(b). For the 20 W Ar^+ plasma power processed sample, the H_3^+ plasma was effective in halving the capacitance and reduced the *D*-peak intensity as well. However, neither the C_{meas} nor the Raman intensity return to that noted for the pristine sample suggesting that (i) the hydrogen plasma may not be completely effective, or (ii) that there may be some residual defects that resist passivation. It was also noted through preliminary X-ray photoelectron spectroscopy (XPS) measurements (see Appendix B) that there was little evidence of the contribution of the surface functional groups, for example, quinones,[128] to the capacitance, as corroborated by a smooth CV scan; see Fig. 6.3(a).

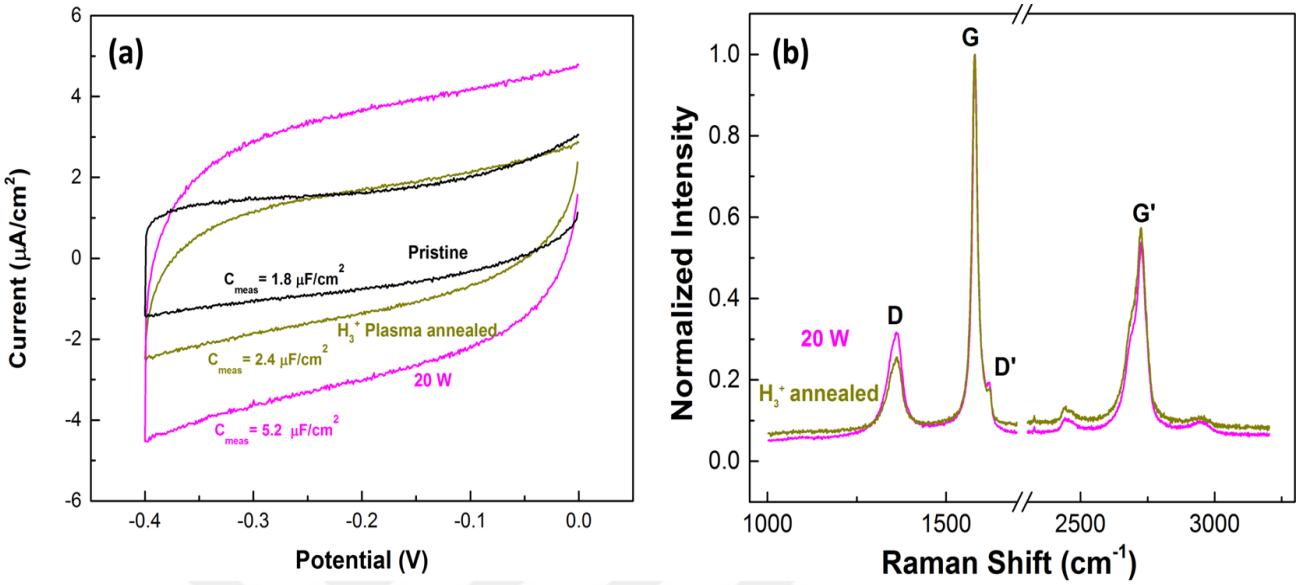


Figure 6.5: Tuning the capacitance of FLGs through hydrogen plasma treatment. (a) A pronounced 2-fold reduction of the capacitance was observed through CV characterization of H^{3+} ion plasma exposed plasma processed samples. Such observations validate the hypothesis that hydrogen passivates the charged defect sites and reduces the capacitance tending toward the pristine state. A residual capacitance on hydrogen exposure may indicate that there may be some residual defects that resist passivation. (b) The decrease in the FLG defect density on hydrogen ion exposure was manifested in the Raman spectra through a decreased A_D/A_G ratio and an increase in the L_a

6.4 Conclusion

In summary, we have indicated a methodology for both increasing and decreasing the electrochemical capacitance of FLG-based nanographites through a combination of

argon and hydrogen-based plasma processing. In addition to the utility for charge storage, our work contributes to understanding and controlling the charge storage characteristics. The proposal of a new length scale, L_d, correlated to electrically active defects contributing to the capacitance, which is smaller than the conventional Tuinstra− Koenig correlation length determined through Raman spectroscopy, implies a distinction between electrical and structural length scales.

CHAPTER SEVEN

DOPANT-CONFIGURATION CONTROLLED CARRIER SCATTERING IN GRAPHENE

7.1 Introduction

The discovery of graphene, a two-dimensional atom-thick sheet of sp^2 hybridized carbon atoms [129], has led to the experimental realization of quantum mechanical phenomena such as the quantum Hall effect at room temperature [130], quantized optical transmittance [131], non-local hot carrier transport [132], and Klein tunneling [133]. More importantly, the distinctive combination of high electron mobility (μ), optical transparency and gate/ dopant-tunable carrier density makes graphene an ideal platform for a multitude of photonic and optoelectronic applications over a wide range of frequencies. To truly harness the potential of this combination and make graphene-based efficient optoelectronic devices a reality, energy transport and relaxation pathways of photogenerated carriers in graphene must be tuned appropriately. Defects in graphene are often considered as "performance limiters" since they deteriorate the electron mobility μ. For example, epitaxial and mechanically exfoliated graphene possess exceptional μ ~15000 $cm^2\ V^{-1}\ s^{-1}$, whereas their chemical vapor deposition (CVD) grown counterparts exhibit much lower values ~1–5000 $cm^2\ V^{-1}\ s^{-1}$ due to the inherent presence of defects [134]. Such deterioration in μ primarily arises from the extra electron scattering terms introduced by grain boundaries and defects. Indeed, μ in CVD grown doped graphene is

highly compromised compared to that in pristine graphene due to the presence of additional scattering by the substituted dopants and related defects [135]. Although there is much effort focused on reducing defects in graphene to improve μ, it should be realized that defects provide an excellent handle and probably the only intrinsic way to control energy transport in graphene. In optoelectronic devices, when photoexcited electrons are scattered by phonons or defects, energy transferred to the lattice is dissipated as heat decreasing the net energy transported through charge carriers to drive a circuit. In the current scenario of graphene optoelectronic devices, a critical challenge is to increase the net charge carrier density and quench electron-defect relaxation pathways to extend photogenerated carrier lifetime. A new energy transport regime in graphene can be realized if electron-defect scattering mechanisms are efficiently quenched.

In this context, it is imperative to identify ideal dopant concentration and configuration in graphene for which the net carrier density (n) can be enhanced (without adversely affecting μ) with quenched electron-dopant scattering mechanisms. Previously, heteroatomic doping was found to result in many changes in the electronic structure of graphene in addition to simply shifting the Fermi level [134]. For instance, N-doping in CVD graphene resulted in a bandgap due to the suppression of electronic density of states near the Fermi level and a consequent reduction in μ [134–136] It is well known that N atoms can be substitutionally doped in the graphene lattice either in the pyridinic, pyrrolic or graphitic configurations (see Fig. 1(a)) [125,136–143]. Our density functional theory (DFT) calculations, described in this chapter, show that all three dopant configurations

(pyridinic, pyrrolic, and graphitic) are stable structures with a positive energy (>9.5 eV) released during the formation with graphitic dopants exhibiting the highest stability. In previous studies, we uncovered a strong correlation between the N bonding configuration and the accompanying vibrational properties of N-doped CVD graphene [125]: the N atoms bonded in the non-graphitic configurations (pyridinic and pyrrolic, observed using X-ray photoelectron spectroscopy or XPS) resulted in intense Raman *D* and *D′* bands, unlike the N atoms bonded in the graphitic configuration, even though the concentration of N dopants was higher in the latter case. Since dopant scattering is one of the dominant factors limiting the photo-response and electron mobility in doped graphene, it behooves us to investigate the influence of graphitic dopant configuration on the electronic and optical properties of doped graphene for improved device performance. The optical and nonlinear optical (NLO) properties of graphene arise mainly from the inter- and intra-band transitions, and are therefore ideal for probing dopant-induced changes in the electronic band structure of graphene. In tandem with NLO studies, ultrafast pump–probe measurements determine how electron–electron and electron-phonon scattering times (τ_1 and τ_2) that determine zero-field mobility μ_0) vary as a function of crystal coherence length (L_a) in N-doped graphene. This chapter juxtaposes data gathered from DFT, Raman, XPS, NLO, and ultrafast spectroscopic studies and concludes that graphitic dopant configuration in N-doped graphene preserves the crystal L_a, τ_1 and τ_2 similar to those in pristine graphene. These findings are apt for graphene-based applications such as optoelectronics, mode locking and pulse shaping [139].

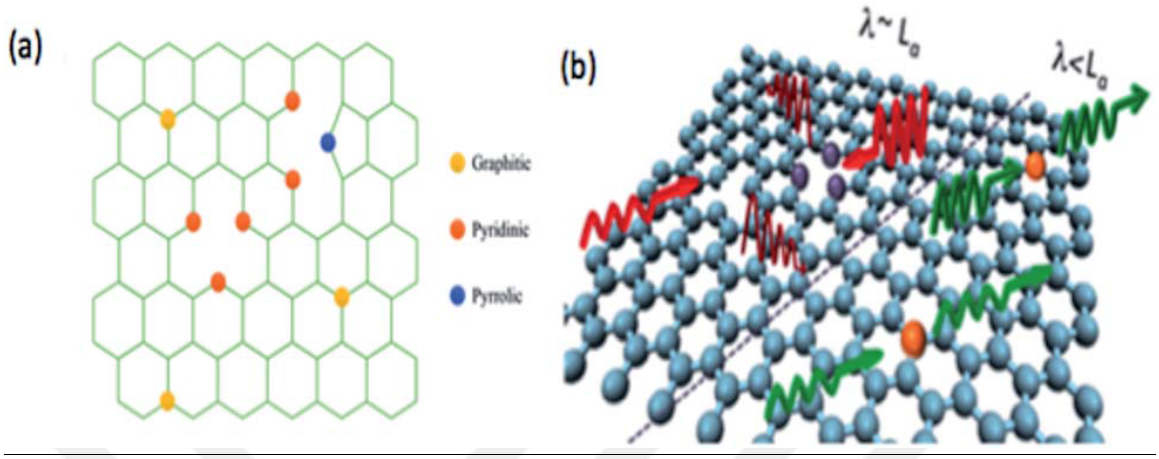


Figure 7.1: (a) Different configurations of nitrogen dopants in graphene include graphitic (yellow), pyridinic (orange), and pyrrolic (blue) dopants. (b) Regarding graphene as a two-dimensional electron gas system (2DEG), the average wavelength (l) of its electrons is determined by the Fermi wavevector (k_F) $k_F \sim (2\pi n)^{1/2}$, which depends solely on the net carrier density (n). When the crystal coherence length or inter-defect spacing (L_a) is comparable to l, carriers scatter off the defects (short relaxation time τ) and the carrier mobility μ is compromised as depicted to the left of the dashed line in the above schematic. Such is the case in doped graphene, where vacancies or dopants present in non-graphitic configurations (e.g., pyrrolic N-dopants shown in purple) significantly reduce L_a due to their extended interaction volume and thereby scatter electrons (scattering shown by red and maroon colored waves) very effectively. To the contrary, dopants present in graphitic configurations (orange atoms) act as point defects and do not adversely affect τ and μ as shown schematically on the right side of the dashed line.

7.2 Experimental section

7.2.1 N-doped bi-layer graphene synthesis

The N-doped bi-layer graphene used in this study were grown on Cu foils using a previously reported thermal CVD technique [125]. Briefly, Cu foils (5 mm x 20 mm) were placed in a 1 in diameter quartz tube furnace and heated to 1000 °C in 50 sccm of H_2 and 450 sccm of Ar flow. Next, 2 sccm of methane was bubbled through a mixture of benzylamine and acetonitrile into the furnace for 30 min, and the samples were cooled to room temperature under flowing H_2, Ar, and CH_4. The doped bi-layer graphene films formed on the Cu foils were then spin-coated with 4% poly-methyl methacrylate (PMMA) in anisole. Subsequently, the Cu foils were etched away using Transene Inc., CE-100 etchant and the bi-layer graphene attached to PMMA was carefully washed in 10% HCl and de-ionized water. Finally, the washed samples were transferred to 0.5 mm thick quartz substrates and annealed at 450 °C in Ar (300 sccm) and H_2 (700 sccm) for 2 h to remove the residual PMMA. By varying the volume percent of benzylamine and acetonitrile as 50:50, 0:100, and 75:25 several differently doped graphene samples were prepared with three N concentrations (Fig. 1(a)), which are referred below as S1 (pyrrolic), S2 (graphitic), and S3 (pyridinc), respectively. For each concentration, at least three sister samples were used in our spectroscopic studies.

7.2.2 Open aperture Z-scan

To quantify the absorptive nonlinear characteristics for each of three concentrations S1–S3, open aperture Z-scan technique was employed in both the nanosecond (ns) and femtosecond (fs) excitation regimes with the excitation source being (a) 5 ns Gaussian pulses of 532 nm from a Q-switched frequency doubled Nd:YAG laser, and (b) 100 fs Gaussian pulses of 800 nm from generatively amplified mode-locked Ti:Sapphire laser. The incident laser pulses were divided into two by a beam splitter, and the reflected beam was measured by a pyro-electric detector (RjP-735, Laser Probe Inc.) to correct for the pulse-to-pulse energy variations during data acquisition. Using a converging lens, the transmitted beam was focused onto the sample that was mounted on a computer-controlled translational stage. Through repeated knife-edge measurements, the beam radius at the focus was calculated to be ~20 mm and ~16 mm for ns and fs excitations, respectively. The beam propagation direction was taken as z with z = 0 being the focus. The input intensity/ fluence is different at each z point due to the variation in the crosssectional area of the focused beam. By translating the sample from -z to +z and measuring the sample transmission at each z point, intensity dependent transmission characteristics of each sample were determined. The measured Z-scan curves, which are plots of sample position vs. transmittance, were analyzed and the coefficients of nonlinearity were obtained from the best fit to the data.

7.2.3 Ultrafast degenerate pump–probe measurements

The ultrafast pump–probe measurements were carried out using 50 fs laser pulses with central photon energy of 1.57 eV derived from a Ti:Sapphire amplifier (Spitfire, Spectra Physics Inc.) operating at a pulse repetition rate of 1 kHz. The spot size (half-width at 1/e maximum) on the sample where the pump and probe beams overlap was kept at ~600 mm and 400 mm, respectively. The pulse width at the sample as determined using a thin beta-barium borate (BBO) crystal was ~70 fs. Polarizations of the pump and probe beams were kept perpendicular to each other to prevent scattered pump light from reaching the detector. The pump and probe beams were incident to the sample normal at a small angle of ~3 degrees between them to maximize their interaction, and their energies were maintained as 12 mJ and 23 nJ, respectively. The pump beam was modulated at 383 Hz using a mechanical chopper and the transmitted probe intensity was measured using a Si-PIN diode with lock-in detection.

7.3 Theoretical section

7.3.1 DFT Modeling

The three types of dopant configurations along with their electron density profiles have been analyzed through density functional theory (DFT) based atomistic tool kit virtual nano lab [144]. For this computational modeling, the exchange correlation

energies have been defined through generalized gradient approximation with revised Perdew–Burke–Ernzerhoff type parameterization, wherein the valence electrons were described by localized pseudo atomic orbital's (PAOs) with a double-z polarized basis set. A large plane wave mesh cut-off of 150 Ryd is used throughout the calculation with 1 x 10 x 10 k-point sampling to achieve the total energy convergence. In the full course of optimization, the run was performed with maximum force tolerance set at 0.05 eV $Å^{-1}$ and electron temperature 300 K. To verify the structural stability of pristine as well as doped (graphitic, pyridinic and pyrrolic) graphene, the binding energy of the system has been calculated. Formation energy is defined as the energy released on the formation of structure from free atoms and its positive value shows that the sheet is stable after introducing the dopants. It is calculated using the following equation $E_{for} = E_{ddg} - E_{dg} + n_V\mu_C - n_N\mu_N$, where E_{dg} and E_{ddg} are total energies of defected and defected-doped graphene (containing dopants and other defects such as vacancies as in the case of non-graphitic dopants). n_V and n_N are the density of carbon vacancies and nitrogen dopants respectively while μ_C and μ_N are the chemical potentials of carbon (in graphene) and nitrogen.

7.4 Results and Discussion

In a heuristic picture, graphene may be viewed as a two dimensional electron gas system (2DEG) whose Fermi wave vector (k_F) (and hence the wavelength λ of electrons) is determined solely by n as $k_F = (2\pi n)^{1/2}$. Under this premise, carrier mobility μ or carrier

relaxation time τ is impervious to defects when λ is sufficiently large compared to the average defect– defect distance L_a. Nonetheless, the presence of extended defects at a length scale comparable to λ can compromise μ and τ by efficiently scattering carriers (Fig. 1(b)). The 2DEG picture, though simplistic in nature, is pertinent even for other semimetals with more intricate Brillouin zones than graphene. Indeed, we have previously demonstrated that the magnitude and temperature dependence of μ and defect scattering in spark plasma sintered pellets of Bi nanoparticles remain unperturbed despite the introduction of defects in the pellet [145]. While Bi presents an intriguing example in its own right, CVD-grown bilayer graphene [146] serves as an exquisite platform to validate the 2DEG picture, and potentially lead to the realization of doped graphene with excellent μ. Doping graphene without affecting its μ or τ would allow a greater flexibility in the design and optimization of graphene-based nano-photonic, electronic, and optoelectronic devices. Accordingly, we built on the intriguing carbon–nitrogen chemistry to chemically grow bilayer graphene with multiple dopant concentrations and configurations, as described in ref. [147]. Here, we go beyond simple synthesis to systematically probe the influence of different dopant concentrations and configurations on the optical, electronic, vibrational properties and carrier dynamics of CVD grown bilayer graphene.

We found that the phonon scattering cross-sections, saturable absorption characteristics and relaxation time constants are strongly influenced by the dopant configuration rather than the dopant concentration. While detailed characterization of our

samples is described in ref. [147], a brief overview is presented below for facilitating a comprehensive understanding of the results. The C 1s line in the XPS spectra (Fig. 1 in ref. [147]) for pristine and three N-doped graphene samples labeled S1 (pyrrolic), S2 (graphitic), and S3 (pyridinic; see Methods section and Fig. 1(a)) is upshifted (by ~0.1–0.16 eV) and broadened (by ~0.5 eV), relative to the pristine sample, with a peak maximum ~284.61 eV and a full width at half-maximum ~1 eV. A statistical analysis of N 1s line shape on at least 3 samples confirmed the presence of different configurations for doped N in the graphene lattice: graphitic, pyrrolic and pyridine-like N [148,149]. As detailed in ref. [147], we observed that sample S2 exhibits graphitic dopant configuration while S1 and S3 show additional defects such as vacancies and pentagons in the honeycomb lattice appearing due to pyridinic/pyrrolic substitution. Besides identifying the N bonding configurations, we quantified dopant concentration from the relative photoemission cross-sections for the C 1s and the corresponding N 1s (substitutional doping only) peaks in S1, S2 and S3 to be 0.2, 2.5 and 3.8 at% N, respectively.

The Raman spectrum of pristine graphene (Fig. 7.2) exhibits several sharp features such as the disorder band (*D* band), graphitic band (*G* band) and the *G′* band. Clearly, the intensity of *D* band (located at ~1350 cm^{-1}) relative to the *G* band (located at ~1585 cm^{-1}) is low in pristine samples due to their high crystallinity. Interestingly, samples S1 and S3 also exhibited an additional peak at ~1620 cm^{-1} (known as the *D′* band) [150]. The origin of the *D* and *D′* band is well understood within the framework of double resonance (DR)

where the in-plane transverse or longitudinal optical phonon (iTO/iLO) scattering is conserved respectively by inter-valley or intra-valley defect scattering [151].

Cancado *et al.* [152] reasoned earlier that the *D* band is more intense for arm-chair edges (compared to zig–zag edges) since the defect scattering (needed to conserve the iTO scattering) associated with them can connect two inequivalent *K* and *K′* points (or support inter-valley scattering) in the Brillouin zone. In our samples, non-graphitic dopant configuration (samples S1 and S3) generates pores in the graphene sheets, which contain armchair like edges and consequently result in the increase in *D* band intensity relative to the *G* band intensity. In addition, the *D* band also broadens more in samples S1 and S3 compared to S2 due to the lattice disruption by dopants bonded in the nongraphitic configuration. It is important to note that the above Raman features were prevalent on a millimeter scale in all our samples.

Our CVD grown samples clearly exhibited a four-peaked structure in the G' band (Fig. 7.2) with a dispersion ~85 ± 5 cm^{-1} confirming that the samples are indeed bilayer graphene. The G' band is also a double resonance (DR) process similar to the *D* and *D′* bands, however, in the DR process for the G' band two iTO phonons are involved in inter-valley scattering without the need for defects. We previously showed that the G' band downshifts upon doping graphene with N, as described in ref. [147]. Interestingly, we found that the downshift in G' band is also strongly dependent upon the dopant configuration, i.e., larger downshifts in G' band were observed for samples S3 (~25 cm^{-1})

and S1 (10–15 cm^{-1}) which contained N-dopants in non-graphitic configurations relative to sample S2 (1–2 cm^{-1}). It is expected that the presence of edges in the non-graphitic bonding configuration may renormalize the electron and phonon energies more strongly [151], i.e., changes in Fermi and phonon velocities that dictate the dispersion of Raman modes with respect to excitation energy. Such a renormalization leads to a discernible downshift in the G' band frequency even at low dopant concentrations as seen in sample S1 (cf. Fig 7.2).

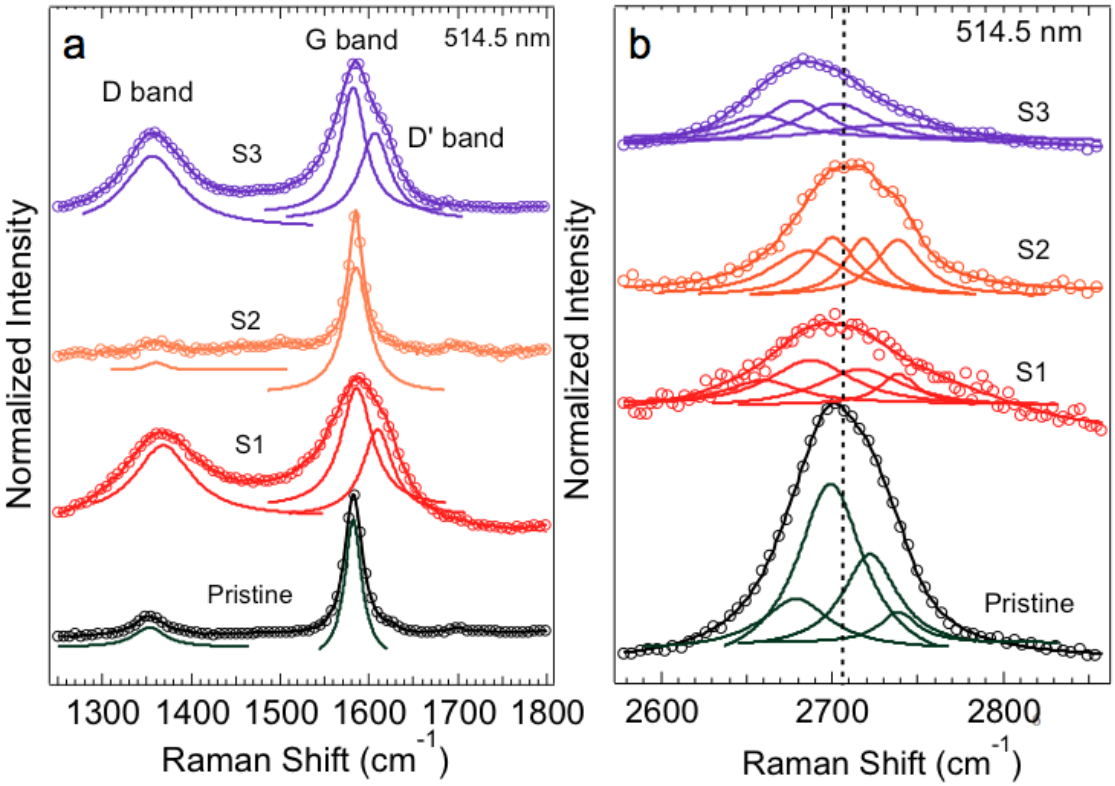


Figure 7.2: Raman spectra for pristine and N doped graphene (S1 – S3) obtained using 514.5 nm excitation. The D and D' bands in panel a) are intense for S1 and S3, and are attributed to N dopants present in the non-graphitic doping configuration (see text).

Notably, the *D* and *G* band intensities for S2 (graphitic doping configuration) are similar to those exhibited by pristine graphene, except for the defect-induced broadening. The electron-phonon energy renormalization upon doping results in a net downshift of the peak position of the G' band for S1and S3 relative to that for pristine and S2.

As discussed next, the above-discussed electronic structure is consistent with our density functional theory calculations. The positive formation energies (>9 eV) for the three-dopant configurations (see Fig. 7.3) obtained from the DFT modeling confirms their stability. The formation energy of graphitic doping was found to be 10.2 eV, which is higher than 9.9 eV for pristine implying that the graphitic phase is not only the most stable among other dopant configurations but interestingly is also more stable than pristine graphene. While the higher stability of graphitic dopants among doped graphene phases may be understood in terms of energetically unfavorable vacancies and dangling bonds present in non-graphitic configurations, its stability over the pristine form may be rationalized as follows. In pristine graphene each C atom has three s bonds with neighboring C atoms and one p bond (sp^2 hybridization), whereas in graphitic dopant configuration, the N atom substituting the C atom possess an extra lone pair of electrons after forming 3s bonds with 3 adjacent C atoms. This extra electron lone pair is in conjugation of the double bond of other C atoms around the N atom (i.e., conjugation between the N lone pair and s and p bonds resulting from sp^2 hybridization of graphene) and is responsible for the electron resonance, which enhances the stability of graphitic dopants slightly above the pristine form. In addition to the three different configurations

discussed in Fig. 7.3, our DFT calculations showed that the porphyrin-type dopants are stable in graphene with a formation energy ~9.75 eV, which is greater than that of pyrrolic dopants. Although porphyrin-type dopants are more stable than pyrrolic, our detailed XPS studies (discussed in ref. [147]) did not detect the presence of this dopant configuration experimentally in samples discussed in this study.

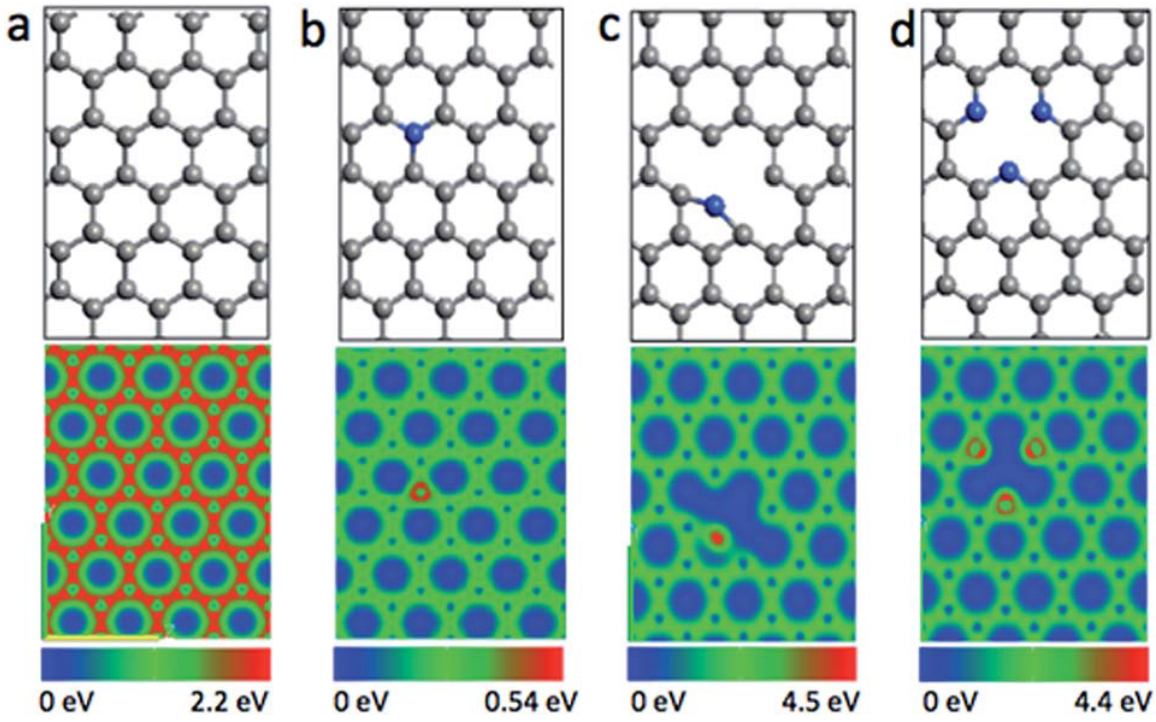


Figure 7.3: The lattice structure (top 4 panels) of pristine (a), graphitic (b), pyridinic (c), and pyrrolic (d) defects in graphene along with their electron density shown in the bottom panels. The energy released on the formation of structure from free atoms for all the configurations was found to be positive (pristine-9.90 eV, graphitic-10.22 eV, pyridinic-9.77 eV, and pyrrolic-9.55 eV) confirming the stability of N doped configurations experimentally observed from XPS and Raman spectroscopy.

The Raman spectrum of graphene contains many rich features (e.g., *D* and G' bands) that are highly sensitive to interand intra-layer defects and interactions. Besides the main D, G, and G' bands, several other Raman modes such as the combination modes and G* mode ~2450 cm^{-1} appear in the spectrum of graphene [112,153,154]. In a Raman process, phonons away from the center of the Brillouin zone (G point) are often not active since the linear momentum of the light is small (~0.002 nm^{-1} for 488 nm excitation) when compared with the Brillouin zone dimension (~13 nm^{-1} for graphene). However, the K-point phonons are still visible in the Raman spectrum of graphene due to its unique continuous energy levels and phonon dispersion relations, which facilitate a high Raman scattering cross-section (Q in eqn (7.1)) through the DR mechanism.

$$Q = \sum_{a,b,c} \frac{M_{fc}M_{cb}M_{ba}M_{ai}}{(E_l - E_{ai} - i\hbar\gamma)(E_l - \hbar\omega - E_{bi} - i\hbar\gamma)(E_l - \hbar\omega - E_{ci} - i\hbar\gamma)} \quad (7.1)$$

In eqn (1), M_{xy} (x, y= a, b, and c) is the matrix element for scattering over the intermediate states *x* and *y*, E_l and E_l- $\hbar\omega$ are the energies of the incoming and outgoing photon, E_{pi} (p= a, b, and c) is the difference in the energy of electronic level *p* and the initial level *i*, and λ is the broadening parameter of the electronic transition between *p* and *i*. Previously, May *et al*. [155] and Araujo *et al*. [154] have independently analyzed the G* band and assigned it to a combination mode containing 2 or more peaks arising from iTO and LA phonons scattering electrons to either the inner or outer side [154] of the

Dirac cones at the K/K'-points. As shown in Fig. 7.4, we clearly observed at least a two-peak structure in the G* band for the pristine samples similar to earlier reports.

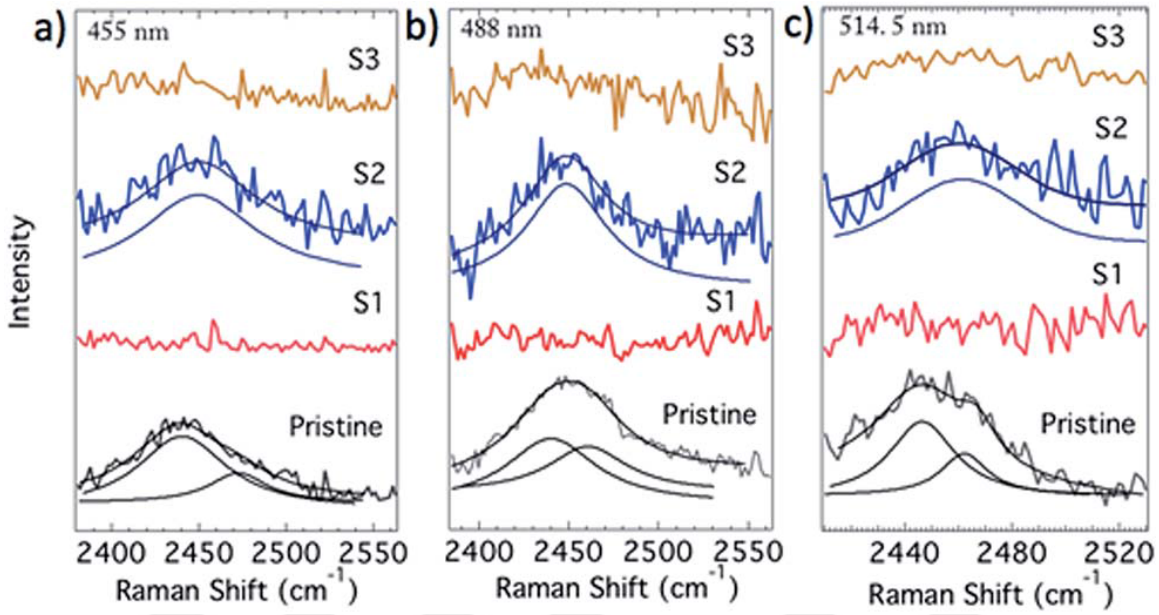


Figure 7.4 (a–c) Raman spectra of CVD grown samples show the presence of two peaks in the G^* band ~2450 cm^{-1} in pristine samples at 3 different Raman excitations. The solid curves below the spectrum are the deconvoluted fits to the experimental data. The G^* band broadens in S2 and disappears in S1 and S3 samples due to defect-induced broadening.

Interestingly, the G^* band vanished completely for samples S1 and S3 while only one peak (as opposed to two peaks in the pristine sample) was found in sample S2 for at least 3 different laser excitations (455, 488, and 514.5 nm). Such an observation may be rationalized as follows. As described in eqn (7.1), the Raman scattering processes are broadened by the parameter γ that originates from electron–phonon and electron–

electron scattering of the photo-excited carriers [156]. A fast scattering rate of photo-excited carriers (or low τ) increases γ. The introduction of dopants results in strong electron-defect scattering that reduces the excited carrier-phonon scattering time from ps to hundreds of fs (an order of magnitude decrease) in samples S1 and S3 (evidenced by results described later in Fig. 7.7) resulting in a high γ or severe broadening of all Raman features. The disappearance of two-peaked structure and the broadening of G^* band in sample S2 may also be attributed to a moderate increase in γ. The non-graphitic doping in S1 and S3 induces defects other than N-dopants such as vacancies or edges, which scatter electrons more efficiently than phonons, possibly resulting in the complete disappearance of the G^* band. Concurring with this scenario, we observed that combination modes (such as iTALO, LOLA, and iTOTA described in ref. [112]) are severely broadened in sample S1 and completely disappeared (similar to the G^* band) in samples S2 and S3 due to defect-induced scattering and increase in γ (Fig. 7.5(a)).

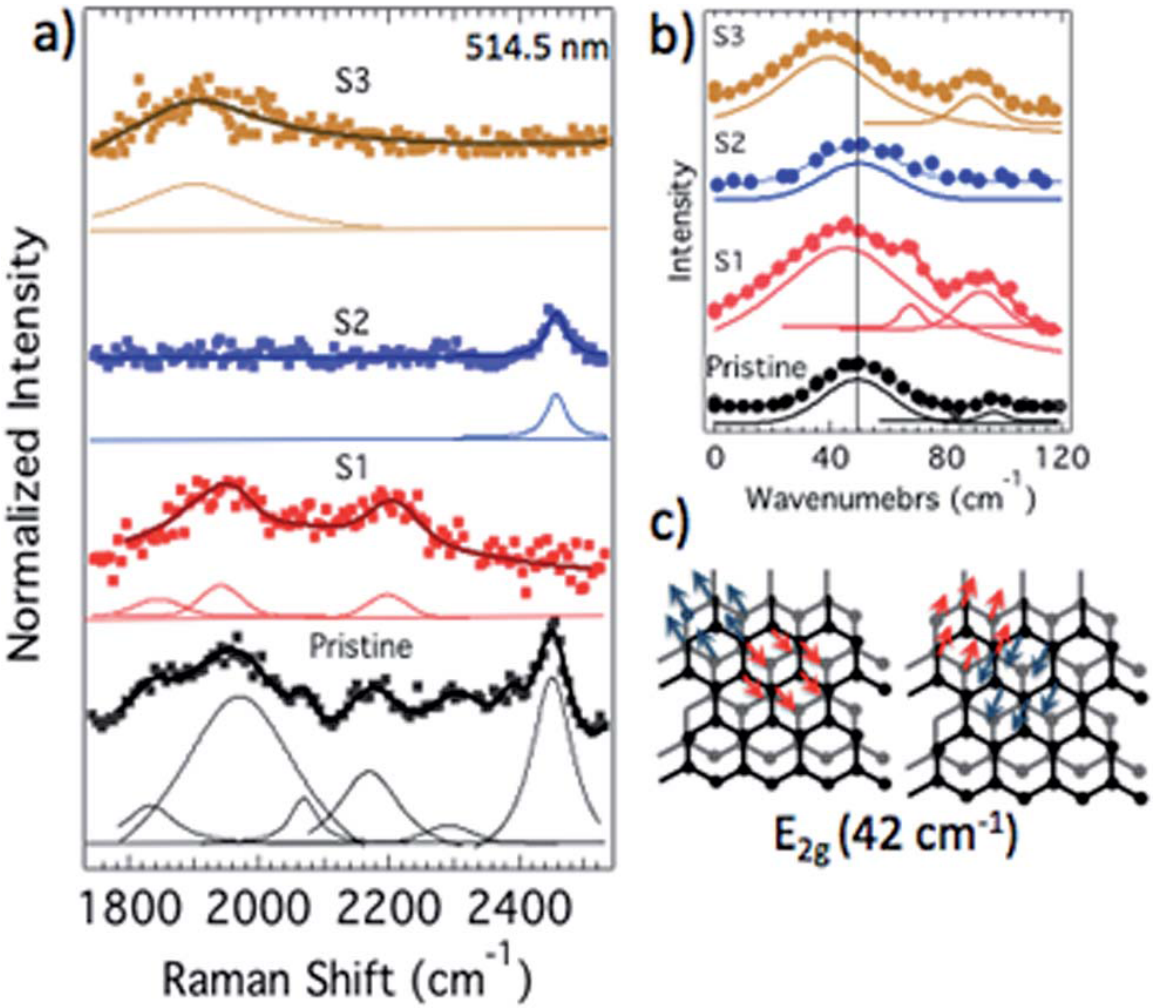


Figure 7.5: (a) The Raman spectra of pristine and N-doped samples showing various combination modes between 1800–2500 cm^{-1}. Clearly, these modes broaden and disappear upon the introduction of dopants due to the increase in inhomogenous broadening and electron defect scattering. The solid curves below each spectrum are the deconvoluted fits. (b) A Fourier transform of time-resolved pump–probe spectrum (discussed later in Fig. 7.7) showing the low-frequency Raman modes in CVD grown graphene. The broad feature ~45 cm^{-1} may be attributed the doubly degenerate (E_{2g}) shear mode shown in (c).

In addition to the linear optical (e.g., π–π* transition) and vibrational properties, we and others previously showed that the nonlinear optical properties of graphene (i.e., saturable absorption) are highly sensitive to the changes in its electronic structure [157,158]. Accordingly, we performed open aperture Z-scan studies of S1–S3 to confirm the dopant-induced changes in the electronic structure of host graphene. As shown in Fig. 7.6 (a) and (b), the nonlinear transmittance (both in the ns and fs regimes) increases with input intensity signaling a saturation of absorption in all samples. Numerical simulations based on nonlinear transmission eqn (7.2) yielded a best fit to the experimental data when a weak two-photon absorption (2PA) component was added to the dominant saturable absorption (SA) within the mathematical model. The pulse propagation equation for such an SA + 2PA type process is given by

$$\frac{dI}{dz'} = -\frac{\alpha_0 I}{1+I/I_s} - \beta I^2 \qquad (7.2)$$

where I is the incident laser intensity, z' is the propagation distance within the sample, α_o is the linear absorption coefficient, I_s is the saturation intensity which characterizes the saturable absorption behavior and β is the 2PA coefficient [157–159]. Clearly, the NLO data in Fig. 7.6 follows a similar trend as that observed in the Raman and XPS data, underscoring the influence of dopant configuration (over dopant concentration) on the optical properties of N-doped graphene.

The β and I_s values [157,158,160–164] obtained from the numerical fits for S1 and S3 (non-graphitic configurations) are higher than to those for S2 (graphitic

configuration) and pristine graphene, indicating that NLO properties are also influenced by the renormalization in the electronic energies. A simple increase in n alone cannot rationalize the deduced increase in β or I_s values since β and I_s of S1 are higher than S2 despite its low N concentration (Fig. 7.6 (c) and (d)). These intriguing, and important, dopant-induced changes in the optical properties of S2 relative to S1 and S3 can be rationalized in terms of the carrier relaxation times through ultrafast degenerate pump–probe (PP) measurements, which we discuss next.

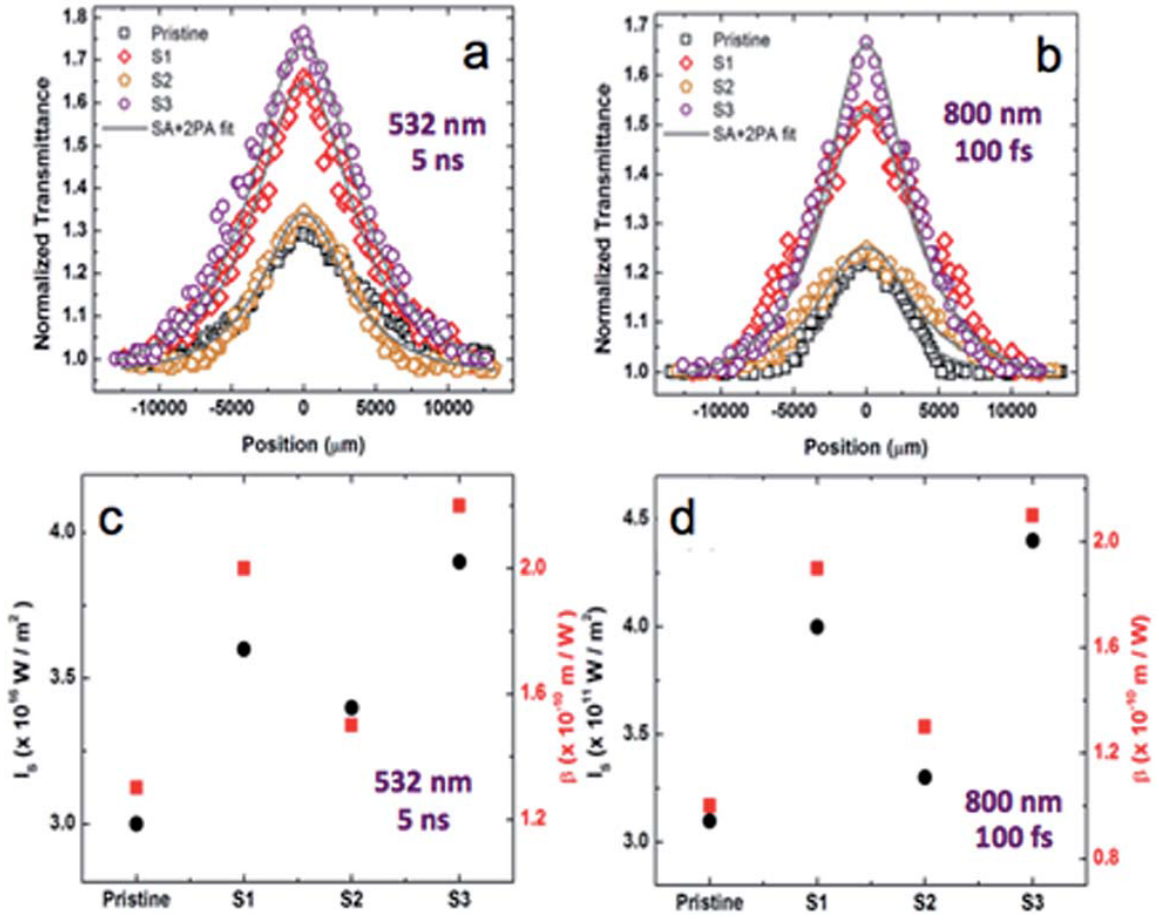


Figure 7.6: Open aperture Z-scan data for pristine graphene, S1, S2 and S3 collected with the (a) ns and (b) fs excitations. The on-axis peak intensity (I_o) is 0.16 GW cm^{-2} and

12.5 TW cm^{-2}, respectively. Solid lines represent theoretical fits to the experimental data obtained from eqn (1) (see text for details). Panels (c) and (d) show the variation of saturation intensity (Is) and the 2PA coefficient (b) obtained from the best fit curves to the Z-scan data in panels (a) and (b). Both I_s and β are higher for the non-graphitic dopant configuration due to the larger defect density arising from pores and arm-chair like edges (cf. Fig. 7.4(a)).

The differential transmittance *(ΔT/T)* was obtained by taking the ratio of the pump-induced change in the probe transmittance *(ΔT)* at a time t after the pump excitation to the probe transmittance *(T)* in the absence of a pump (Fig. 6(a)). The initial response is an incident pulse-width-limited rise in the transmitted signal immediately after the zero delay *(t . 0)*, which eventually decays in an exponential manner. The best fit to the PP data was obtained with a bi-exponentially decaying function, $\Delta T/T = A_1\, exp(-t/\tau_1) + A_2\, exp(-t/\tau_2)$ with two distinct time scales: a fast component (τ_1) corresponding to the intra-band carrier-carrier scattering and a slower component (τ_2) corresponding to carrier-phonon scattering (discussed later in Fig. 7.7 (b). Both $\tau_1$and $\tau_2$values obtained from the best-fitted curves for the samples are tabulated in Table 1. Consistent with our Z-scan measurements (*cf.* Fig. 7.6), the sign of *ΔT/T* signal in Fig. 7.7 is positive and is due to the bleaching of ground state (saturable absorption). As shown in Fig 7.7 (b), under intense photo-excitation a narrow non-equilibrium carrier distribution (akin to a broadened Dirac-delta distribution) is generated in the electron density of states above and below the Fermi level through intra-band and inter-band one-photon

absorption (1PA) and 2PA processes [158]. Such a non-equilibrium carrier population broadens in momentum via inelastic and elastic intra-band carrier–carrier scattering on a timescale of s1 (100–200 fs) and equilibrates to reach a Fermi–Dirac distribution with a temperature much higher than the lattice temperature. The hot carriers further cool down by inter-band carrier–phonon scattering on a timescale of s2 (1–2 ps) and eventually reach a thermal equilibrium with the lattice.[158] In the case of carrier trapping, relaxation times are prolonged up to hundreds of ps to a few ns [158]. Once a steady state is reached between excited carriers and carriers relaxing back to initial states, further absorption of photons within the pulse width is restricted as two photo-excited carriers cannot occupy the same state due to 'Pauli blocking'.

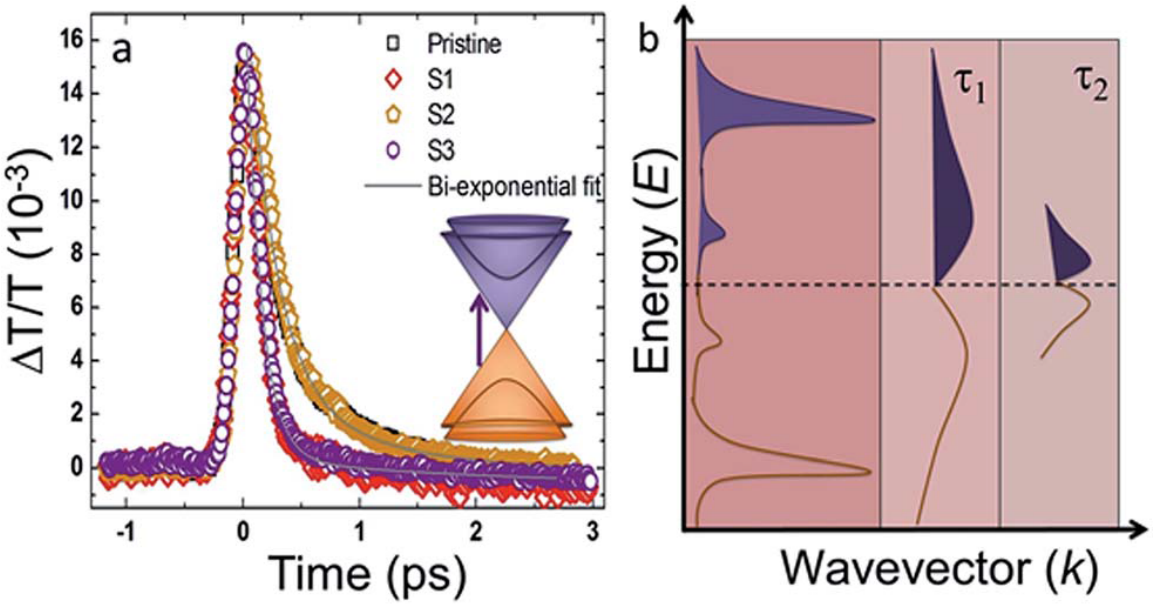


Figure 7.7: (a) Time-resolved differential transmission spectra for pristine graphene and S1–S3 obtained through a degenerate pump–probe method using 70 fs pulses of 780 nm excitation wavelength. Solid lines represent the bi-exponential fits based on carrier–carrier and carrier– phonon scattering time scales (see Table 1). The inset shows the parabolic energy dispersion for bilayer graphene and the arrow indicates excitation of electrons from the valence to the conduction band. (b) Under intense photo-excitation, the non-equilibrium carrier distribution (in the *E–k* space depicted by the parabolic energy dispersion in the inset shown in (a)) results in an initial rise in the transmitted intensity. The carriers (electron and hole distribution shown in blue and orange respectively) equilibrate by carrier–carrier scattering on a timescale τ_1. Subsequently, the carrier thermalization and decay occur through carrier–phonon scattering on a timescale τ_2.

Sample ID	τ_1	τ_2
Pristine	241 fs	2 ps
S1	196 fs	206 fs
S2	232 fs	1.6 ps
S3	168 fs	186 fs

Table 7.1 Carrier relaxation times of both pristine and N-doped graphene obtained from the analysis of time resolved ultrafast pump– probe measurements. Consistent with conclusions drawn from the Raman and NLO data, S2 exhibits similar carrier–carrier (τ_1) and carrier–phonon (τ_2) relaxation times due to its graphitic N-dopant configuration

As shown in Table 1, the carrier–carrier and carrier–phonon relaxation times do not decrease monotonically with increasing N content, akin to the Raman features described in Fig. 7.4 and 7.5 and the saturable absorption intensity in Fig. 7.6(a) and (b).

Clearly, the dopants present in the non-graphitic configurations exhibit much faster relaxation times than to dopants present in S2 with graphitic bonding, or pristine graphene. Indeed, carriers in sample S1 decay much faster (within fs), despite lower N content, due to the presence of extended defects that lead to increased contribution from carrier-defect scattering. Since $L_a(nm) = 2.4 * 10^{-10}\lambda^4(I_G/I_D)$,[112,151,152,154–157] it follows that L_a (and hence the relaxation time) decreases with an increase in the *D* band intensity. Clearly, the non-graphitic dopants present in S1 and S3 lower L_a as they create pores in the honeycomb lattice leading to extended defects (or a high defect-density).

While L_a, derived from empirical results in nano-crystalline graphite [165], represents the amount of disorder given by one-dimensional defects, L_d or average distance between point defects in single-layer graphene may be obtained as $L^2_d(\mathrm{nm}) = 1.8*10^{-9}\lambda^4(I_G/I_D)$. Since both L_a and L_d vary inversely with D band intensity, carrier relaxation times decrease significantly for S1 and S3 (non-graphitic) compared to S2 and pristine samples. In this context, L_a is more appropriate than L_d for our samples due to their bilayer character and the nature of extended defects in S1 and S3 (e.g., pores and arm-chair like edge). Considering pristine graphene as a two-dimensional electron gas (2DEG), we can approximate the Fermi wave vector $k_F \sim (2\pi n)^{1/2}$ with an average carrier density $n \sim 10^{12}$ cm^{-2}. In other words, the carriers in pristine graphene may be considered to have a wavelength ~25 nm. The I_G/I_D ratios from the Raman data in Fig. 7.2 yield L_a>100 nm for pristine (106 nm) and S2 (101 nm) samples, which is at least 4 times the carrier wavelength (25 nm). However, S1 and S3 exhibit a much shorter L_a (33 and 25 nm, respectively), which is comparable to the carrier wavelength, and consequently support enhanced scattering of carriers (or faster decay times). Considering that μ is directly proportional to τ, it is then expected that μ in the case of S2 is not significantly different from that in pristine graphene, despite the presence of dopants in S2 (since it does not significantly alter L_a). Such a dopant configuration is advantageous since it increases the carrier concentration and upshifts the Fermi level without compromising the carrier mobility in doped graphene. Returning to the saturable absorption behavior of N-doped graphene (cf. Fig. 7.6), Dawlaty et al. have earlier reported that τ_2 in pristine epitaxial graphene decreases concomitantly with L_a, concurring with our present

observation of lower lifetimes for non-graphitic substitution (S1 and S3). The saturation carrier density (N_s) in graphene could be estimated using a simplified approximation given by Bao et al. as $N_s = \alpha I\tau/\hbar\omega$ where α is the absorption coefficient, $\hbar$ is the reduced Planck's constant and ω is the excitation frequency [166]. Chemla et al. argued that in the case of 2-DEG, absorption saturation occurs when the photo-generated carrier density is about one charge carrier per exciton volume $4\pi a_o^3/3$where a_0 is the Bohr radius [167].

Therefore saturation intensity can be approximated as $I_s = 3\hbar\omega/4\pi a_0^3\alpha\tau$ [163]. It now follows that for a given excitation, I_s is solely determined by τ through an inverse relation. Thus the variation in I_s with dopant configuration for both fs and ns excitation regimes shown in Fig. 7.6(c) and (d) can be explained using the effect of defects on the carrier relaxation times.

Returning to Fig. 7.5(b), the broadening of Raman features concurs with the carrier relaxation times derived from the data presented in Fig. 7.7. In addition to providing the relaxation times, the Fourier transform (FT) of excited carrier decay, shown in Fig. 7.5(b), contains information pertaining to low-wavenumber phonons. The presence of the Raman excitation line at 0 cm^{-1} often overwhelms the low-frequency phonon signals in Raman spectroscopy. Recently, Tan *et al.* [168] uncovered a doubly degenerate (Fig. 7.5(c)) low-wavenumber shear mode (~45 cm^{-1}) in multilayer graphene using Raman spectroscopy. As shown in Fig. 7.5(b), we observed a peak in the low-

frequency data ~45 cm^{-1} in the FT-spectra (derived from Fig. 7.7(a)), which could plausibly be attributed to the shear mode in our bilayer samples. Not surprisingly, we found that this mode broadened in all the doped samples akin to other features (cf. Fig. 7.5 and 7.6) observed directly in the Raman spectrum due to changes in carrier relaxation times. Additional features observed above 45 cm^{-1} may be Raman inactive acoustic phonons away from the Γ-point and warrant further investigation. Lastly, juxtaposing DFT, Raman, XPS, pump–probe and non-linear optical spectroscopic measurements on N-doped graphene, it could be surmised that both dopant configuration and density play a critical role in determining the properties of graphene. Particularly, an increase in the density of non-graphitic nitrogen dopants is expected to decrease the coherence length L_a, much more rapidly than graphitic dopants, due to the formation of other accompanying defects such as vacancies or pentagons. This increase in non-graphitic N-dopant density will lead to: (i) a more pronounced decrease in the electronic mobility, compared to graphitic dopants, due to increased defect scattering, (ii) increase the electronic density of states near the Fermi level, and (iii) the appearance of D and D'-bands ~1350 cm^{-1} and ~1620 cm^{-1}.

7.4 Conclusions

In summary, we investigated the influence of substitutional N-doping on the electronic, vibrational, and optical properties of CVD grown bi-layer graphene. Our DFT calculations showed that all N-dopant configurations are stable with a positive formation

energy. Our XPS measurements indicated that N can be controllably doped in pyridinic, pyrrolic, and graphitic configurations. Interestingly, the *D*-band intensity increased significantly only when the N-dopants are substituted in non-graphitic configurations since they create pores with armchair edges in the graphene lattice. Furthermore, the Raman G' band frequency was observed to downshift due to the electronphonon energy renormalization near dopant sites. The G^*, combination, and low-frequency modes (derived from pump– probe data) broadened or disappeared in the Raman spectrum of doped samples due to decreased scattering rates. In the nonlinear regime, the 2PA coefficient and saturation intensity were higher for non-graphitic dopant configuration compared to graphitic configuration, consistent with the Raman scattering data. Most importantly, time-resolved pump–probe spectroscopy studies clearly showed that non-graphitic dopants reduce scattering times of electrons due to a decrease in the crystal coherent length. Lastly, our results imply that N-dopants when substituted in a graphitic configuration yields n-type graphene with little or no deterioration in the electron mobility.

CHAPTER EIGHT

SUMMARY AND FUTURE WORK

Understanding of nanomaterial properties is important to develop future technologies. Introducing defects on nanomaterials changes their physical, chemical, electrical properties *etc.* and controlling these defects are challenge. Carbon nanomaterials have unique properties and this dissertation focused on defects introduced carbon nanotubes and graphene.

In chapter 2, helically coiled CNTs foam showed promising energy dissipation performance but there are some challenges. One of the challenges is controlling the coil diameter and coil pitch. Coil diameter and pitch will affect the HCNT foam performance. The other challenge is uniform growth of HCNT. Cost is also one of the challenges. For HCNT growth, expensive chemicals are used and cost effective new methods need to be developed.

In chapter 3, bucky aerogel foams was introduced. A new CNT foam preparation method was developed and it was shown that this method is time saving and cost effective. Being lightweight, easy to prepare and time saving, it has a potential various application fields. The next step for this project is scalable production of BAG foam.

Chapter 4 focused on nano-composites. We showed that polymer modified HCNTs or MWCNTs demonstrate a clear example of how two disparate materials can be combined to exploit material properties. The use of highly conductive, three dimensional scaffolds achieved by the carbon nanomaterials within the paper electrode provides new possibilities for low cost energy storage materials, such as solution processable redox polymers.

In chapter 5, we present a scalable roll-to-roll (R2R) spray coating process for synthesizing randomly oriented multi-walled carbon nanotubes electrodes on Al foils. Our cost analysis shows that the R2R spray coating process can produce supercapacitors with 10 times the energy density of conventional activated carbon devices at ~17% lower cost. In future studies, we will focus on a CNT/polymer composite to make electrodes and increase the performance of the supercapacitor devices.

In chapter 6, we have indicated a methodology for both increasing and decreasing the electrochemical capacitance of FLG-based nanographites through a combination of argon and hydrogen-based plasma processing. In addition to the utility for charge storage, our work contributes to understanding and controlling the charge storage characteristics.

In the final chapter, the influence of substitutional N-doping on the electronic, vibrational, and optical properties of CVD grown bi-layer graphene was investigated. Our results imply that N-dopants when substituted in a graphitic configuration yield n-type

graphene with little or no deterioration in the electron mobility. In this study we have investigated nitrogen doped graphene. We will investigate other atoms, such as boron, sulfur *etc.* doping effects on graphene.

APPENDICES

Appendix A

We performed synchrotron X-ray scattering and mass attenuation measurements to nondestructively quantify the density and alignment within HCNT foams. A beam energy of 10 keV was selected with a Mo/B4 C double multilayer monochromator, and the height of the beamspot was less than 300 μm at the sample with a measured flux of 10^{12} photons sec^{-1}. The HCNT sample was mounted on a motorized stage that enables 1) tilt alignment to make the sample's Si substrate parallel to the X-ray beam as well as 2) spatial mapping of the structural characteristics of the sample along its height.

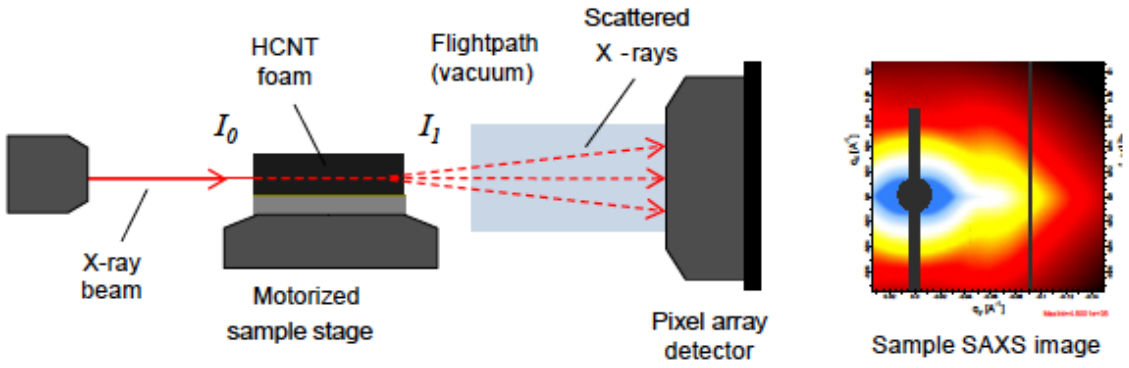


Figure Appendix A 1: Schematic side view of the experimental setup for X-ray characterization with a representative SAXS image collected from our HCNT foams. The x-z-α stage enables spatial mapping and alignment of the HCNT to the X-ray beam, and the scattered X-rays are collected on a Pilatus 1M pixel detector.

We monitored the X-ray intensity upstream (I_0) and downstream (I_1) of the sample by measuring ion current at the locations denoted in the schematic. These values were used to calculate the mass density of the sample based on the Beer-Lambert law [46],

$$\rho_{CNT} = \frac{ln\left(I_0/I_1\right)}{t(\mu/\rho)}$$

where ρ_{CNT} is the HCNT volumetric mass density, t is the path-length through the HCNT, and (μ/ρ) is the mass attenuation coefficient. Values for (μ/ρ) are tabulated by NIST as a function of element and X-ray energy.

In addition to measuring the X-ray attenuation, we also quantified the average CNT alignment from the anisotropy of small-angle X-ray scattering (SAXS) patterns. Using the distribution of scattered intensity about the azimuthal angle φ, we calculated the Hermans orientation factor [47]

$$f = \frac{1}{2}(3\langle cos^2\varphi\rangle - 1)$$

Here, f equals 1 for perfectly aligned CNTs and 0 for random order (no alignment), and

$$\langle cos^2\varphi\rangle = \frac{\int_0^{\pi/2} d\varphi I(\varphi) sin\varphi cos^2\varphi}{\int_0^{\pi/2} d\varphi I(\varphi) sin\varphi}$$

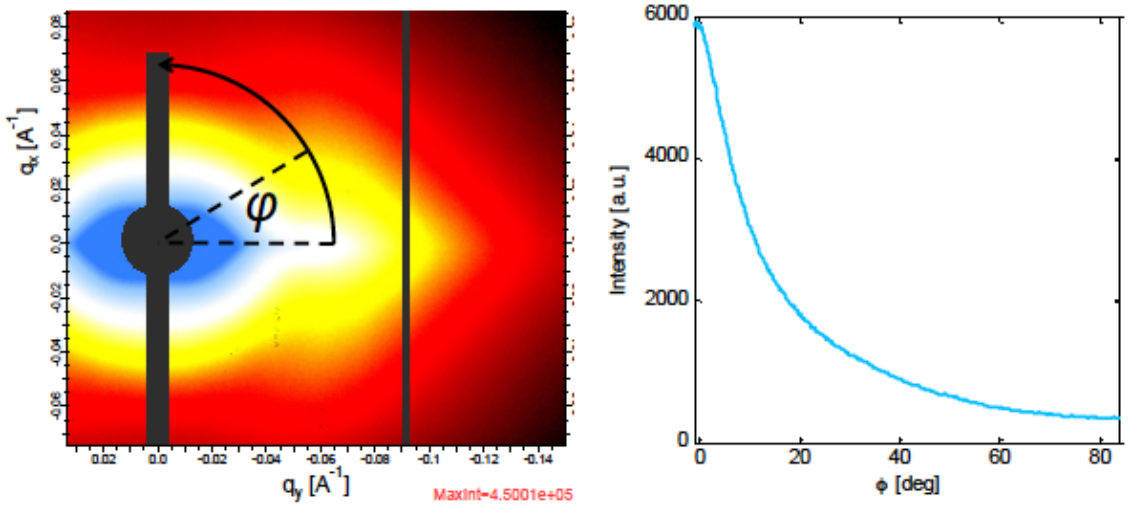


Figure Appendix A 2: Schematic illustration that demonstrates the azimuthal integration we perform on SAXS images to extract the Herman's orientation factor. The annulus of the azimuthal scan about φ is defined by ±5 pixels from the CNT form factor scattering peak located near q = 0.05- 0.07 $Å^{-1}$. We only use one half of the SAXS image because HCNT alignment is isotropic in the plane of the catalyst substrate (Si), so the SAXS pattern is vertically symmetric.

Appendix B

Calculation of the space charge capacitance (C_{SC}) and the quantum capacitance (C_Q)

The plasma processing of the few layer graphene (FLG) samples was considered to increase the carrier density of the graphene, giving rise to an increase in measured capacitance from the CV measurements. In order to analytically model this increase, it was necessary to consider the constituent capacitances (all normalized per unit area), i.e., the space-charge capacitance: Csc, and the quantum capacitance: CQ, in terms of an equivalent carrier density.

The measurement for the FLG represents accumulated responses from each of the individual layers. A major influence in accounting for the charge densities of the individual layers is the screening, starting from the layer closest to the electrolyte, which shields the internal layers of the FLG from the charges in the electrolyte and implies a diminishing electrical potential from the outer to the inner layers of the FLG. Consequently, the carrier density in the single layer of graphene closest to the electrolyte is considered to be: $n_{2D,0}$. The carrier density of each subsequent layer would typically be scaled down by an exponential factor ~ $exp\ (-x/\lambda)$, where λ is an appropriate screening length, e.g., a Debye length or a Thomas-Fermi screening length (see Appendix A. b).

The need to consider various types of λ as well as the possibility of nonlinear screening in FLG systems has been previously reported.

a. Estimating the carrier density in the layer, closest to the electrolyte: $n_{2d,0}$ and the E_F

A quantitative discussion of $n_{2D,0}$ requires derivation starting from the energy (E) dependent density of states: D(E), of graphene. While the inter-layer interaction in FLG has been implicated in a nonlinear energy dispersion, e.g., a hyperbolic dispersion for bilayer graphene, we approximate that in the vicinity of the Fermi energy (E_F), a linear energy dispersion relation of the form: $E = \hbar v_F k$, where $\hbar$ is the reduced Planck constant (=1.05 x 10^{-34}Js), v_F is the Fermi velocity - typically in the range of c/300, where c is the velocity of light, and k as the wavevector, could be considered to gain useful insights. Consequently, the two-dimensional DOS would be:

$$D(E)dE = \frac{4}{(2\pi)^2} 2\pi k\, dk \Longrightarrow D(E) = \frac{2}{\pi} \frac{E}{(\hbar v_F)^2} \quad \text{(B1)}$$

In our analyses, the v_F has been determined from the Raman analysis (see Fig 6.4(b) in the chapter 6), and k refers to the wave-vector. We calculate $n_{2D,0}$ from:

$$n_{2D,0} = \int_0^{E_F} f(E)D(E)dE = \int_0^{E_F} D(E)dE = \frac{1}{\pi} \frac{1}{(\hbar v_F)^2} E_F^2 \quad \text{(B2)}$$

where *f (E)* is the Fermi-Dirac function, and is assumed to be unity for the far right hand side of the above relation. Such an assumption is valid if the Fermi energy (E_F) of the first layer is more than $3k_BT$ away from the Dirac point (denoted by $E = 0$). Indeed, in line with estimates of $n_{2D,0}$ of ~ 5 x 10^{12} cm^{-2}, in practical graphene and graphite, the E_F is of the order of 0.25 eV, which is much greater than ~ 78 meV (=$3k_BT$ at 300 K: room temperature, at which the experiments were done).

b. Choice of appropriate screening length and the estimation of the space charge capacitance: C_{SC}

Through the use of Maxwell's equation for the change in the potential ($\Delta\varphi$), of the form: $\nabla^2(\Delta\varphi) = -\Delta\rho/\varepsilon$, where $\Delta\rho$, is the change in the charge density (= $e\,dn$), with e as the unit of elementary electronic charge due to the change in the number of contributing carriers *dn* and ε being the dielectric permittivity of the graphene (=5.7 ε_0) with ε_0 as the vacuum permittivity (=8.854 x 10^{-12} C^2/Nm^2), one may derive an effective screening length (λ), assuming that φ variesas exp (-x/λ). Consequently, the solution of the Maxwell equation yields:

$$\lambda = \sqrt{\frac{\varepsilon}{e^2}\left(\frac{dE}{dn}\right)} \qquad with\ dE = e\Delta\phi \tag{B3}$$

A Boltzmann approximation, whereby the volumetric charge density: $n = n\ exp\ (E/k_BT)$ and $dn/dE = n/k_BT$, yields the Debye screening length (λ_D). However, in graphene, with

$n_{2D,0} \sim E_F^2$ the (dn/dE) evaluated at $E=E_F$ is equal to ($2n/E_F$) and results in an alternative screening length of the Thomas-Fermi form: λ_{TF}.

$$\lambda_{TF} = \sqrt{\frac{\varepsilon}{e^2}\frac{E_F}{2n}}, \quad with\ C_{SC} = \frac{\varepsilon}{\lambda_{TF}} \tag{B4}$$

where n is set to be equal to $(n_{2D,0})^{3/2}$. Consequently, the C_{SC} is estimated to ε/λ_{TF}.

c. Estimation of the quantum capacitance: C_Q

The implication of the λ_{TF} is that the charge on any subsequent (say, l^{th}) layer (counted from the outermost graphene layer, facing the electrolyte, with carrier concentration: $n_{2D,0}$ into the current collector) would be:

$$n_{2D,l} = n_{2D,0}\ exp\ (-lx/\lambda_{TF}) \tag{B5a}$$

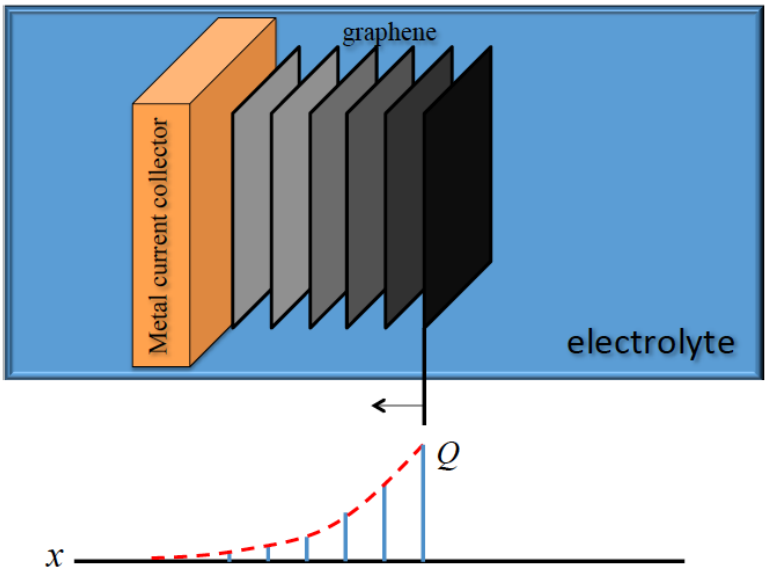


Figure B1: While the constituent charge (Q) in the individual layers of the FLG is discrete, the carrier concentration from the outermost layer into the current collector was modeled through a continuous exponential decay.

The "x" was obtained from the experimentally determined spacing between the layers, through Atomic Force Microscopy (AFM) measurements and was estimated to be ~ 1 nm: Fig. 6.2.

Schematically, the magnitude of the charge in the layers of our FLG films would be as indicated in Fig A1. The sum of the net discrete charge on the individual layers, i.e., $\sum_{i=0}^{N} n_{2D,i}$ would contribute to the quantum capacitance, through:

$$C_Q = \frac{d\left(=e\sum_{i=0}^{N} n_{2D,i}\right)}{dV} = e^2 D(E_F) \qquad \text{(B 5b)}$$

d. The variation of $n_{2D,0}$ for fitting the experimental values to C_Q and C_{SC}

For fitting the experimental values of the experimentally measured capacitance (C_{meas}) to C_Q and C_{SC}, we varied n_{2D0} for each plasma power until the combined series capacitances, estimated from Eqns. B (4) and (5) match the experimental values. It is found that the values of n_{2D0} begin at 4.5 x 10^{12}/cm^2, which is in good agreement with contemporary literature on carrier concentrations in intrinsic graphene as well as through interpolation from bulk graphite.

Estimation of the charge-correlation length: L_d

We have noted a charge correlation length: $L_d \sim 1\ n_{2D,0}$ as noted in Table I, which may be

understood as the average distance between the charged defects (that could have arisen due to the plasma induced charges) that contribute to the C_Q as well as the C_{SC}. It was observed through simulations, that with an applied electrode bias (~ -100 V) and an ion density of the order of 10^{11} /cm^3, the average ion penetration depth would be ~ 0.8 nm, which implies that only the first layer of the FLG would be affected through the plasma processing. Consequently, only the $n_{2d,0}$ is being considered for the L_d.

e. XPS (x-ray photoelectron spectroscopy) analysis of samples subject to argon and hydrogen plasma processing treatment

Through a preliminary XPS study, we have found that there is very little evidence of the contribution of the surface functional groups, and we have also safely ruled out any substantial contribution to the net capacitance.

Previous plasma treatment work, involving, for example, the treatment of activated fibers with oxygen plasma, has found the substantial presence of quinone groups (involving C=O bonds), that may contribute to additional redox capacitance. To circumvent such complications, we have initially considered only *Ar* based plasma, specifically chosen due to the inherently simple plasma chemistry (where only *Ar*+ ions are involved) and avoids quinone group formation. Consequently, in our data/study, there are absolutely no redox capacitance associated phenomena (as there is no associated peaks in the CV scan): see Fig. 6.3(a).

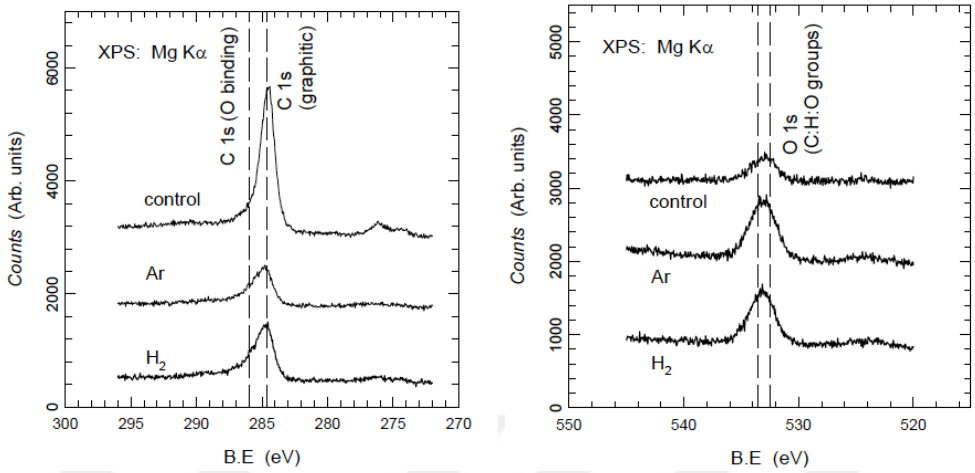


Figure B2: (a) Carbon associated peaks, indicating the pristine graphene – control, argon irradiated FLG – Ar, which was subsequently treated with hydrogen plasma – H_2. There is no evidence of quinone functionality (no peak at 287.6 eV) in the Ar and the H_2 plasma modified samples. (b) The increased oxygen content (as seen through the peak at ~ 532.4 eV in the Ar and the H_2 samples) is indicative of saturated C-O bonds. Additionally, while XPS analyses on the Ar plasma irradiated samples did indicate an enhanced oxygen content, there was absolutely no evidence of quinone functionality (C=O related peaks). The increased oxygen content may have occurred due to exposure to ambient and it was noted that the oxygen is bound up in a C-O saturated bond and not in a unsaturated C=O configuration.

We also note from the XPS measurements before and after the hydrogen plasma treatment (Fig. B2) that the oxygen content seems to have been reduced due to the treatment – see Fig. B2(b). A concomitant increase (/decrease) of the C 1s (/O 1s) peak intensity was observed due to the hydrogen plasma treatment, which indicates the partial effectiveness of the hydrogen treatment, as noted originally.

APPENDIX C

List of abbreviations

1. AC: Armchair
2. ACN: Acetonitrile
3. AFM: Atomic force microscopy
4. BAG: Bucky-aerogel
5. BBO: Beta-barium borate
6. BMIM][BF_4]: 1-Butyl-3-methylimidazolium tatrafluoroborate
7. CF: Carbon fiber
8. CNT: Carbon nanotube
9. CV: Cyclic voltammetry
10. CVD: Chemical vapor deposition
11. DFT: Density functional theory
12. DOS: Density of States
13. DMF: Dimethylformamide
14. EC: Electrochemical
15. ECP: Electro-active conducting polymer
16. EDLC: Electrochemical double layer capacitance
17. FLG: Few layer graphene
18. HCNT: Helical carbon nanotube
19. HRTEM: High resolution transmission electron microscope
20. HOPG: Highly oriented pyrolytic graphite
21. MWCNT: Multi walled carbon nanotube
22. NCNT: Nitrogen doped carbon nanotube
23. NHE: Normal hydrogen electrode
24. NLO: Nonlinear optic
25. R2R: roll-to-roll
26. PAO: Pseudo atomic orbital
27. PCNT1: Pristine carbon nanotube type 1
28. PCNT2: Pristine carbon nanotube type 2
29. PECVD: Plasma enhanced chemical vapor desposition
30. SAXS: small-angle X-ray scattering
31. SDS: Sodium dodecyl sulfonate
32. SEM: Scanning electron microscope
33. SLS: Sodium lignosulfinate
34. SWCNT: Single walled carbon nanotube
35. TBAHFP: Tetrabutylammonium hexafl uorophosphate

36. $TEABF_4$: tetraethylammonium tetrafluoroborate
37. TGA: Thermal gravimetric analysis
38. VACNT: Vertically aligned carbon nanotube
39. XPS: X-ray photoelectron spectroscopy
40. ZZ: Zigzag

REFERENCES

[1] R.W. Siegel, in:, G.L. Trigg (Ed.), Encycl. Appl. Phys., VCH, Weinheim, 1994, pp. 1–27.

[2] K. Lingam, R. Podila, H. Qian, S. Serkiz, A.M. Rao, Adv. Funct. Mater. 23 (2013) 5062.

[3] W. Wang, K. Yang, J. Gaillard, P.R. Bandaru, a. M. Rao, Adv. Mater. 20 (2008) 179.

[4] F. Yavari, Z. Chen, A. V Thomas, W. Ren, H.-M. Cheng, N. Koratkar, Sci. Rep. 1 (2011) 166.

[5] M. Karakaya, D. Saini, R. Podila, M.J. Skove, A.M. Rao, R. Thevamaran, C. Daraio, Adv. Eng. Mater. (2014) n/a.

[6] Z.-S. Wu, K. Parvez, X. Feng, K. Müllen, Nat. Commun. 4 (2013) 2487.

[7] S. Iijima, Nature 354 (1991) 56.

[8] D. Qian, G.J. Wagner, W.K. Liu, M.-F. Yu, R.S. Ruoff, Appl. Mech. Rev. 55 (2002) 495.

[9] R. Saito, G. Dresselhaus, M.S. Dresselhaus, Physical Properties of Carbon Nanotubes, Imperial College Press, London, 1998.

[10] N. Murata, J. Haruyama, J. Reppert, A.M. Rao, T. Koretsune, S. Saito, M. Matsudaira, Y. Yagi, Phys. Rev. Lett. 101 (2008) 027002.

[11] Y. Murakami, Chem. Phys. Lett. 385 (2004) 298.

[12] T. Yamada, T. Namai, K. Hata, D.N. Futaba, K. Mizuno, J. Fan, M. Yudasaka, M. Yumura, S. Iijima, Nat. Nanotechnol. 1 (2006) 131.

[13] A.J. Hart, A.H. Slocum, L. Royer, Carbon N. Y. 44 (2006) 348.

[14] R. Andrews, D. Jacques, A.M. Rao, F. Derbyshire, D. Qian, X. Fan, E.C. Dickey, J. Chen, Chem. Phys. Lett. 303 (1999) 467.

[15] K.R. Atkinson, S.C. Hawkins, C. Huynh, C. Skourtis, J. Dai, M. Zhang, S. Fang, A.A. Zakhidov, S.B. Lee, A.E. Aliev, C.D. Williams, R.H. Baughman, Phys. B Condens. Matter 394 (2007) 339.

[16] E. Polsen, M. Bedewy, E.R. Meshot, A. Tawfick, A.J. Hart, in:, ASME 2011 Int. Mech. Eng. Congr. Expo., Denver, CO, 2011.

[17] M.R. Arcila-Velez, J. Zhu, A. Childress, M. Karakaya, R. Podila, A.M. Rao, M.E. Roberts, Nano Energy 8 (2014) 9.

[18] L. Lattanzi, R. Thevamaran, L. De Nardo, C. Daraio, Adv. Eng. Mater. (2015) n/a.

[19] A. Shaikjee, N.J. Coville, J. Adv. Res. 3 (2012) 195.

[20] P.R. Bandaru, C. Daraio, K. Yang, A.M. Rao, J. Appl. Phys. 101 (2007) 094307.

[21] M. Zhang, J. Li, Mater. Today 12 (2009) 12.

[22] P.R. Bandaru, C. Daraio, S. Jin, A.M. Rao, Nat. Mater. 4 (2005) 663.

[23] P.G. Collins, H. Bando, A. Zettl, Nanotechnology 9 (1998) 153.

[24] A. Jorio, G. Dresselhaus, M.S. Dresselhaus, eds., Carbon Nanotubes, Springer Berlin Heidelberg, Berlin, Heidelberg, 2008.

[25] J.W. Jang, C.E. Lee, S.C. Lyu, T.J. Lee, C.J. Lee, Appl. Phys. Lett. 84 (2004) 2877.

[26] B. Sadanadan, T. Savage, S. Bhattacharya, T.M. Tritt, A. Cassell, M. Meyyappan, Z.R. Dai, Z.L. Wang, R. Zidan, A.M. Rao, J. Nanosci. Nanotechnol. 3 (2003) 99.

[27] X.B. Zhang, X.F. Zhang, D. Bernaerts, G. van Tendeloo, S. Amelinckx, J. van Landuyt, V. Ivanov, J.B. Nagy, P. Lambin, A.A. Lucas, Europhys. Lett. 27 (1994) 141.

[28] C.-J. Su, D. W. Hwang, S.-H. Lin, B.-Y. Jin, L.-P. Hwang, PhysChemComm 5 (2002) 34.

[29] V. Bajpai, L. Dai, T. Ohashi, J. Am. Chem. Soc. 126 (2004) 5070.

[30] T. Hayashida, L. Pan, Y. Nakayama, Phys. B Condens. Matter 323 (2002) 352.

[31] A. Volodin, D. Buntinx, M. Ahlskog, A. Fonseca, J.B. Nagy, C. Van Haesendonck, Nano Lett. 4 (2004) 1775.

[32] X. LI, K. LAU, Y. YIN, Compos. Sci. Technol. 68 (2008) 2876.

[33] K. Lau, M. Lu, K. Liao, Compos. Part A Appl. Sci. Manuf. 37 (2006) 1837.

[34] R.B. Rakhi, W. Chen, H.N. Alshareef, J. Mater. Chem. 22 (2012) 5177.

[35] A. Leela Mohana Reddy, R.I. Jafri, N. Jha, S. Ramaprabhu, P.M. Ajayan, J. Mater. Chem. 21 (2011) 16103.

[36] L. Pan, T. Hayashida, M. Zhang, Y. Nakayama, Jpn. J. Appl. Phys. 40 (2001) L235.

[37] S.H. Park, P. Theilmann, K. Yang, A.M. Rao, P.R. Bandaru, Appl. Phys. Lett. 96 (2010) 043115.

[38] C. Daraio, V.F. Nesterenko, S. Jin, W. Wang, A.M. Rao, J. Appl. Phys. 100 (2006) 064309.

[39] A. Cao, P.L. Dickrell, W.G. Sawyer, M.N. Ghasemi-Nejhad, P.M. Ajayan, Science 310 (2005) 1307.

[40] R. Thevamaran, E.R. Meshot, C. Daraio, Carbon N. Y. 84 (2015) 390.

[41] K.T. Lau, M. Lu, D. Hui, Compos. Part B Eng. 37 (2006) 437.

[42] X. Chen, S. Zhang, D. a. Dikin, W. Ding, R.S. Ruoff, L. Pan, Y. Nakayama, Nano Lett. 3 (2003) 1299.

[43] V.R. Coluci, A.F. Fonseca, D.S. Galvão, C. Daraio, Phys. Rev. Lett. 100 (2008) 086807.

[44] R. Thevamaran, C. Daraio, Exp. Mech. 54 (2014) 1319.

[45] R. Di Giacomo, B. Maresca, A. Porta, P. Sabatino, G. Carapella, H.-C. Neitzert, IEEE Trans. Nanotechnol. 12 (2013) 111.

[46] M. Bedewy, E.R. Meshot, M.J. Reinker, A.J. Hart, ACS Nano 5 (2011) 8974.

[47] E.R. Meshot, A.J. Hart, Appl. Phys. Lett. 92 (2008) 113107.

[48] B.N. Wang, R.D. Bennett, E. Verploegen, A.J. Hart, R.E. Cohen, J. Phys. Chem. C 111 (2007) 5859.

[49] M.F. Gibson, Lorna J., Ashby, Cellular Solids, Cambridge University Press, n.d.

[50] J. Suhr, P. Victor, L. Ci, S. Sreekala, X. Zhang, O. Nalamasu, P.M. Ajayan, Nat. Nanotechnol. 2 (2007) 417.

[51] J.R. Raney, A. Misra, C. Daraio, Carbon N. Y. 49 (2011) 3631.

[52] O. Yaglioglu, No Title, Massachusetts Institute of Technology, 2007.

[53] S.B. Hutchens, L.J. Hall, J.R. Greer, Adv. Funct. Mater. 20 (2010) 2338.

[54] J.R. Raney, F. Fraternali, C. Daraio, Nanotechnology 24 (2013) 255707.

[55] A.E. Aliev, J. Oh, M.E. Kozlov, A.A. Kuznetsov, S. Fang, A.F. Fonseca, R. Ovalle, M.D. Lima, M.H. Haque, Y.N. Gartstein, M. Zhang, A.A. Zakhidov, R.H. Baughman, Science 323 (2009) 1575.

[56] T.W. Hamann, A.B.F. Martinson, J.W. Elam, M.J. Pellin, J.T. Hupp, Adv. Mater. 20 (2008) 1560.

[57] J.T. Korhonen, P. Hiekkataipale, J. Malm, M. Karppinen, O. Ikkala, R.H.A. Ras, ACS Nano 5 (2011) 1967.

[58] L. Cremaldi, D.A. Sanders, P. Sonnek, D.J. Summers, J. Reidy, IEEE Trans. Nucl. Sci. 56 (2009) 1475.

[59] G.-R. Li, Z.-P. Feng, Y.-N. Ou, D. Wu, R. Fu, Y.-X. Tong, Langmuir 26 (2010) 2209.

[60] C. Moreno-Castilla, F.J. Maldonado-Hódar, Carbon N. Y. 43 (2005) 455.

[61] M. Moner-Girona, A. Roig, E. Molins, J. Llibre, J. Sol-Gel Sci. Technol. 26 (n.d.) 645.

[62] T.F. Baumann, S.O. Kucheyev, A.E. Gash, J.H. Satcher, Adv. Mater. 17 (2005) 1546.

[63] J. Di, D. Hu, H. Chen, Z. Yong, M. Chen, Z. Feng, Y. Zhu, Q. Li, ACS Nano 6 (2012) 5457.

[64] X. Gui, Z. Zeng, Y. Zhu, H. Li, Z. Lin, Q. Gan, R. Xiang, A. Cao, Z. Tang, Adv. Mater. 26 (2014) 1248.

[65] H. Li, X. Gui, L. Zhang, S. Wang, C. Ji, J. Wei, K. Wang, H. Zhu, D. Wu, A. Cao, Chem. Commun. (Camb). 46 (2010) 7966.

[66] S.M. Jung, H.Y. Jung, M.S. Dresselhaus, Y.J. Jung, J. Kong, Sci. Rep. 2 (2012) 849.

[67] P. Calcagnile, D. Fragouli, I.S. Bayer, G.C. Anyfantis, L. Martiradonna, P.D. Cozzoli, R. Cingolani, A. Athanassiou, ACS Nano 6 (2012) 5413.

[68] J. Yuan, X. Liu, O. Akbulut, J. Hu, S.L. Suib, J. Kong, F. Stellacci, Nat. Nanotechnol. 3 (2008) 332.

[69] P. Thanikaivelan, N.T. Narayanan, B.K. Pradhan, P.M. Ajayan, Sci. Rep. 2 (2012) 230.

[70] Y. Han, X. Quan, S. Chen, H. Zhao, C. Cui, Y. Zhao, Sep. Purif. Technol. 50 (2006) 365.

[71] A. Misra, J.R. Raney, L. De Nardo, A.E. Craig, C. Daraio, ACS Nano 5 (2011) 7713.

[72] M.S. Whittingham, MRS Bull. 33 (2011) 411.

[73] A.F. Burke, Proc. IEEE 95 (2007) 806.

[74] M. Winter, R.J. Brodd, Chem. Rev. 104 (2004) 4245.

[75] J.B. Goodenough, H.D. Abruna, M. V. Buchanan, Basic Research Needs for Electrical Energy Storage. Report of the Basic Energy Sciences Workshop on Electrical Energy Storage, April 2-4, 2007, 2007.

[76] P. Simon, Y. Gogotsi, Nat. Mater. 7 (2008) 845.

[77] R.G. Eggert, Issues Sci. Technol. 26 (2010).

[78] J.A. Fernández, T. Morishita, M. Toyoda, M. Inagaki, F. Stoeckli, T.A. Centeno, J. Power Sources 175 (2008) 675.

[79] C.-C. Hu, K.-H. Chang, M.-C. Lin, Y.-T. Wu, Nano Lett. 6 (2006) 2690.

[80] G.G. Wallace, P.R. Teasdale, G.M. Spinks, L.A.P. Kane-maguire, Conductive Electroactive Polymers: Intelligent Polymer Systems, Third Edit, CRC Press, 2008.

[81] K. Naoi, M. Morita, Interface 17 (2008) 44.

[82] G. Milczarek, O. Inganas, Science (80-.). 335 (2012) 1468.

[83] J.R. Miller, P. Simon, Science 321 (2008) 651.

[84] D. Pech, M. Brunet, H. Durou, P. Huang, V. Mochalin, Y. Gogotsi, P.-L. Taberna, P. Simon, Nat. Nanotechnol. 5 (2010) 651.

[85] P. Simon, Y. Gogotsi, Philos. Trans. A. Math. Phys. Eng. Sci. 368 (2010) 3457.

[86] A. Ghosh, Y.H. Lee, ChemSusChem 5 (2012) 480.

[87] H. Yamada, P.R. Bandaru, Appl. Phys. Lett. 102 (2013) 173113.

[88] L.L. Zhang, X. Zhao, H. Ji, M.D. Stoller, L. Lai, S. Murali, S. Mcdonnell, B. Cleveger, R.M. Wallace, R.S. Ruoff, Energy Environ. Sci. 5 (2012) 9618.

[89] M.R. Arcila-Velez, J. Zhu, A. Childress, M. Karakaya, R. Podila, A.M. Rao, M.E. Roberts, Nano Energy 8 (2014) 9.

[90] M. Endo, T. Hayashi, Y.-A. Kim, Pure Appl. Chem. 78 (2006).

[91] R. Guzmán de Villoria, A.J. Hart, B.L. Wardle, ACS Nano 5 (2011) 4850.

[92] P.G. Whitten, G.M. Spinks, G.G. Wallace, Carbon N. Y. 43 (2005) 1891.

[93] M. Kaempgen, C.K. Chan, J. Ma, Y. Cui, G. Gruner, Nano Lett. 9 (2009) 1872.

[94] K. Jost, C.R. Perez, J.K. McDonough, V. Presser, M. Heon, G. Dion, Y. Gogotsi, Energy Environ. Sci. 4 (2011) 5060.

[95] X. Zhao, B.T.T. Chu, B. Ballesteros, W. Wang, C. Johnston, J.M. Sykes, P.S. Grant, Nanotechnology 20 (2009) 065605.

[96] H. Dura, J. Perry, T. Lecacou, F. Markoulidis, C. Lei, S. Khalil, M. Decker, M. Weil, in:, 2013 Int. Conf. Clean Electr. Power, IEEE, 2013, pp. 516–523.

[97] M.I. Katsnelson, Graphene: Carbon in Two Dimensions, Cambridge University Press, Cambridge, 2012.

[98] F. Banhart, J. Kotakoski, A. V Krasheninnikov, ACS Nano 5 (2011) 26.

[99] M.D. Stoller, S. Park, Y. Zhu, J. An, R.S. Ruoff, Nano Lett. 8 (2008) 3498.

[100] S. Radic, N.K. Geitner, R. Podila, A. Käkinen, P. Chen, P.C. Ke, F. Ding, Sci. Rep. 3 (2013) 2273.

[101] J.A. Nichols, H. Saito, C. Deck, P.R. Bandaru, J. Appl. Phys. 102 (2007) 064306.

[102] U.M. Kelkar, M.H. Gordon, L.A. Roe, Y. Li, J. Vac. Sci. Technol. A Vacuum, Surfaces, Film. 17 (1999) 125.

[103] J.-J. Zeng, Y.-J. Lin, Appl. Phys. Lett. 104 (2014) 233103.

[104] J.W. Lee, J.F. Donohue, K.D. Mackenzie, R. Westerman, D. Johnson, S.J. Pearton, Solid. State. Electron. 43 (1999) 1769.

[105] M. Hoefer, P. Bandaru, J. Electrochem. Soc. 160 (2013) H360.

[106] P. Chen, M.A. Fryling, R.L. McCreery, Anal. Chem. 67 (1995) 3115.

[107] L.M. Malard, M.A. Pimenta, G. Dresselhaus, M.S. Dresselhaus, Phys. Rep. 473 (2009) 51.

[108] A. Felten, D. McManus, C. Rice, L. Nittler, J.-J. Pireaux, C. Casiraghi, Appl. Phys. Lett. 105 (2014) 183104.

[109] D.S. Knight, W.B. White, J. Mater. Res. 4 (1989) 385.

[110] F. Tuinstra, J. Chem. Phys. 53 (1970) 1126.

[111] M.A. Pimenta, G. Dresselhaus, M.S. Dresselhaus, L.G. Cançado, A. Jorio, R. Saito, Phys. Chem. Chem. Phys. 9 (2007) 1276.

[112] R. Rao, R. Podila, R. Tsuchikawa, J. Katoch, D. Tishler, A.M. Rao, M. Ishigami, ACS Nano 5 (2011) 1594.

[113] L.G. Cançado, M.A. Pimenta, B.R.A. Neves, M.S.S. Dantas, A. Jorio, Phys. Rev. Lett. 93 (2004) 247401.

[114] K. Nakada, M. Fujita, G. Dresselhaus, M.S. Dresselhaus, Phys. Rev. B 54 (1996) 17954.

[115] J. Xia, F. Chen, J. Li, N. Tao, Nat. Nanotechnol. 4 (2009) 505.

[116] T. Fang, A. Konar, H. Xing, D. Jena, Appl. Phys. Lett. 91 (2007) 092109.

[117] H. Gerischer, in:, P.J. GEllings, H.J.M. Bouwmeester (Eds.), CRC Handb., CRC Press, Boca Raton, FL, 1997.

[118] N.W. Ashcroft, N.D. Mermin, Solid State Physics, Saunders College, Orlando, FL, 1976.

[119] E. Uesugi, H. Goto, R. Eguchi, A. Fujiwara, Y. Kubozono, Sci. Rep. 3 (2013) 1595.

[120] A.J. Bard, L.R. Faulkner, Electrochemical Methods: Fundamentals and Applications, 2nd ed., John Wiley, New York, 2001.

[121] A. Ashraf, Y. Wu, M.C. Wang, N.R. Aluru, S.A. Dastgheib, S. Nam, Langmuir 30 (2014) 12827.

[122] I.O. Maciel, N. Anderson, M. a Pimenta, A. Hartschuh, H. Qian, M. Terrones, H. Terrones, J. Campos-Delgado, A.M. Rao, L. Novotny, A. Jorio, Nat. Mater. 7 (2008) 878.

[123] A. Jorio, R. Saito, G. Dresselhaus, M. Dresselhaus, Raman Spectroscopy in Graphene Related Systems, Wiley-VCH Verlag GmbH & Co. KGaA, Weinheim, 2011.

[124] a. C. Ferrari, J.C. Meyer, V. Scardaci, C. Casiraghi, M. Lazzeri, F. Mauri, S. Piscanec, D. Jiang, K.S. Novoselov, S. Roth, a. K. Geim, Phys. Rev. Lett. 97 (2006) 187401.

[125] J.T. Spear, T. Pichler, P. Ayala, A.M. Rao, R. Podila, J. Chac, 123108 (2012) 3.

[126] A.C. Ferrari, Solid State Commun. 143 (2007) 47.

[127] S. Nunomura, M. Kondo, J. Appl. Phys. 102 (2007) 093306.

[128] K. Okajima, K. Ohta, M. Sudoh, Electrochim. Acta 50 (2005) 2227.

[129] M.I. Katsnelson, Mater. Today 10 (2007) 20.

[130] K.S. Novoselov, Z. Jiang, Y. Zhang, S. V Morozov, H.L. Stormer, U. Zeitler, J.C. Maan, G.S. Boebinger, P. Kim, A.K. Geim, Science (80-.). 315 (2007) 1379.

[131] R.R. Nair, P. Blake, A.N. Grigorenko, K.S. Novoselov, T.J. Booth, T. Stauber, N.M.R. Peres, A.K. Geim, Science 320 (2008) 1308.

[132] N.M. Gabor, J.C.W. Song, Q. Ma, N.L. Nair, T. Taychatanapat, K. Watanabe, T. Taniguchi, L.S. Levitov, P. Jarillo-Herrero, Science 334 (2011) 648.

[133] M.I. Katsnelson, K.S. Novoselov, A.K. Geim, Nat. Phys. 2 (2006) 620.

[134] D. Wei, Y. Liu, Y. Wang, H. Zhang, L. Huang, G. Yu, Nano Lett. 9 (2009) 1752.

[135] H. Wang, T. Maiyalagan, X. Wang, ACS Catal. 2 (2012) 781.

[136] A. Lherbier, X. Blase, Y.-M. Niquet, F. Triozon, S. Roche, Phys. Rev. Lett. 101 (2008) 036808.

[137] L. Feng, Y. Chen, L. Chen, ACS Nano 5 (2011) 9611.

[138] H.M. Jeong, J.W. Lee, W.H. Shin, Y.J. Choi, H.J. Shin, J.K. Kang, J.W. Choi, Nano Lett. 11 (2011) 2472.

[139] Z. Jin, J. Yao, C. Kittrell, J.M. Tour, ACS Nano 5 (2011) 4112.

[140] B. Guo, Q. Liu, E. Chen, H. Zhu, L. Fang, J.R. Gong, Nano Lett. 10 (2010) 4975.

[141] D. Usachov, O. Vilkov, A. Grüneis, D. Haberer, A. Fedorov, V.K. Adamchuk, A.B. Preobrajenski, P. Dudin, A. Barinov, M. Oehzelt, C. Laubschat, D. V Vyalikh, Nano Lett. 11 (2011) 5401.

[142] X. Wang, X. Li, L. Zhang, Y. Yoon, P.K. Weber, H. Wang, J. Guo, H. Dai, Science 324 (2009) 768.

[143] L. Zhao, R. He, K.T. Rim, T. Schiros, K.S. Kim, H. Zhou, C. Gutiérrez, S.P. Chockalingam, C.J. Arguello, L. Pálová, D. Nordlund, M.S. Hybertsen, D.R. Reichman, T.F. Heinz, P. Kim, A. Pinczuk, G.W. Flynn, A.N. Pasupathy, Science 333 (2011) 999.

[144] M. Brandbyge, J.-L. Mozos, P. Ordejón, J. Taylor, K. Stokbro, Phys. Rev. B 65 (2002) 165401.

[145] P. Puneet, R. Podila, S. Zhu, M.J. Skove, T.M. Tritt, J. He, A.M. Rao, Adv. Mater. 25 (2013) 1033.

[146] Y. Zhang, T.-T. Tang, C. Girit, Z. Hao, M.C. Martin, A. Zettl, M.F. Crommie, Y.R. Shen, F. Wang, Nature 459 (2009) 820.

[147] R. Podila, J. Chacón-Torres, J.T. Spear, T. Pichler, P. Ayala, A.M. Rao, Appl. Phys. Lett. 101 (2012) 123108.

[148] P. Ayala, A. Grüneis, T. Gemming, D. Grimm, C. Kramberger, M.H. Rümmeli, F.L. Freire, H. Kuzmany, R. Pfeiffer, A. Barreiro, B. Büchner, T. Pichler, J. Phys. Chem. C 111 (2007) 2879.

[149] A.L. Elías, P. Ayala, A. Zamudio, M. Grobosch, E. Cruz-Silva, J.M. Romo-Herrera, J. Campos-Delgado, T. Terrones, H.; Pichler, M. Terrones, J. Nanosci. Nanotechnol. 10 (2010) 3959.

[150] L.G. Cançado, M.A. Pimenta, B.R.A. Neves, M.S.S. Dantas, A. Jorio, Phys. Rev. Lett. 93 (2004) 247401.

[151] I.O. Maciel, N. Anderson, M.A. Pimenta, A. Hartschuh, H. Qian, M. Terrones, H. Terrones, J. Campos-Delgado, A.M. Rao, L. Novotny, A. Jorio, Nat. Mater. 7 (2008) 878.

[152] L. Cançado, M. Pimenta, B. Neves, M. Dantas, A. Jorio, Phys. Rev. Lett. 93 (2004) 247401.

[153] P. May, M. Lazzeri, P. Venezuela, F. Herziger, G. Callsen, J.S. Reparaz, A. Hoffmann, F. Mauri, J. Maultzsch, Phys. Rev. B 87 (2013) 075402.

[154] P.T. Araujo, D.L. Mafra, K. Sato, R. Saito, J. Kong, M.S. Dresselhaus, Phys. Rev. Lett. 109 (2012) 046801.

[155] P. May, M. Lazzeri, P. Venezuela, F. Herziger, G. Callsen, J. Reparaz, A. Hoffmann, F. Mauri, J. Maultzsch, Phys. Rev. B 87 (2013) 075402.

[156] Z. Luo, C. Cong, J. Zhang, Q. Xiong, T. Yu, Carbon N. Y. 50 (2012) 4252.

[157] R. Podila, B. Anand, J.T. Spear, P. Puneet, R. Philip, S.S.S. Sai, A.M. Rao, Nanoscale 4 (2012) 1770.

[158] J.M. Dawlaty, S. Shivaraman, M. Chandrashekhar, F. Rana, M.G. Spencer, Appl. Phys. Lett. 92 (2008) 042116.

[159] R.L. Sutherland, Handbook of Nonlinear Optics, Marcel Dekker Inc., New York, 1996.

[160] B. Anand, A. Kaniyoor, S.S.S. Sai, R. Philip, S. Ramaprabhu, J. Mater. Chem. C 1 (2013) 2773.

[161] H. Yang, X. Feng, Q. Wang, H. Huang, W. Chen, A.T.S. Wee, W. Ji, Nano Lett. 11 (2011) 2622.

[162] S. Kumar, M. Anija, N. Kamaraju, K.S. Vasu, K.S. Subrahmanyam, A.K. Sood, C.N.R. Rao, Appl. Phys. Lett. 95 (2009) 191911.

[163] S. Kaniyankandy, S.N. Achary, S. Rawalekar, H.N. Ghosh, J. Phys. Chem. C 115 (2011) 19110.

[164] G.-K. Lim, Z.-L. Chen, J. Clark, R.G.S. Goh, W.-H. Ng, H.-W. Tan, R.H. Friend, P.K.H. Ho, L.-L. Chua, Nat. Photonics 5 (2011) 554.

[165] L.G. Cançado, A. Jorio, E.H.M. Ferreira, F. Stavale, C.A. Achete, R.B. Capaz, M.V.O. Moutinho, A. Lombardo, T.S. Kulmala, A.C. Ferrari, Nano Lett. 11 (2011) 3190.

[166] Q. Bao, H. Zhang, Y. Wang, Z. Ni, Y. Yan, Z.X. Shen, K.P. Loh, D.Y. Tang, Adv.

Funct. Mater. 19 (2009) 3077.

[167] D.S. Chemla, D.A.B. Miller, J. Opt. Soc. Am. B 2 (1985) 1155.

[168] P.H. Tan, W.P. Han, W.J. Zhao, Z.H. Wu, K. Chang, H. Wang, Y.F. Wang, N. Bonini, N. Marzari, N. Pugno, G. Savini, A. Lombardo, A.C. Ferrari, Nat. Mater. 11 (2012) 294.